BAYESIAN ESTIMATION OF GRAIN SCALE ELASTIC-PLASTIC INTRINSIC MATERIAL PROPERTIES VIA SPHERICAL INDENTATION MEASUREMENTS AND THE EXPLORATION OF DESIGN OF EXPERIMENTS STRATEGIES

A Dissertation
Presented to
The Academic Faculty

by

Andrew R. Castillo

In Partial Fulfillment
of the Requirements for the Degree
Doctor of Philosophy in the
Woodruff School of Mechanical Engineering

Georgia Institute of Technology
May 2020

BAYESIAN ESTIMATION OF GRAIN SCALE ELASTIC-PLASTIC INTRINSIC MATERIAL PROPERTIES VIA SPHERICAL INDENTATION MEASUREMENTS AND THE EXPLORATION OF DESIGN OF EXPERIMENTS STRATEGIES

Approved by:

Dr. Surya R. Kalidindi, Advisor
George W. Woodruff School of Mechanical Engineering
Georgia Institute of Technology

Dr. Hamid Garmestani
School of Materials Science and Engineering
Georgia Institute of Technology

Dr. Joseph Roshan
H. Milton Stewart School of Industrial and Systems Engineering
Georgia Institute of Technology

Dr. Shreyes N. Melkote
George W. Woodruff School of Mechanical Engineering
Georgia Institute of Technology

Dr. David L. McDowell
George W. Woodruff School of Mechanical Engineering
Georgia Institute of Technology

Date Approved: April 24, 2020

This work is dedicated to my Grandparents, Andronico and Alicia Castillo. For whom I know are smiling down.

ACKNOWLEDGEMENTS

First, I would like to thank my advisor, Dr. Surya Kalidindi, for his support and guidance throughout my Ph.D. He has continually encouraged me to think independently and pushed me to explore new research topics with a critical mindset. I have been fortunate to have the opportunity to work on a wide variety of research topics while under his supervision. I would also like to thank Dr. Roshan Joseph, for various conversations and advice. His collaboration and technical expertise have been instrumental in making these projects possible.

I am also thankful to the whole MINED research group. In particular, I am grateful to Aditiya Venkatraman for his contribution toward CPFE simulations, as well as Alicia Rossi, Natalia Millan and Soumya Mohan for their contributions in experimental data. I am thankful to Dipen Patel, Apaar Shankaar and Sepideh Hashemi for the endless conversations to help clarify new and old ideas; and Marshall Johnson for his assistance in exploring new research topics.

Additionally, I would like to acknowledge the financial support provided by the National Science Foundation (NSF) Office of Naval Research (ONR), the Airforce Office of Scientific Research (AFOSR) and Air Force Research Laboratory (AFRL) for the work done in this thesis.

I am especially thankful to my parents Valerie and Dony Castillo, my fiancé Sepi, my sisters Abby, Alyssa, Andrea, and my friends who have provided me with endless support throughout this endeavor.

TABLE OF CONTENTS

LIST OF TABLES

LIST OF FIGURES

LIST OF SYMBOLS AND ABBREVIATIONS

BCC	Body Centered Cube
BLR	Bayesian Linear Regression
CPFE	Crystal Plasticity Finite Element
FE	Finite Element
HCP	Hexagonal Close Packed
KL	Kullback-Liebler
MCMC	Markov Chain Monte Carlo
PMC	Polymer Matrix Composite
ROM	Reduced Order Model
SCMH	Single Component Metropolis Hastings
SHH	Surface Spherical Harmonics

SUMMARY

This thesis is focused on establishing and demonstrating a statistical framework for the objective fusion of data acquired from multiscale experiments and multiscale models performed to understand and predict the intrinsic material behavior. What makes this difficult is that the experimental data often provides information only on derived quantities from the material response (only these can be measured at present) and not directly the parameters present in the physics-based multiscale materials constitutive models. Consequently, one has to use sophisticated statistical theories to estimate the values of the critically needed material parameters and quantify rigorously the implicit uncertainty in this quantification. A mathematical framework that addresses this gap and its unique capabilities are demonstrated through the extraction of single crystal elastic-plastic constants for thermodynamic phases present in the microstructure of a metallic alloy and the extraction of laminate level properties for multi-laminate composite system.

CHAPTER 1. INTRODUCTION

Continued development and application of physics-based multiscale materials models is largely hampered by the lack of protocols for reliably estimating the intrinsic material properties at the microscale (e.g., the grain-scale properties in modeling of polycrystalline materials). In recent years, instrumented indentation techniques have been demonstrated to be capable of providing consistent and reliable measurements at the lower length scales (up to submicron length scales) [1-5]. Although small-scale mechanical measurements are now quite reliable, it has not been a straightforward process to extract the intrinsic material properties from such measurements. As specific examples, there is a lack of protocols to estimate the values of the single crystal elastic constants and the critical resolved shear strengths along with their associated uncertainties from the instrumented nanoindentation measurements.

Currently employed strategies for extracting intrinsic material properties from indentation tests have generally involved the calibration of physics-based finite element (FE) models of these tests to the corresponding set of experimental measurements [6-9]. These protocols are much more robust when the calibration is attempted in the form of the normalized indentation stress-strain curves as opposed to directly matching the load-displacement curves [10]. This is mainly because the initial elastic response and the elastic-plastic transition occur over a very short early portion of the load-displacement curve that is not easily identified and isolated, resulting in a very high sensitivity of the extracted values of the intrinsic material properties to small changes in the calibration procedures.

One of the central bottlenecks in addressing the critical gap identified above comes from the fact that the forward model connecting the intrinsic material properties of the material to their corresponding indentation stress-strain responses requires the execution of a computationally expensive finite element (FE) model of the indentation test [8-11]. Since the solution of the inverse problem formulated above requires many forward solutions, there is a critical need for a clever strategy. One such strategy involving a two-step protocol has been formalized: (1) Establish a surrogate model for the computationally intensive FE simulations; (2) Use inverse methodologies to calibrate intrinsic material parameters given available experimental data.

The main difficulty with the two-step protocol described above lies in building the reduced-order model (i.e., step (1)). Because of the need to cover a large space (for example for extracting single crystal elastic constants, the input space of interest is the product space spanning all combinations of the single crystal elastic constants, C_{11}, C_{12}, C_{44}, and all possible grain orientations), one needs to generate a large amount of the FE simulation data in order to establish a high-fidelity reduced-order model. The difficulty of this task is amplified significantly in dealing with hcp crystals, where the numbers of the intrinsic properties is significantly larger (for example, modeling the elastic deformation in hcp crystals requires specification of five independent single crystal elastic constants). Obviously, the uncertainty associated with predictions from the reduced order model is variable with respect to the coverage of the large space of input parameters. In such cases, one needs to examine carefully where one should produce additional simulations in order to best improve the reduced order model. This kind of a rational approach for deciding where to generate new data points is critical for situations where data generation is

expensive (as is the case with the FE simulations of the spherical indentation for the present case study). Once the strategy for establishing a reduced-order model is developed and validated, the main remaining challenge come from the efficient execution of the experiments (i.e., step (2)).

The experimental component of step (2) of the protocol involves conducting indentation measurements in grains of different orientations. A typical strategy for this task has been to perform as many indentation experiments in as many grains as possible [8,12]. The only guidance one typically gets is to select grains orientations that ensure a roughly uniform coverage of the fundamental zone of the relevant orientation space (defined based on the crystal symmetry) [1,13]. Here is where an optimal design of experiments strategy might prove to be very beneficial. As a specific example, a properly designed strategy can inform the experimentalist on the following questions: (i) Amongst the available grain orientations on the sample, which orientation is likely to offer the most valuable information in improving the estimates of the intrinsic material properties of interest? (ii) When should one stop doing more tests? The answers to these questions have the potential to improve the reliability of the extracted values of the intrinsic material parameters of interest, while minimizing the number of experiments conducted.

CHAPTER 2. EXECUTIVE SUMMARY

This chapter provides an executive summary which serves as an overview of the remaining chapters of this thesis. The aforementioned chapters include publication quality material from the candidate's cohesive body of work. The executive summary summarizes the general methodologies consistently applied throughout the chapters and selected findings from the candidate's research.

2.1 Importance

The lack of robust strategies for extracting reliable values of the intrinsic material parameters from related experimental measurements is currently one of the central bottlenecks in the advancement of multiscale materials modeling capabilities (e.g., the grain-scale properties in modeling of polycrystalline materials). In recent years, instrumented indentation techniques have been demonstrated to be capable of providing consistent and reliable measurements at the lower length scales (up to submicron length scales) [2,4,5,14,15]. Although small-scale mechanical measurements are now quite reliable, it has not been a straightforward process to extract the intrinsic material properties from such measurements. As specific examples, there is a lack of protocols to estimate the values of the single crystal elastic constants and the critical resolved shear strengths along with their associated uncertainties from the instrumented nanoindentation measurements.

2.2 Background

2.2.1 Simulated Spherical Indentation Stress-Strain Curves

Currently employed strategies for extracting intrinsic material properties from indentation tests have generally involved the calibration of physics-based models (e.g. finite element (FE) models) of these tests to the corresponding set of experimental measurements [6-9]. In this regard, it has been pointed out in recent work [10], that these protocols are much more robust when the calibration is attempted in the form of the normalized indentation stress-strain curves as opposed to directly matching the load-displacement curves. The spherical indentation stress-strain analyses protocols developed previously will be briefly summarized here.

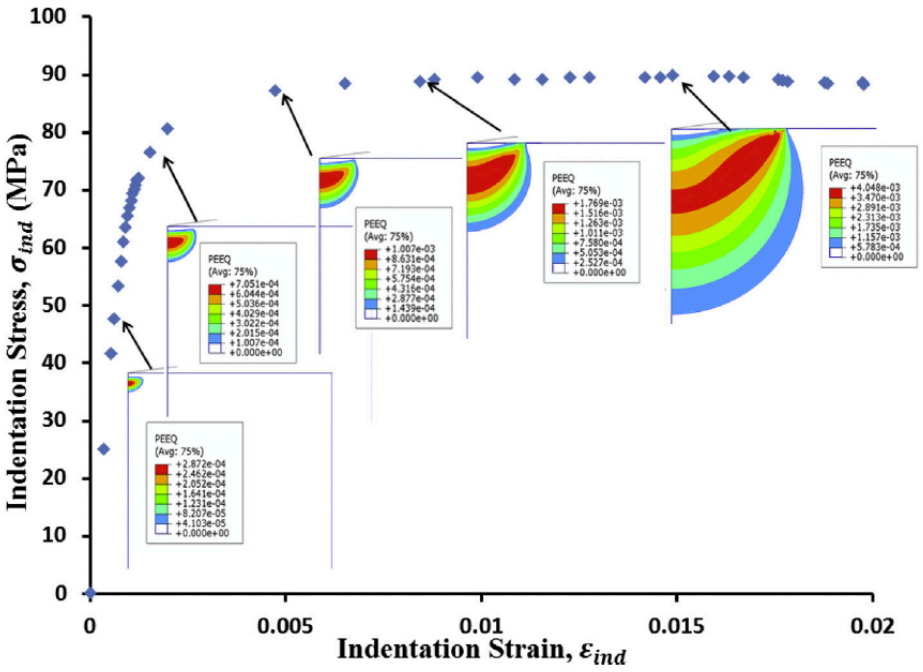

Figure 2.1 Simulated Indentation Stress Strain Curve using Finite Element Simulations from Prior Work [16].

These protocols are based on the relationships initially established by the elastic, frictionless, contact between two isotropic, homogenous bodies with quadratic surfaces by Hertz Theory [17].

$$\mathcal{P} = \frac{4}{3} E^* R_{eff}^{\frac{1}{2}} h_e^{\frac{3}{2}} \tag{2.1}$$

$$a = \sqrt{R_{eff} h_e} \tag{2.2}$$

where $\mathcal{P}$ is the indentation load due to the elastic indentation displacement, h_e. In Equation (2.1) R_{eff} denotes the effective radius of the indenter-sample system, and E^* is the effective indentation modulus. Although the measured E^* generally reflects the effective indentation modulus of the indenter-sample system, one can account for the elastic deformation in the indenter itself and recover the indentation modulus of the sample alone [17]. The corresponding distance to the edge of contact between the indenter and the sample surfaces is given by contact radius, a, shown in Equation (6.2). In order to transform indentation load-displacement data into meaningful indentation stress-strain curves, suitable measures of indentation stress, σ_{ind}, and indentation strain, ε_{ind}, have previously been developed [18].

$$\sigma_{ind} = \frac{\mathcal{P}}{\pi a^2} \tag{2.3}$$

$$\varepsilon_{ind} = \frac{4}{3\pi} \frac{h^*}{a} \tag{2.4}$$

These measures are meant to represent effective volume-averaged quantities in the primary deformation zones underneath the indenter. We note h^* generally reflects the total indentation depth of the entire indenter-sample system and, similar to E^*, one can account for the effect due to the indenter in order to recover the indentation depth due solely into the sample. In the treatment presented here, it will be assumed that such corrections have been made, i.e., E^* and h^* denotes the indentation modulus and depth of the sample respectively. The main impediment in the determination of indentation stress and strain measures is that direct measurement of the contact radius, a, is often difficult. We note, when simulating the indentation experiment the computation of a is best accomplished via elastic unloading segments [16]. Each unloading segment corresponds to a single data point for indentation stress-strain measurements. Therefore, the establishment of an indentation stress-strain curve corresponds to the simulation of a loading segment followed by multiple unloading segments. This process leads to a significant computational expense when simulating a full indentation stress-strain curve.

Although the above protocols were initially developed considering the contact between an indenter and isotropic material system, subsequent work has extended such protocols to the extraction of meaningful indentation stress strain curves for anisotropic material systems [1,4,13,15]. In polycrystalline materials, the indentation stress strain curves measured within single grains of a particular thermodynamic phase of a given polycrystalline sample have been found to be a function of the direction of indentation relative to the local crystallographic grain orientation. In the aforementioned studies typically the indentation modulus, E^*, and indentation yield, Y^* (defined by a 0.2% indentation strain offset) are reported from experiment indents within multiple grains of a given polycrystalline sample.

2.2.2 Crystal Plasticity Material Model

In order to extract intrinsic material parameters a suitable physics-based models which takes into relevant constitutive relations must be adopted. In order to simulate the single crystal deformation behavior under the indenter in an experiment, the CPFEM scheme developed by Kalidindi et al. [19,20] is adopted. In order to implement these schemes, a suitable description of the local deformation at the crystal level is adopted from previous works [19,20]. The local deformation at the crystal level is considered through the determination of the local plastic velocity gradient, $\boldsymbol{L}^P$, which is computed from the rates of shear deformation across multiple crystallographic slip systems [21]. $\boldsymbol{L}^P$ is related to the shearing rate across all α slip systems as

$$\boldsymbol{L}^P = \sum_\alpha \dot{\gamma}^\alpha \boldsymbol{S}_0^\alpha, \qquad \boldsymbol{S}_0^\alpha = \boldsymbol{m}^\alpha \otimes \boldsymbol{n}^\alpha \tag{2.5}$$

where $\boldsymbol{S}_0^\alpha$ is the Schmid tensor computed using the slip plane normal, $\boldsymbol{n}^\alpha$, and slip direction $\boldsymbol{m}^\alpha$. The visco-plastic power law commonly used to model the slip activity on slip system α due to an imposed resolved shear stress τ^α is given by

$$\dot{\gamma}^\alpha = \dot{\gamma}_0 \left| \frac{\tau^\alpha}{s^\alpha} \right|^{\frac{1}{m}} sign(\tau^\alpha) \tag{2.6}$$

Where $\dot{\gamma}_0$ is a reference shear rate, m is the rate sensitivity parameter and s^α is the resistance to slip of the α system. We note the slip resistances, s^α, are usually taken to evolve through time in accordance with a hardening law which takes into account the shear rates across all slip systems. In this work, only initial values of slip resistance are of interest.

2.2.3 Reduced order model of Indentation Finite Element Simulations

The general mathematical form of the reduced-order model used to capture the dependence of an indentation property, P^* on the local orientation $\boldsymbol{g}$, and set of intrinsic material parameters, $\boldsymbol{\psi}$ is adopted from prior work [7] as

$$P^* = \hat{P}^*(\boldsymbol{\psi}, \boldsymbol{g}) \approx \sum_{l=0}^{L} \sum_{m=1}^{M(l)} \sum_{\boldsymbol{q}}^{\boldsymbol{Q}} A_l^{mq} \mathrm{K}_l^m(\boldsymbol{g}) \widetilde{\mathrm{P}}^{\boldsymbol{q}}(\bar{\boldsymbol{\psi}}) \tag{2.7}$$

$$\bar{\psi}_j = \frac{2\psi_j - \psi_j^{min} - \psi_j^{max}}{\psi_j^{max} - \psi_j^{min}} \tag{2.8}$$

where $\mathrm{K}_l^m(\boldsymbol{g})$ denote the symmetrized Surface Spherical Harmonics basis over the relevant orientation space of interest, and $\widetilde{\mathrm{P}}^q(\,)$ denote a multivariate Legendre polynomial product basis. In other words, one can express $\widetilde{\mathrm{P}}^{\boldsymbol{q}}(\bar{\boldsymbol{\psi}}) = \mathrm{P}^{q_1}(\bar{\psi}_1)\mathrm{P}^{q_2}(\bar{\psi}_2) \ldots \mathrm{P}^{q_R}(\bar{\psi}_R)$, where $\boldsymbol{q} = (q_1, q_2 \ldots q_R)$ forms a multi-index array, each element of which is a nonnegative integer allowed to vary from 0 to the selected maximum degree, Q, i.e., $q_j \in [0, Q]$. The use of Legendre polynomials provides an orthonormal basis over the range [-1,1], for which each of the elastic constants are rescaled in accordance to Eqn. (2.8), where ψ_j^{max} and ψ_j^{min} are the maximum and minimum values of the j-th elastic constant under consideration. $M(l)$ enumerates the spherical harmonics that implicitly reflect the inherent symmetries of the material system of interest [22,23]. The integers Q and L denote the truncation levels. It is emphasized here that the model form used denotes a Fourier representation using an orthonormal basis that has been previously shown to produce compact representations for mechanical responses of crystalline solids [7,10,24-27]. One of the central features of a

Fourier representation is that the Fourier coefficients A_l^{mq} are completely independent of each other. The goal of the reduced-order modeling tasks here is to estimate the values of A_l^{mq}, expressed in a vector notation as $\boldsymbol{A}$, from the sparse amount of available data generated from the expensive FE simulations.

2.2.4 Bayesian Inference

Bayesian approaches treat model parameters as stochastic variables exhibiting a distribution of values. Most importantly, Bayes' theorem allows one to update the distributions for the model parameters given new data (i.e., observations) and is commonly expressed as

$$P(A|D) = \frac{P(D|A)P(A)}{P(D)} \tag{2.9}$$

where $P(A)$ denotes the prior belief (expressed as a distribution) on the values of the unknown model parameters, $P(D|A)$ denotes the likelihood of sampling the observations D for specified values of the model parameters, and $P(A|D)$ denotes the posterior (updated) belief on the values of the unknown model parameters given the observations D. The denominator $P(D)$ is generally referred as the probability of the evidence, and is often difficult to establish. However, it mainly serves as a normalization factor for the posterior distribution. Since the distributions are often defined with known normalization factors, it is often possible to skip the evaluation of $P(D)$ in practical implementations of the Bayes' rule [28].

2.2.5 Bayesian Linear Regression

The following protocol is used in the establishment of the reduced order models outlined in Section 2.2.3 of the indentation finite element simulation. Let the indentation properties generated from FE simulated database be denoted $\{\boldsymbol{P}^*_{sim}, \boldsymbol{\Psi}_{sim}, \boldsymbol{G}_{sim}\}$ where $P^* \in \boldsymbol{P}^*$ denotes the set of indentation properties corresponding to the $\boldsymbol{\psi} \in \boldsymbol{\Psi}$ set of intrinsic material properties, and $\boldsymbol{g} \in \boldsymbol{G}$ set of orientations. The i[th] observed value of the indentation property is modeled as being generated from a deterministic model, with added stochastic noise, as

$$P^*_i = \hat{P}^*_i(\boldsymbol{A}, \boldsymbol{\psi}_i, \boldsymbol{g}_i) + \varepsilon_i, \qquad \varepsilon_i \sim \mathcal{N}(0, \beta^{-1}) \tag{2.10}$$

where $\mathcal{N}(0, \beta^{-1})$ denotes a normal distribution with a zero mean and a variance of β^{-1}. Note that the stochastic noise is assumed to be independent of location in the parameter space, i.e., homoscedastic. The likelihood for a set of N independently observed indentation moduli can be established using the product rule as

$$p(\boldsymbol{P}^*_{sim} | \boldsymbol{A}, \boldsymbol{\Psi}_{sim}, \boldsymbol{G}_{sim}, \beta) = \prod_i^N p(P_i | \boldsymbol{A}, \boldsymbol{\psi}_i, \boldsymbol{g}_i, \beta) \tag{2.11}$$

the model parameters $\boldsymbol{A}$ are also treated as stochastic variables. The prior belief on these variables is assumed to be specified by a normal distribution with a zero mean and a large variance of α^{-1} as

$$p(\boldsymbol{A}|\alpha) \sim \mathcal{N}(0, \alpha^{-1}\boldsymbol{I}) \tag{2.12}$$

The application of Bayes' rule to the problem at hand results in

$$p(\boldsymbol{A}|\boldsymbol{P}^*_{sim}, \boldsymbol{\Psi}_{sim}, \boldsymbol{G}_{sim}, \alpha, \beta) = \frac{p(\boldsymbol{P}^*_{sim}|\boldsymbol{A}, \boldsymbol{\Psi}_{sim}, \boldsymbol{G}_{sim}, \beta)\, p(\boldsymbol{A}|\alpha)}{p(\boldsymbol{P}^*_{sim}|\boldsymbol{\Psi}_{sim}, \boldsymbol{G}_{sim}, \alpha, \beta)} \tag{2.13}$$

where $p(\boldsymbol{A}|\boldsymbol{P}^*_{sim}, \boldsymbol{\Psi}_{sim}, \boldsymbol{G}_{sim}, \alpha, \beta)$ denotes the posterior (updated) distribution on the model parameters. The denominator reflects the probability of the observed outcomes irrespective of the model parameters $\boldsymbol{A}$ chosen, and can be described by the marginalization of the likelihood with respect to the model parameters as

$$p(\boldsymbol{P}^*_{sim}|\boldsymbol{\Psi}_{sim}, \boldsymbol{G}_{sim}, \alpha, \beta) = \int_{\boldsymbol{A}} p(\boldsymbol{P}^*_{sim}|\boldsymbol{A}, \boldsymbol{\Psi}_{sim}, \boldsymbol{G}_{sim}, \beta)\, p(\boldsymbol{A}|\alpha) d\boldsymbol{A} \tag{2.14}$$

In a fully Bayesian approach, the precision parameters, α, β, may also be treated as stochastic variables [29]. This allows for a separate application of Bayes' theorem expressed as

$$p(\alpha, \beta|\boldsymbol{P}^*_{sim}, \boldsymbol{\Psi}_{sim}, \boldsymbol{G}_{sim}) \propto p(\boldsymbol{P}^*_{sim}|\boldsymbol{\Psi}_{sim}, \boldsymbol{G}_{\boldsymbol{sim}}, \alpha, \beta) p(\alpha, \beta) \tag{2.15}$$

Alternately, one can use point estimates from the maximization of the likelihood, denoted as $\hat{\alpha}, \hat{\beta}$. This is equivalently interpreted as the maximization of the evidence of the observed data in Eqn. (2.14) [30]. With this approach, the posterior distributions of model coefficients in Eqn. (2.13) can be solved analytically (while assuming normal distributions for the various variables involved) [31-33]. The updated posterior distribution computed using the approach described above is generally expected to be sharper (i.e., lower variance) compared to the prior belief.

2.2.6 Markov Chain Monte Carlo

The sampling from a posterior distribution of intrinsic material parameters, $\boldsymbol{\psi}$, for given experimental data, $\{\boldsymbol{P}^*_{exp}, \boldsymbol{G}_{exp}\}$, is accomplished using Markov Chain Monte Carlo (MCMC).

$$p(\boldsymbol{\psi}|\boldsymbol{P}^*_{exp}, \boldsymbol{G}_{exp}) \propto p\left(\boldsymbol{P}^*_{exp}\middle|\boldsymbol{\psi}, \boldsymbol{G}_{exp}\right)p(\boldsymbol{\psi}) \tag{2.16}$$

The goal of MCMC is to generate a Markov Chain which indirectly samples from the posterior distribution of interest as long as the number of samples drawn is very large. The Markov Chain is generated by the acceptance and rejection of a large number of transitions through the space of intrinsic material parameters based on an acceptance probability. In practice, a class of algorithms have been developed in order to define these transitions and are referred as Metropolis-Hastings algorithms [34]. For the proposed protocol, Single Component Metropolis Hastings (SCMH) is suggested, which considers component wise transitions [35]. In the algorithm below for a given step t, partial updates are performed for the sample $\boldsymbol{\psi}_t$ for each component j until all components are updated.

The basic steps for the implementation of the SCMH algorithm are as follows:

1. Initialize a starting point, $\boldsymbol{\psi}_0$, using the best available information
2. Sample transition, $\boldsymbol{\psi}^*$, from a proposal distribution $q_j(*)$ for an update of component j. If t is a new step, initialize $\boldsymbol{\psi}_t = \boldsymbol{\psi}_{t-1}$ where $\boldsymbol{\psi}_t$ will be subjected to partial updates (one component at a time). Mathematically, one can express this as

$$\boldsymbol{\psi}^* \sim q_j(\boldsymbol{\psi}|\boldsymbol{\psi}_t)$$

where $q_j(*)$ proposes $\boldsymbol{\psi}^*$ differing from $\boldsymbol{\psi}_t$ in component j, sampled from a normal distribution with mean ϕ_t^j and variance v_j^2

$$\boldsymbol{\psi}^{j^*} \sim \mathcal{N}\left(\boldsymbol{\psi}^j | \boldsymbol{\psi}_t^j, v_j^2\right)$$

3. Calculate the acceptance probability of transition, $\alpha(*)$

$$\alpha(\boldsymbol{\psi}^* | \boldsymbol{\psi}_t) = \min\left(1, \frac{p\left(\boldsymbol{\psi}^* \middle| \boldsymbol{P}_{exp}^*, \boldsymbol{G}_{exp}\right) q_j(\boldsymbol{\psi}_t | \boldsymbol{\psi}^*)}{p\left(\boldsymbol{\psi}_t \middle| \boldsymbol{P}_{exp}^*, \boldsymbol{G}_{exp}\right) q_j(\boldsymbol{\psi}^* | \boldsymbol{\psi}_t)}\right)$$

$$= \min\left(1, \frac{p\left(\boldsymbol{P}_{exp}^* \middle| \boldsymbol{\psi}^*, \boldsymbol{G}_{exp}\right) p(\boldsymbol{\psi}^*)}{p\left(\boldsymbol{P}_{exp}^* \middle| \boldsymbol{\psi}_t, \boldsymbol{G}_{exp}\right) p(\boldsymbol{\psi}_t)}\right)$$

4. Update Chain (accept/reject proposed transition)
    a. Draw a sample, r, from a standard uniform distribution
    b. If $\alpha > r$

$$\boldsymbol{\psi}_t = \boldsymbol{\psi}^*$$

5. Repeat steps (2-4) until all components of $\boldsymbol{\psi}_t$ are updated, then proceed to a new step.

While the probability of a proposed transition is described by the proposal distribution $q_j(*)$, the probability of accepting the transition is given by $\alpha(*)$. By assuming a flat prior for $p(\boldsymbol{\psi})$, the acceptance probability of a proposed transition is completely specified by the posterior probability of the states evaluated within a normalizing constant using Eqn.(2.16) [34,36]. The variances of the proposal distributions v_j^2 are tuned during the "burn-in" period in order to meet an acceptance rate around ~0.23. Ensuring the acceptance rate lies around 0.23 has been shown to provide efficient convergence of the Markov chain for gaussian posteriors [37].

2.2.7 Information Based Bayesian Sequential Experimental Design

Before the start of the experiments, the pre-existing knowledge about the intrinsic material parameters $\boldsymbol{\psi}$ is encapsulated in the prior distribution, $p(\boldsymbol{\psi})$. Given any available experimental data $\{\boldsymbol{P}^*_{exp}, \boldsymbol{G}_{exp}\}$, the prior knowledge can be updated to obtain the posterior distribution $p\left(\boldsymbol{\psi}\middle|\boldsymbol{P}^*_{exp}, \boldsymbol{G}_{exp}\right)$ using Eqn. (2.16). Therefore, the value (i.e. amount of new information) of the experimental data can be related to the difference between $p\left(\boldsymbol{\psi}\middle|\boldsymbol{P}^*_{exp}, \boldsymbol{G}_{exp}\right)$ and $p(\boldsymbol{\psi})$. One approach to measuring the difference between these two distributions is to use the Kullback-Liebler (KL) divergence expressed as [38]

$$KL\left(p\left(\boldsymbol{\psi}\middle|\boldsymbol{P}^*_{exp}, \boldsymbol{G}_{exp}\right)\middle|\middle|p(\boldsymbol{\psi})\right) = \int \log\frac{p\left(\boldsymbol{\psi}\middle|\boldsymbol{P}^*_{exp}, \boldsymbol{G}_{exp}\right)}{p(\boldsymbol{\psi})} p\left(\boldsymbol{\psi}\middle|\boldsymbol{P}^*_{exp}, \boldsymbol{G}_{exp}\right) d\boldsymbol{\psi} \tag{2.17}$$

However, since $\boldsymbol{P}^*_{exp}$ is unknown before the experiment, the KL distance needs to be averaged over the distribution of the possible values of $\boldsymbol{P}^*_{exp}$ in order to obtain a computable measure. Thus, the objective is to find $\boldsymbol{G}_{exp}$ to maximize the expected KL divergence expressed as

$$I\left(\boldsymbol{G}_{exp}\right) = \int KL\left(p\left(\boldsymbol{\psi}\middle|\boldsymbol{P}^*_{exp}, \boldsymbol{G}_{exp}\right)\middle|\middle|p(\boldsymbol{\psi})\right) p(\boldsymbol{P}^*_{exp}|\, \boldsymbol{G}_{exp}) d\boldsymbol{P}^*_{exp}$$

$$= \iint \log\frac{p\left(\boldsymbol{\psi}\middle|\boldsymbol{P}^*_{exp}, \boldsymbol{G}_{exp}\right)}{p(\boldsymbol{c})} p\left(\boldsymbol{\psi}, \boldsymbol{P}^*_{exp}\middle|\boldsymbol{G}_{exp}\right) d\boldsymbol{\psi} d\boldsymbol{P}^*_{exp} \tag{2.18}$$

where $I(\boldsymbol{G}_{exp})$ can be viewed as the expected Shannon information gain [38,39] (or simply referred as information gain) due to the experiments. This criterion can be used for finding the Bayesian optimal design of experiment [40,41].

2.3 Bayesian Framework for the Extraction of Intrinsic Material Properties via Spherical Indentation Stress Strain Curves

The extraction of grain scale properties from spherical indentation measurements has been formalized in previous works as a two-step process: (1) establishing a reduced-order model calibrated to FE simulations of indentations that takes the relevant intrinsic material properties as inputs and predicts indentation properties (defined suitably on an indentation stress-strain curve), and (2) the extraction of the intrinsic material properties from the available measurements (typically performed on grains of different orientations in a polycrystalline sample) through calibration with the reduced-order model established in step (1). The second step described above typically involves the solution to an optimization problem (i.e., minimizing the difference between the measurements and the predictions from the reduced-order model).

Bayesian inference has been instrumental in model-building tasks with limited amount of data [33,34,42,43]. The adoption of a Bayesian inference framework for the extraction of the intrinsic material properties from indentation measurements offers the following main advantages: (i) it is expected to dramatically reduce the number of FE simulations needed to produce the reduced-order model generated in step (1) as compared to traditional regression approaches, and (ii) it provides a much more rigorous quantification of the uncertainty in the estimates of the intrinsic material properties obtained in step (2), while

providing a platform for accounting for uncertainty in the experimental measurements. Throughout this thesis, a Bayesian inference framework is developed and its advantages demonstrated for both steps of the two-step protocol for the extraction of grain scale intrinsic material properties across a variety of material systems. We note that Bayesian frameworks enable the implementation of information based workflows (See section 2.2.7) which provides guidance in the selection of the grain orientations for indentation measurements by leveraging sequential design strategies. We note these same strategies can be implemented in providing guidance for the selection of inputs to FE simulations in order to expedite the process of establishing a reduced order model. The overall Bayesian framework is presented in Figure 2.2.

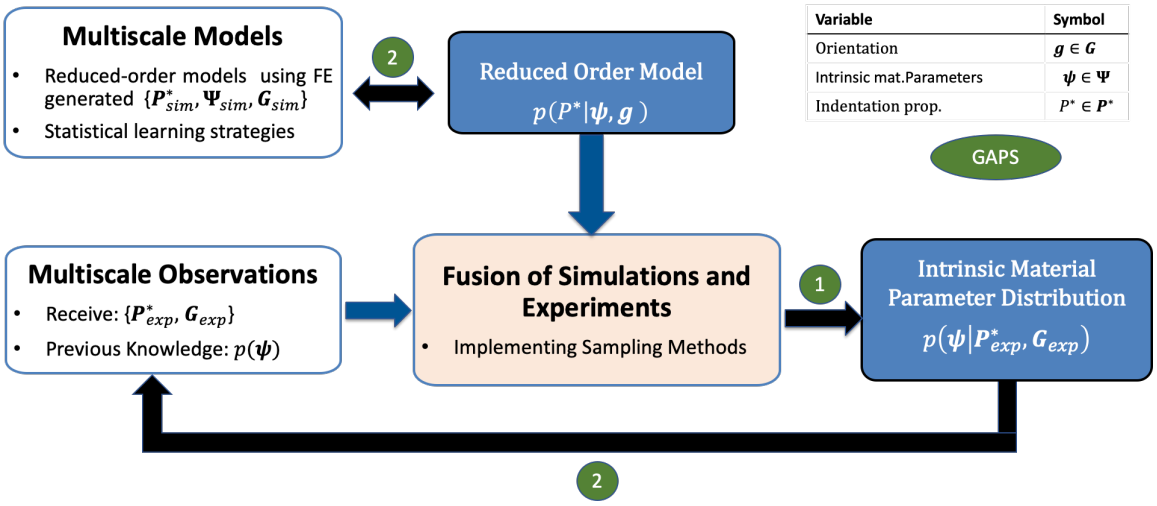

Figure 2.2 Overview of Bayesian Framework and Major Gaps addressed in this thesis. Gap 1: The adoption of a Bayesian framework enables the quantification and propagation of uncertainty from experimental measurements to the extracted intrinsic parameters. Gap 2: Bayesian frameworks enable the dynamic selection of experiments and simulations to best improve the posterior distributions of parameters of interest.

The Bayesian framework is covered extensively in CHAPTER 3 [44]. A brief overview of the methodology in extracting grain scale properties via spherical indentation measurements is given next. In the following let $\boldsymbol{\psi}$ be a set of crystal level intrinsic material

properties, P^* be an experimentally measured indentation property (e.g. indentation modulus *or* indentation yield, (See Section (2.2.1)) which are highly correlated to the underlying intrinsic properties (e.g. single crystal elastic constants *or* initial slip resistances). In this approach, the measured indentation property is modeled as

$$P^* = P^*_{sim}(\boldsymbol{\psi}, \boldsymbol{g}) + \epsilon \tag{2.19}$$

where $P^*_{sim}(\boldsymbol{\psi}, \boldsymbol{g})$ denotes the FE-simulated indentation property at the crystallographic orientation $\boldsymbol{g}$, corresponding to a set of intrinsic material properties, $\boldsymbol{\psi}$, and $\epsilon \sim \mathcal{N}(0, \lambda)$ denotes a stochastic noise term. It is implicitly assumed here that the FE simulated $P^*_{sim}(\boldsymbol{\psi}, \boldsymbol{g})$ exhibits negligible variance. Let $\{\boldsymbol{P}^*_{exp}, \boldsymbol{G}_{exp}\}$ denote the set of experimental indentation properties, $\boldsymbol{P}^*_{exp}$, measured at the corresponding crystallographic orientations, $\boldsymbol{G}_{exp}$. The likelihood for n experimental measurements (denoted $\{\boldsymbol{P}^*_{exp}, \boldsymbol{G}_{exp}\}$) is expressed as

$$p\left(\boldsymbol{P}^*_{exp} \middle| \boldsymbol{\psi}, \boldsymbol{G}_{exp}\right) = \prod_{i}^{n} \frac{1}{\sqrt{2\pi}\sigma_i} exp\left\{\frac{-(P^*_i - P^*_{sim}(\boldsymbol{\psi}, \boldsymbol{g}_i))^2}{2\sigma_i^2}\right\} \tag{2.20}$$

Where P^*_i denotes the experimental indentation property measured at the i-th orientation and σ_i^2 is the variance exhibited by the indentation modulus at the i-th orientation. We note the formulation of the likelihood and its associated parameters (in particular variance) are modified on a case by case basis dependent upon the available experimental data. Inference of the intrinsic material properties, $\boldsymbol{\psi}$, for the observed experimental data can be expressed by Bayes rule:

$$p\left(\boldsymbol{\psi}\middle|\boldsymbol{P}_{exp}^{*},\boldsymbol{G}_{exp}\right)\propto p\left(\boldsymbol{P}_{exp}^{*}\middle|\boldsymbol{\psi},\boldsymbol{G}_{exp}\right)p(\boldsymbol{\psi}) \tag{2.21}$$

Considering a uniform prior for $p(\boldsymbol{\psi})$ along with the likelihood function shown in Eqn. (2.20) allows for the application of MCMC methods for sampling the posterior distribution on single crystal properties [45]. MCMC algorithms seek to generate a sequence, known as a Markov Chain, which converges to a target posterior distribution by accepting/rejecting a large number of proposed transitions across a finite parameter space based on an acceptance probability. Specifically, the Single Component Metropolis Hastings (SCMH) algorithm (See section 2.2.6) is adopted in this work to generate transitions across the multivariate parameter space of intrinsic material parameters [35].

The high computational costs associated with the execution of the FE models of indentation make it impractical to use the FE indentation models directly in the computations described above. The only practical approach for addressing this challenge is to first establish a reduced-order model. The development of this reduced-order model involves the use of an expanded Fourier basis (See Section 2.2.3) and the calibration of the Fourier coefficients via Bayesian Linear Regression (BLR) (See Section 2.2.5). The usage of BLR provides a valuable quantification of uncertainty associated with the predictions from the reduced-order model [30]. In order to establish the reduced-order model, a database of finite element simulations covering the relevant input parameter space is necessary. The quantification of uncertainty provided by BLR enables the deployment of sequential strategies to build a simulated database by focusing on areas of high predictive uncertainty. Such an approach is rooted in the maximization of expected information gain (See section 2.2.7) [46]. Simulations can be continually performed until sufficient performance of the reduced-order

model is achieved, as determined by various error metrics. Such strategies are explored and evaluated extensively in CHAPTER 3 for the establishment of a reduced order model to capture the dependence of indentation modulus on single crystal elastic constants of an hcp material and crystallographic orientation and demonstrated again clearly in CHAPTER 5 for the establishment of a reduced order model to capture the dependence of indentation modulus on effective single ply elastic constants of PMC and ply orientation. One of the greatest advantages of establishing a reduced order model comes when the goal is to extract intrinsic crystal level elastic-plastic properties of multiple alloys. In such situations a carefully established reduced order model can be reapplied to multiple alloys. This is best demonstrated in the estimation of slip resistances and single crystal elastic constants for the alpha phase of differing compositions from spherical indentation measurements in a collection of Ti alloys in CHAPTER 6.

The estimation of the intrinsic material parameters (e.g. single crystal elastic constants *or* slip resistances) involves the matching of the simulated and the measured indentation property (e.g. indentation moduli *or* indentation yield) in grains of different orientations selected in a polycrystalline/ordered sample. The Bayesian framework enables the computation of information gain relevant to a potential new experiment (See section 2.2.7) using the current distribution of intrinsic material properties. This information provides guidance in the selection of the grain orientations for additional indentation measurements. This sequential workflow tracks rigorously the improvements made to the distributions on the intrinsic material parameters of interest, as new indentation measurements are added. In this strategy, one can objectively decide when to stop making further measurements because the protocols will naturally reveal when there are no further improvements to the

distributions with the addition of new measurements. In summary the Bayesian framework enables the optimal selection of the next orientation, $\boldsymbol{g} \in \boldsymbol{G}_{map}$, for the indentation measurement such that we can obtain the largest reduction in the variance for the distributions on the intrinsic material properties of interest. Such strategies are explored in CHAPTER 4.

2.4 Selected Findings

2.4.1 Summary of Case Studies Considered

As previously mentioned, the Bayesian Framework and its capabilities are demonstrated through the extraction of single crystal elastic-plastic constants for thermodynamic phases present in the microstructure of various metallic alloys and the extraction of effective single ply properties for multi-laminate composite system. the case studies and their relevant section in this Chapter are summarized in Table 2.1. We note, each section provides a brief introduction to the work associated with the extracted parameters, and further directs the reader to the relevant chapters of this thesis for a more thorough review if necessary.

Table 2.1 Summary of Case studies considered throughout this thesis. The extraction of intrinsic material parameters is demonstrated across a variety of material systems using the 2-step Bayesian Framework presented in this thesis.

Section Number	Material	Structure	Intrinsic Material Parameters, $\boldsymbol{\psi}$	Structure Descriptor	Indentation Property, P^*	Example Microstructure
2.4.2	Fe-3%-Si	Cubic Single Crystal	$\boldsymbol{c} = \{C_{11}, C_{12}, C_{44}\}$	$\boldsymbol{g} = \{\varphi_1, \phi, \varphi_2\}$	$E^*(\mathbf{c}, \phi, \varphi_2)$	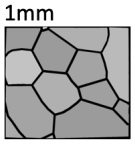
2.4.3	PMC	Homogenized Single Plies	$\boldsymbol{c} = \{C_{11}, C_{12}, C_{44}, C_{33}, C_{13}\}$	$\boldsymbol{g} = \{\phi\}$, homogenized	$E^*(\mathbf{c}, \phi)$	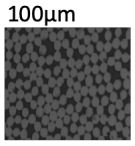
2.4.4	Ti-Alloys (α)	HCP Single Crystal	$\boldsymbol{c} = \{C_{11}, C_{12}, C_{44}, C_{33}, C_{13}\}$ $\boldsymbol{s} = \{s_{pr}, s_{ba}, s_{pyr-a}, s_{py-c+a}\}$	$\boldsymbol{g} = \{\varphi_1, \phi, \varphi_2\}$	$E^*(\mathbf{c}, \phi)$ $Y^*(\mathbf{s}, \phi, \varphi_2)$	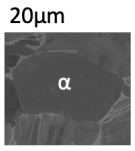

2.4.2 Selected Findings from Extraction of Single crystal Elastic Constants from Fe 3%-Si polycrystalline sample

For this study, extraction of the single crystal elastic constants $\{C_{11}, C_{12}, C_{44}\}$ of the bcc metal Fe 3%-Si which was previously attempted using standard regression techniques was revisited using the Bayesian framework [44]. In the previous study [7], utilizing traditional regression techniques a total of 2286 simulations were needed to establish a high-fidelity reduced-order model in the first step of the two-step protocol. Using Bayesian strategies to select inputs to FE simulations, and establishing the reduced model parameters via BLR, a high fidelity reduced order model was established within 300 simulations (See Figure 2.3). This reduced order model was used for the extraction of single crystal elastic constants using experimental indentation modulus data previously obtained for 11 different orientations shown in Figure 2.4 [7]. A more in-depth discussion of these results can be found in Section 3.4 of this thesis.

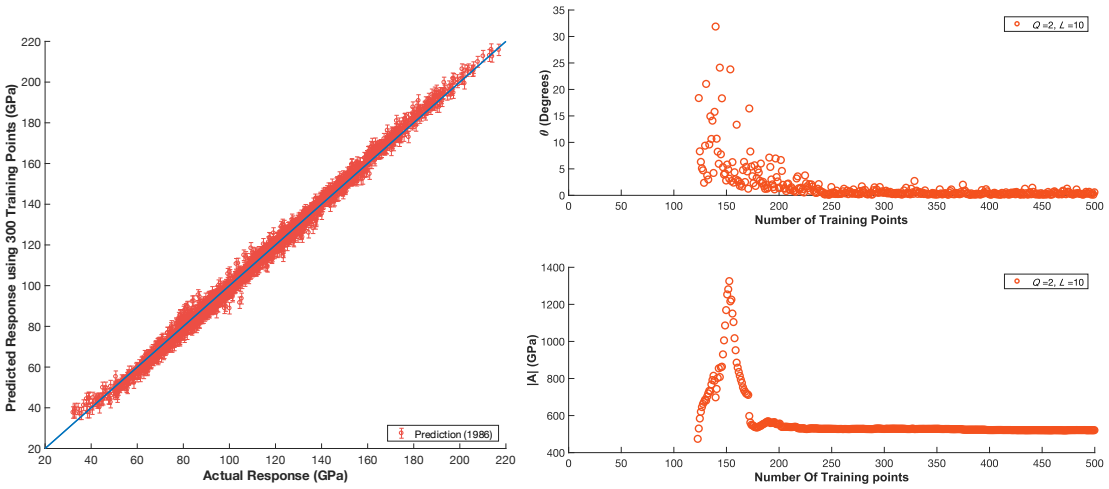

Figure 2.3 Left: Predictive performance of the ROM built using 300 simulations. Predictions are over the 1986 simulations outside the training data set used to establish the ROM. Right: (A) Variation in the angular change in the vector of model coefficients between model update steps. (B) Variation in the magnitude of the vector of model coefficients during the model building process.

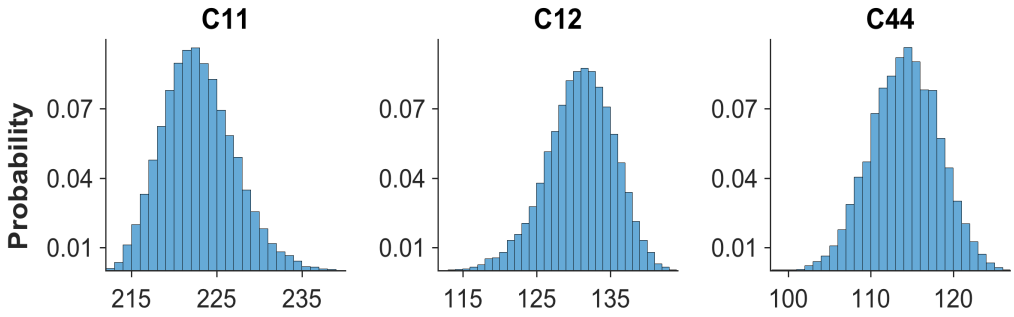

	C11	C12	C44
Mean (GPa)	222.88	130.88	114.13
STDEV	4.15	4.55	4.11

Figure 2.4 MCMC sampling of the multi-variate posterior distribution of the three intrinsic elastic constants for Fe 3% Si.

A follow up study [47] refined the second step in order to sequentially identify specific grains that should be indented to provide the most utility in improving the estimated distributions on the elastic constants extracted using experimental indents from the cubic polycrystalline Fe-3%-Si sample. Selection of additional experiments is continued until the

posterior mean and standard deviation of the parameters exhibit convergence (i.e., only minimal changes with data added from new experiments). To serve as a comparison, random selection of experiments without replacement were also performed several times while utilizing the same initialization. The convergence rate using the information gain (See section 2.2.7) as a selection criteria was compared to cases using random selection as shown in Figure 2.5. Using information gain as the design criteria, the mean of the sampled distribution of elastic constants was found to converge only after three experiments are performed. Additionally, using the information gain design criteria, the standard deviation also appears to converge after three experiments. A more in depth discussion about the computation of the information gain metric can be found in Section 4.4 and further discussion about the results can be found in Section 4.5.

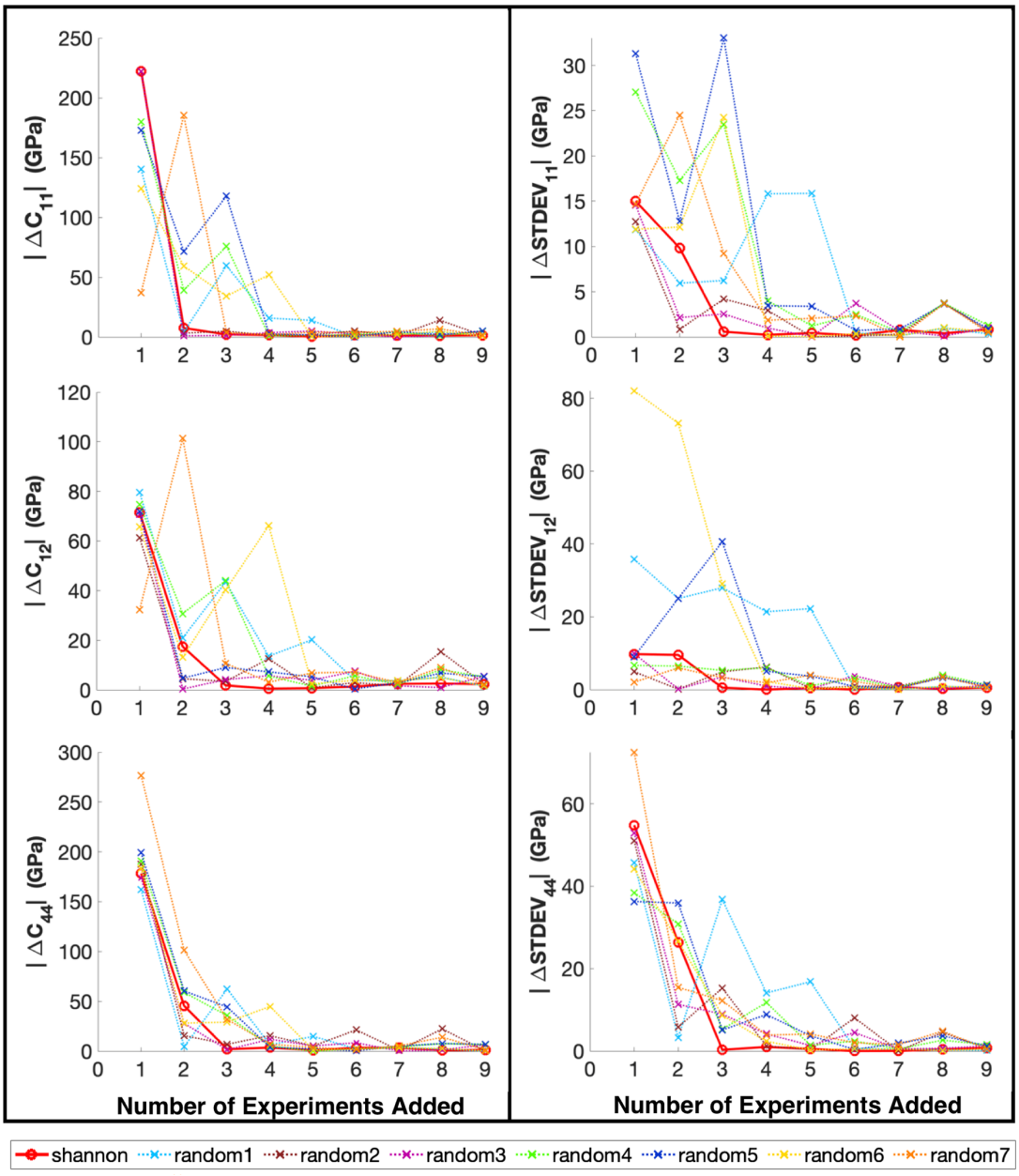

Figure 2.5 Comparison of parameter convergence rates for the sequential selection of experiments based on information gain criteria (shannon) and random selection. Left: Convergence rate for sampled mean {C11, C12, C44} of the MCMC chain. Right: Convergence rate for sampled standard deviation of {C11, C12, C44}. The initialization for all runs is a single orientation chosen such that the [100] crystal direction is close to the sample normal.

2.4.3 Selected Findings from Extraction of Effective Single Ply Elastic Constants from spherical indentation measurements of single ply within multi-laminate samples.

In this study the estimation of effective anisotropic elastic constants of single plies within a IM7/977-3 epoxy-carbon fiber multi-laminate system is demonstrated using previously reported spherical indentation measurements within singular plies [48]. More specifically, the homogenized elastic response of a single ply (each ply is a composite comprising matrix and fibers) can be assumed to exhibit transverse isotropy and is represented by a set of five intrinsic stiffness parameters denoted as C_{11}, C_{12}, C_{13}, C_{33}, and C_{44} ; these five parameters are adequate to fully define the ply's fourth-rank elastic stiffness tensor. It should be noted that the polymer matrix composite (PMC) samples studied here exhibit significantly higher levels of anisotropy and inherent variance in the indentation measurements, when compared to the polycrystalline cubic and hcp metal samples studied in CHAPTER 3. This study demonstrates that the usage of a two-step Bayesian framework enables the extraction of reliable point estimates (and associated distributions) for the effective elastic constants from indentation modulus measurements conducted within single plies at different angles to the fiber orientations. Distributions of effective single ply effective elastic constants extracted in this study are shown in Figure 2.6. An in depth discussion about the results can be found in Section 5.4.2 and development of a reduced order model can be found in Section 5.4.1.

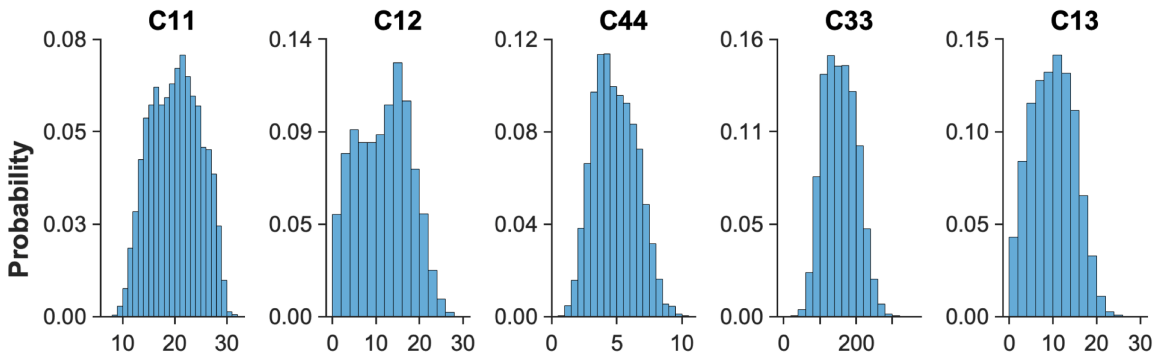

	C11	C12	C44	C33	C13
Mean (GPa)	20.1	11.7	4.9	155.4	9.9
STDEV	4.7	6.1	1.6	45.2	4.9

Figure 2.6 Extracted posterior distributions of the single ply elastic stiffness parameters from the available experimentally measured indentation moduli presented in Table 2.1.

This study further focused on addressing how the distributions of single ply properties are propagated to the effective properties at the multi-laminate scale. The effective elastic properties of a multi-laminate system can be tailored by manipulating the configuration of the constituent plies. Simple homogenization theories have often provided estimates for the effective properties of various configurations of a multi-laminate system. Incorporating the distributions of effective elastic constants (shown in Figure 2.6) into simplified homogenization schemes the effective properties at the next higher length scale were estimated. The expected effective Young's Moduli in the longitudinal direction computed for various configurations of the IM7/977-3 epoxy-carbon fiber multi-laminate system are compared to previously reported experimentally measured values [49] in Table 2.2. The computed expected longitudinal stiffness using the distributions extracted were found to

be in very good agreement with experimentally measured values. A more in depth discussion of these results and homogenization theory used can be found in Section 5.4.3.

Table 2.2. Comparison of homogenized longitudinal Young's Modulus predicted using posterior distributions of single ply elastic stiffness constants to the longitudinal Young's Modulus measured experimentally for multiple multi-laminate configurations.

Multi-laminate Ply Configuration	**Experimental Longitudinal Young's Modulus**	**Expected Longitudinal Young's Modulus**	**STDEV of Expected Longitudinal Young's Modulus**
$[0/+45/90/-45]_{2S}$	58.9	57.6	0.6
$[+60/0/-60]_{3S}$	59.5	57.9	0.6
$[+30/+60/90/-60/-30]_{2S}$	38.1	39.5	0.4

2.4.4 Selected Findings from Extraction of Single crystal Elastic-Plastic properties from spherical indentation measurements in alpha phase of Ti polycrystalline samples

In this study the two step Bayesian framework was used to extract the values for the single crystal elastic constants, $\{C_{11}, C_{12}, C_{44}, C_{13}, C_{33}\}$, as well as the initial slip resistance values $\{s_{pr}, s_{ba}, s_{pyr-a}, s_{pyr-ca}\}$, and associated uncertainties quantified for the hcp primary α phase of different compositions from polycrystalline Ti alloys. It should be emphasized that this study aimed to generate a comprehensive and consistent dataset of single crystal elastic-plastic properties across Ti alloys with varying compositions using available experimental spherical indentation measurements. It should be noted that previous studies involving the extraction of plastic crystal level properties for single phase cubic polycrystalline Fe-3%-Si samples only considered a single slip resistance value [10]. The

extraction effort here was complicated from the previous study by the number of slip resistances necessary to consider. The difficult was further compounded by (i) the plastic anisotropy exhibited in HCP metals (ii) the necessary exploration of the relatively high dimensional parameter space defined by slip resistances and crystallographic single orientations for calibration steps. The extracted distributions of single crystal elastic constants and slip resistances for the aforementioned Ti alloys using the indentation modulus and indentation yield values measured within alpha-grains of various orientations of a polycrystalline sample are shown in Figure 2.7 and Figure 2.8 respectively. Further in depth discussion of the establishment of reduced order model via CPFEM simulations, as well as discussion regarding the associated uncertainties to the distributions reported here are located in Section 6.5.

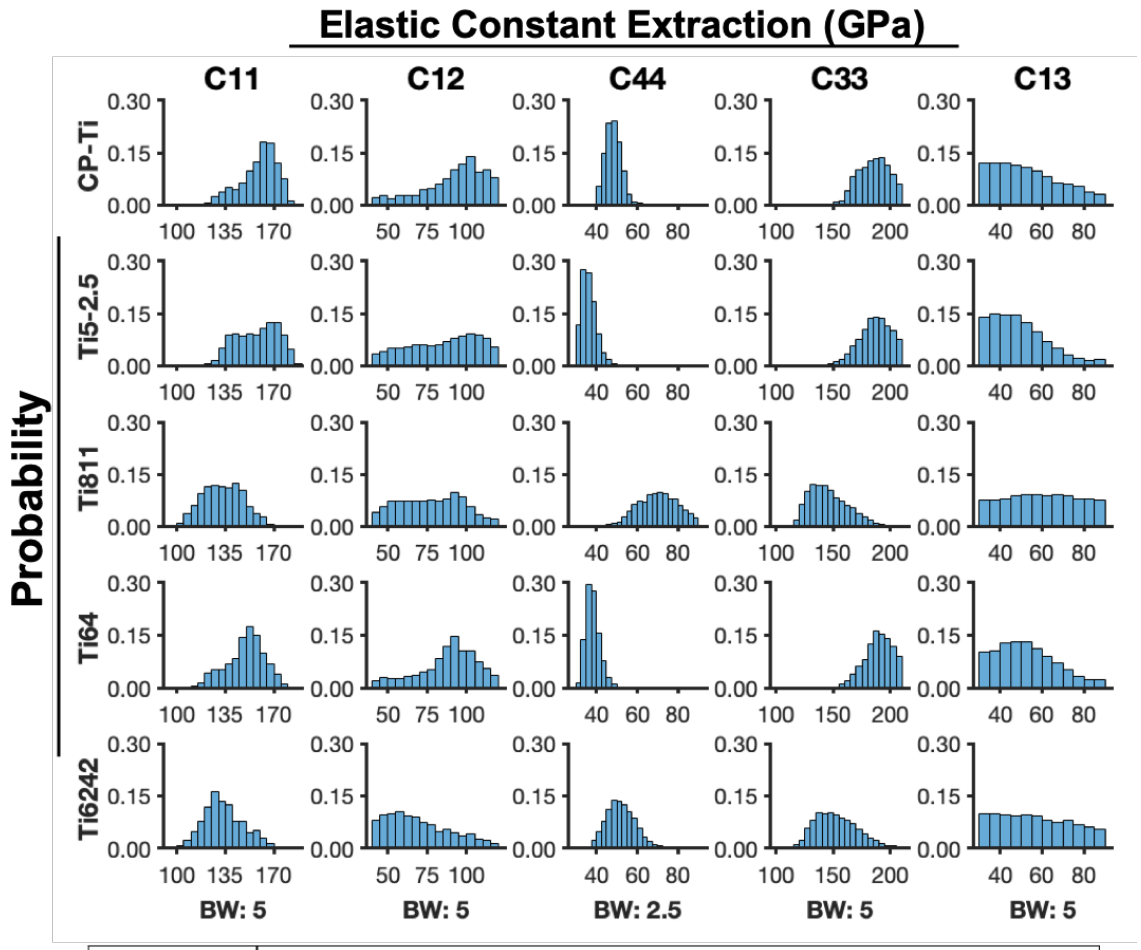

	C11 (GPa)	C12 (GPa)	C44 (GPa)	C33 (GPa)	C13 (GPa)
CP-Ti	159 ± 13	92 ± 19	48 ± 4	185 ± 13	53 ± 16
Ti5-2.5	158 ± 15	85 ± 22	37 ± 4	186 ± 13	49 ± 13
Ti811	133 ± 14	77 ± 20	70 ± 9	146 ± 17	60 ± 17
Ti64	150 ± 14	88 ± 18	38 ± 3	189 ± 12	53 ± 14
Ti6242	134 ± 14	70 ± 20	52 ± 7	153 ± 19	57 ± 17

Figure 2.7 Top: Distributions of single crystal elastic constants extracted for Ti. BW denotes the fixed bin width for the distributions in a given column. Bottom: The mean and corresponding standard deviation of the extracted initial slip resistances are shown.

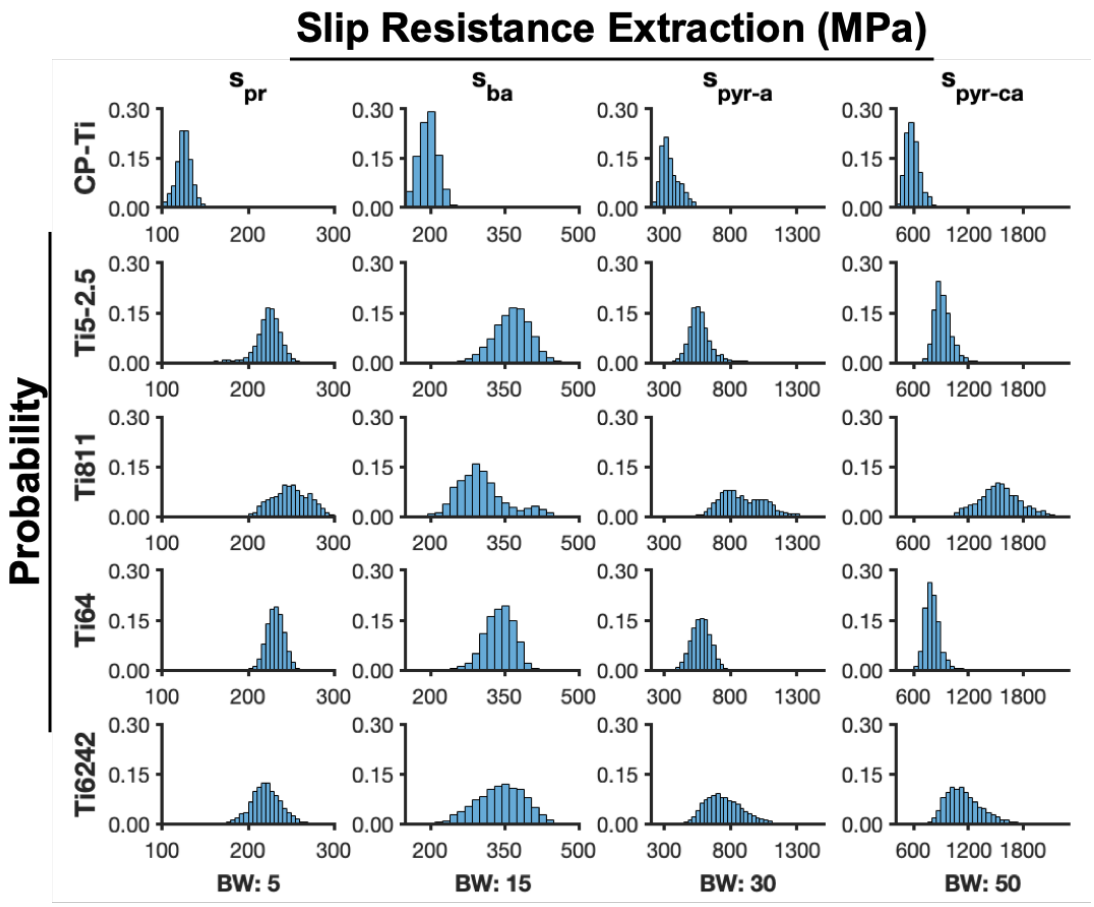

	s_{pr} (MPa)	s_{ba} (MPa)	s_{pyr-a} (MPa)	S_{pyr-ca} (MPa)
CP-Ti	125 ± 9	195 ± 20	346 ± 69	589 ± 77
Ti5-2.5	223 ± 15	366 ± 36	573 ± 96	921 ± 96
Ti811	249 ± 21	304 ± 49	894 ± 165	1546 ± 220
Ti64	231 ± 10	340 ± 30	579 ± 72	804 ± 82
Ti6242	221 ± 18	342 ± 49	748 ± 135	1150 ± 189

Figure 2.8 Top: Distributions of initial slip resistances for Ti alloys. BW denotes the fixed bin width for the distributions in a given column. Bottom: The mean and corresponding standard deviation of the extracted initial slip resistances are shown.

2.4.5 Conclusions

In this work, a statistical framework has been presented for the robust extraction of the intrinsic material parameters from available experimental observations from spherical indentation stress-strain protocols across a broad range of material systems. The two-step

Bayesian inference framework enables the specification of uncertainty in the measurement data, which is then transferred to the uncertainty in the values of the extracted intrinsic material properties. The framework presented here demonstrates potential for significantly speeding up the materials characterization effort by focusing on experiments and simulations that are likely to deliver the maximum value in establishing the desired properties. Finally, the use of a Bayesian framework opens new avenues for the development of autonomous (fully guided by the computer) scientific explorations. It is anticipated that the framework is extensible to a large number of other applications in multiscale materials modeling (e.g., extraction of the values of parameters in phase-field models based on available microstructure datasets). We note in future work it may be highly desirable to use alternative reduced order model forms to the Fourier basis presented here (such as gaussian processes). It is anticipated the introduction of these model forms combined with the framework presented here could further accelerate material characterization efforts.

CHAPTER 3. A BAYESIAN FRAMEWORK FOR THE ESTIMATION OF SINGLE CRYSTAL ELASTIC CONSTANTS FROM SPHERICAL INDENTATIONS MEASUREMENTS IN POLYCRYSTALLINE MATERIALS

The following work was accepted for publication in the Journal, Frontier in Materials, in May 2019 under the title "A Bayesian Framework for the Estimation of the Single Crystal Elastic Parameters from Spherical Indentation Stress-Strain Measurements" [44]. Order of authorship is Andrew R. Castillo, and Surya R. Kalidindi. AC was responsible for data analysis and simulations, SK provided guidance. All contributed to preparation of the manuscript.

3.1 Abstract

This paper presents a two-step Bayesian framework for the estimation of the intrinsic single crystal elastic stiffness parameters from the measurements of spherical indentation stress-strain responses in multiple individual grains of a polycrystalline sample, whose crystal lattice orientations have been measured using electron back-scattered diffraction technique. The first step requires the establishment of the functional dependence of the indentation elastic modulus given the lattice orientation and the intrinsic single crystal elastic stiffness parameters. Previous efforts for this step required a large database of computationally expensive finite element (FE) simulations in order to establish this function with adequate accuracy. In this paper, it is shown that the introduction of a Bayesian framework can

greatly reduce the number of simulations necessary to establish this function, while introducing practically useful measures of uncertainty which can guide the selection of specific additional simulations that are expected to best improve the predictive accuracy of the function. The second step involves a Markov Chain Monte-Carlo (MCMC) sampling of the distribution of possible values for the single crystal elastic stiffness parameters based on a given set of experimentally measured elastic indentation moduli in individual grains of different lattice orientations. This second step is accomplished by calibrating the available experimental data to the function established in the first step. This novel framework is presented and demonstrated in this paper for an as-cast cubic polycrystalline Fe-3% Si sample and a hexagonal polycrystalline commercially pure (CP-Ti) titanium sample.

3.2 Introduction

Continued development and application of physics-based multiscale materials models is largely hampered by the lack of protocols for reliably estimating the intrinsic material properties at the microscale (e.g., the grain-scale properties in modeling of polycrystalline materials). In recent years, instrumented indentation techniques have been demonstrated to be capable of providing consistent and reliable measurements at the lower length scales (up to submicron length scales) [1-5]. Although small-scale mechanical measurements are now quite reliable, it has not been a straightforward process to extract the intrinsic material properties from such measurements. As specific examples, one would hope to estimate the values of the single crystal elastic constants and the critical resolved shear strengths from the instrumented nanoindentation measurements. Reliable and robust protocols for addressing this gap are emergent [6,10,50].

Currently employed strategies for extracting intrinsic material properties from indentation tests have generally involved the calibration of physics-based finite element (FE) models of these tests to the corresponding set of experimental measurements [6-9]. In this regard, it has been pointed out in recent work [10] that these protocols are much more robust when the calibration is attempted in the form of the normalized indentation stress-strain curves as opposed to directly matching the load-displacement curves. This is mainly because the initial elastic response and the elastic-plastic transition occur over a very short early portion of the load-displacement curve that is not easily identified and isolated, resulting in a very high sensitivity of the extracted values of the intrinsic material properties to small changes in the calibration procedures.

The calibration of the FE simulated indentation stress-strain curves to the experimentally measured indentation stress-strain curves for any selected material system essentially involves solving an inverse problem. In other words, the guessed values of the intrinsic material properties of interest become inputs to the FE simulations. Typically, one has to search over a large multidimensional space to find the best-fits between the FE predictions and the measurements. The main challenge comes from the high computational expense of FE simulations of the indentation experiments. It should be noted that establishing each data point on the FE predicted indentation stress-strain curve needs the simulation of a suitable unloading segment [10], and this drives up the cost of the simulation significantly. Given all of the complexity described, the only logical path forward is to establish a reduced-order model for the FE simulations of the indentation test, and to use the reduced-order model in solving the inverse problem described above. In recent work [7], we have formalized this approach as a two-step process: (1) establishing a reduced-order model

calibrated to FE simulations of indentations that takes the relevant intrinsic material properties as inputs and predicts indentation properties (defined suitably on an indentation stress-strain curve), and (2) the extraction of the intrinsic material properties from the available measurements (typically performed on grains of different orientations in a polycrystalline sample) through calibration with the reduced-order model established in step (1). The second step described above typically involves the solution to an optimization problem (i.e., minimizing the difference between the measurements and the predictions from the reduced-order model). The viability of this two-step protocol for extracting the values of the single crystal elastic constants and the critical resolved shear strengths in Fe-3%-Si has been demonstrated in recent work [7,10].

The main difficulty with the two-step protocol described above lies in building the reduced-order model (i.e., step (1)). Because of the need to cover a large space (for example for extracting single crystal elastic constants, the input space of interest is the product space spanning all combinations of the single crystal elastic constants, C_{11}, C_{12}, C_{44}, and all possible grain orientations), one needs to generate a large amount of the FE simulation data in order to establish a high-fidelity reduced-order model. The difficulty of this task is amplified significantly in dealing with hcp crystals, where the numbers of the intrinsic properties is significantly larger (for example, modeling the elastic deformation in hcp crystals requires specification of five independent single crystal elastic constants). In prior work [7], the reduced-order models were built using standard regression approaches. Although these regression approaches produced excellent results, they do not scale well to problems with larger numbers of the intrinsic properties (because of the need to generate a large amount of data spanning the entire input domain).

The primary goal of this paper is to demonstrate the utility of Bayesian strategies for (i) optimizing the reduced-order model building effort involved in step (1), and (ii) providing estimates of the desired intrinsic material parameters (single elastic constants specifically) with uncertainty measures from available experimental data (spherical indentation measurements). Towards these goals, we will develop and present a Bayesian inference framework for both steps of the two-step protocol described above. Bayesian inference has been instrumental in model-building tasks with limited amount of data [33,34,42,43]. The adoption of a Bayesian inference framework for the extraction of the intrinsic material properties from indentation measurements offers the following main advantages: (i) it is expected to dramatically reduce the number of FE simulations needed to produce the reduced-order model generated in step (1), and (ii) it provides a much more rigorous quantification of the uncertainty in the estimates of the intrinsic material properties obtained in step (2), while accounting for the uncertainty in the measurements as well as other sources. In this paper, we first develop the framework, and subsequently demonstrate its application to the extraction of single crystal elastic properties in selected cubic and hexagonal metals.

3.3 New Bayesian Inference Framework for the Estimation of Intrinsic Material Properties from Indentation Measurements

Let $\boldsymbol{c}$ denote the set of intrinsic material properties to be established. For cubic crystals, this represents the set of three elastic constants, i.e., $\boldsymbol{c} = \{C_{11}, C_{12}, C_{44}\}$. Let $\boldsymbol{P}$ denote an available set of observations of the indentation properties corresponding to the set of crystal orientations $\boldsymbol{G}$. This set of observations could come from either FE simulations or the physical experiments. We shall note the source of the data using subscripts *sim* and *exp* on

these variables. Furthermore, in the notation employed in this paper, a set of values for a variable is denoted by an upper-case symbol, while an individual element of the set is denoted by its non-bold counterpart. As an example, a single value of the indentation property will be denoted by P. Furthermore, a collection of variables is also denoted by bold symbols. As an example, a single value of the crystal orientation would be denoted by $\boldsymbol{g}$, as it denotes a set of three Bunge-Euler angles [22]. However, a set of grain orientations would be represented by $\boldsymbol{G}$. Likewise, a single set of intrinsic material parameters is denoted by $\boldsymbol{c}$, whereas a collection of the sets of intrinsic material parameters is denoted $\boldsymbol{C}$. Employing this notation, the central tasks in the two-step protocol developed in this work are the following:

Establish a reduced-order model that takes given values of $\boldsymbol{c}$ and $\boldsymbol{g}$ and predicts the indentation property of interest, $P = \hat{P}(\boldsymbol{c}, \boldsymbol{g})$, while employing Bayesian inference in building the reduced-order model. In other words, given the previously aggregated set of simulation data $\{\boldsymbol{P}_{sim}, \boldsymbol{G}_{sim}\}$, determine the new inputs for the FE simulation that would yield the best improvements in the reliability of the reduced-order model being built.

Given the reduced-order model built in step (1) and a set of experimental observations $\{\boldsymbol{P}_{exp}, \boldsymbol{G}_{exp}\}$ from a given polycrystalline sample, establish the posterior distribution on $\boldsymbol{c}$ for the sample. It is noted that the indentation properties are measured by the spherical indentation protocols mentioned earlier, while the orientations are measured using electron back-scattered diffraction (EBSD) techniques [51].

Prior experimental work [13] in single-phase polycrystalline metals has focused on exploring the dependence of indentation modulus on the lattice orientation of the indented

grains (i.e., individual crystals). These findings were verified by suitable FE simulations [7]. Recently, a reduced-order model which captures the dependence of indentation modulus on both orientation and an arbitrary set of intrinsic material parameters has been established from FE simulations. The mathematical form of the reduced-order model for the present application is adopted from this prior work [7] as

$$P = \hat{P}(\boldsymbol{c}, \boldsymbol{g}) \approx \sum_{l=0}^{L} \sum_{m=1}^{M(l)} \sum_{\boldsymbol{q}}^{\boldsymbol{Q}} A_l^{mq} \mathrm{K}_l^m(\boldsymbol{g}) \widetilde{\mathrm{P}}^{\boldsymbol{q}}(\bar{\boldsymbol{c}}) \tag{3.1}$$

$$\bar{c}_j = \frac{2c_j - c_j^{min} - c_j^{max}}{c_j^{max} - c_j^{min}} \tag{3.2}$$

where $\mathrm{K}_l^m(\boldsymbol{g})$ denote the symmetrized Surface Spherical Harmonics basis over the relevant orientation space of interest, and $\widetilde{\mathrm{P}}^q(\,)$ denote a multivariate Legendre polynomial product basis. In other words, one can express $\widetilde{\mathrm{P}}^{\boldsymbol{q}}(\bar{\boldsymbol{c}}) = \mathrm{P}^{q_1}(\bar{c}_1)\mathrm{P}^{q_2}(\bar{c}_2) \ldots \mathrm{P}^{q_R}(\bar{c}_R)$, where $\boldsymbol{q} = (q_1, q_2 \ldots q_R)$ forms a multi-index array, each element of which is a nonnegative integer allowed to vary from 0 to the selected maximum degree, Q, i.e., $q_j \in [0, Q]$. The use of Legendre polynomials provides an orthonormal basis over the range [-1,1], for which each of the elastic constants are rescaled in accordance to Eqn. (3.2), where c_j^{max} and c_j^{min} are the maximum and minimum values of the j-th elastic constant under consideration. In Eqn. 3.1, $M(l)$ enumerates the spherical harmonics that implicitly reflect the crystal symmetries of interest [22,23]. The integers Q and L denote the truncation levels adopted in the use of Eqn. 3.1. It is emphasized here that the model form used in Eqn. 3.1 denotes a Fourier representation using an orthonormal basis that has been previously shown to produce compact representations for mechanical responses of crystalline solids [7,10,24-27]. One

of the central features of a Fourier representation is that the Fourier coefficients A_l^{mq} are completely independent of each other. The goal of the reduced-order modeling task here is to estimate the values of A_l^{mq}, expressed in a vector notation as $\boldsymbol{A}$, from the sparse amount of available data, as it is being generated from the expensive FE simulations. Even more importantly, our goal is to drive the model building in an optimal way by identifying the specific set of inputs for the next FE simulation such that it maximizes the improvement to the reduced-order model being built.

3.3.1 Building the Reduced-Order Model

The reduced-order model (see Eqn. 3.1) needs to be built such that it makes good predictions for the indentation modulus over a large domain of input parameters $(\boldsymbol{c}, \boldsymbol{g})$. Given the large domain of the input parameters (e.g., covering the range of values for the three independent parameters defining cubic elasticity and the two independent parameters defining the indentation direction in the crystal reference frame) and the high cost of executing a FE simulation for generating each data point, it is highly desirable to explore Bayesian regression approaches for estimating the unknown Fourier coefficients in Eqn. 3.1. The data generated from FE simulations will be denoted $\{\boldsymbol{P}_{sim}, \boldsymbol{C}_{sim}, \boldsymbol{G}_{sim}\}$ following the notation introduced earlier.

Bayesian approaches treat model parameters (e.g., Fourier coefficients in Eqn. 3.1) as stochastic variables exhibiting a distribution of values. Most importantly, Bayes' theorem allows one to update the distributions for the model parameters given new data (i.e., observations) and is commonly expressed as

$$P(A|D) = \frac{P(D|A)P(A)}{P(D)} \tag{3.3}$$

where $P(A)$ denotes the prior belief (expressed as a distribution) on the values of the unknown model parameters, $P(D|A)$ denotes the likelihood of sampling the observations D for specified values of the model parameters, and $P(A|D)$ denotes the posterior (updated) belief on the values of the unknown model parameters given the observations D. The denominator $P(D)$ in Eqn. (3.3) is generally referred as the probability of the evidence, and is often difficult to establish. However, it mainly serves as a normalization factor for the posterior distribution. Since the distributions are often defined with known normalization factors, it is often possible to skip the evaluation of $P(D)$ in practical implementations of the Bayes' rule described in Eqn. (3.3) [28].

It is expedient to treat the distributions associated with all the stochastic variables in Eqn. (3.3) as normal (i.e., Gaussian) distributions. As a specific example, the ith observed value of the indentation modulus is modeled as being generated from a deterministic model, with added stochastic noise, as

$$P_i = \hat{P}_i(\boldsymbol{A}, \boldsymbol{c}_i, \boldsymbol{g}_i) + \varepsilon_i, \quad \varepsilon_i \sim \mathcal{N}(0, \beta^{-1}) \tag{3.4}$$

where $\mathcal{N}(0, \beta^{-1})$ denotes a normal distribution with a zero mean and a variance of β^{-1}. Note that the stochastic noise is assumed to be independent of location in the parameter space, i.e., homoscedastic. The likelihood for a set of N independently observed indentation moduli can be established using the product rule as

$$p(\boldsymbol{P_{sim}}|\boldsymbol{A}, \boldsymbol{C_{sim}}, \boldsymbol{G_{sim}}, \beta) = \prod_{i}^{N} p(P_i|\boldsymbol{A}, \boldsymbol{c}_i, \boldsymbol{g}_i, \beta) \tag{3.5}$$

As noted earlier, the model parameters $\boldsymbol{A}$ are also treated as stochastic variables. The prior belief on these variables is assumed to be specified by a normal distribution with a zero mean and a large variance of α^{-1} as

$$p(\boldsymbol{A}|\alpha) \sim \mathcal{N}(0, \alpha^{-1}\boldsymbol{I}) \tag{3.6}$$

The application of Bayes' rule (Eqn. (3.3)) to the problem at hand results in

$$p(\boldsymbol{A}|\boldsymbol{P_{sim}}, \boldsymbol{C_{sim}}, \boldsymbol{G_{sim}}, \alpha, \beta) = \frac{p(\boldsymbol{P_{sim}}|\boldsymbol{A}, \boldsymbol{C_{sim}}, \boldsymbol{G_{sim}}, \beta)\, p(\boldsymbol{A}|\alpha)}{p(\boldsymbol{P_{sim}}|\boldsymbol{C_{sim}}, \boldsymbol{G_{sim}}, \alpha, \beta)} \tag{3.7}$$

where $p(\boldsymbol{A}|\boldsymbol{P_{sim}}, \boldsymbol{C_{sim}}, \boldsymbol{G_{sim}}, \alpha, \beta)$ denotes the posterior (updated) distribution on the model parameters. The denominator in Eqn. (3.7) reflects the probability of the observed outcomes irrespective of the model parameters $\boldsymbol{A}$ chosen, and can be described by the marginalization of the likelihood with respect to the model parameters as

$$p(\boldsymbol{P_{sim}}|\boldsymbol{C_{sim}}, \boldsymbol{G_{sim}}, \alpha, \beta) = \int_{\boldsymbol{A}} p(\boldsymbol{P_{sim}}|\boldsymbol{A}, \boldsymbol{C_{sim}}, \boldsymbol{G_{sim}}, \beta)\, p(\boldsymbol{A}|\alpha) d\boldsymbol{A} \tag{3.8}$$

In a fully Bayesian approach, the precision parameters, α, β, may also be treated as stochastic variables [34]. This allows for a separate application of Bayes' theorem expressed as

$$p(\alpha, \beta | \boldsymbol{P_{sim}}, \boldsymbol{C_{sim}}, \boldsymbol{G_{sim}}) \propto p(\boldsymbol{P_{sim}} | \boldsymbol{C_{sim}}, \boldsymbol{G_{sim}}, \alpha, \beta) p(\alpha, \beta) \tag{3.9}$$

Alternately, one can use point estimates from the maximization of the likelihood in Eqn. (3.9), denoted as $\hat{\alpha}, \hat{\beta}$. This is equivalently interpreted as the maximization of the evidence of the observed data in Eqn. (3.8) [30]. With this approach, the posterior distributions of model coefficients in Eqn. (3.7) can be solved analytically (while assuming normal distributions for the various variables involved) [30-32]. The updated posterior distribution computed using the approach described above is generally expected to be sharper (i.e., lower variance) compared to the prior belief.

Obviously, the available observations may not produce a posterior distribution that is sharp enough (i.e., the uncertainty associated with the posterior is still too high for a given application). In such cases, one needs to examine carefully where one should produce additional data points (i.e., new observations) in order to maximize the sharpening of the posterior distributions. The general approach to solving this problem (i.e., identifying the new data points exhibiting the maximum potential for improving the model accuracy and reliability) involves making predictions for new inputs, and identifying the specific inputs that exhibited the highest variance (i.e., uncertainty) in their predictions as the locations where new observations should be generated [46,52]. This kind of a rational approach for deciding where to generate new data points is critical for situations where data generation is expensive (as is the case with the FE simulations of the spherical indentation for the present case study). The predictions for new inputs are obtained by the marginalization over the posterior distribution of the model parameters as

$$p\left(P\middle|\boldsymbol{c},\boldsymbol{g},\boldsymbol{P_{sim}},\boldsymbol{C_{sim}},\boldsymbol{G_{sim}},\hat{\alpha},\hat{\beta}\right) = \int_{\boldsymbol{A}} p\left(P\middle|\boldsymbol{A},\mathbf{c},\mathbf{g},\hat{\beta}\right) p\left(\boldsymbol{A}\middle|\boldsymbol{P_{sim}},\boldsymbol{C_{sim}},\boldsymbol{G_{sim}},\hat{\alpha},\hat{\beta}\right) d\boldsymbol{A} \tag{3.10}$$

where $(\boldsymbol{c},\boldsymbol{g})$ denote the new inputs. Therefore, the specific set of inputs which exhibit the highest variance for the prediction can be readily identified. Once the set of inputs are identified, and corresponding FE simulation performed, the next step is updating the distribution of model coefficients with the newly acquired observation. The update step to the distribution of the model coefficients is natural using a Bayesian framework in the sense that any knowledge acquired previously can be incorporated through the prior.

$$\begin{aligned} &p_{N+1}\left(\boldsymbol{A}\middle|\boldsymbol{P_{sim}},\boldsymbol{C_{sim}},\boldsymbol{G_{sim}},\hat{\alpha},\hat{\beta}\right) \\ &\propto p_{N+1}\left(\boldsymbol{P_{sim}}\middle|\boldsymbol{A},\boldsymbol{C_{sim}},\boldsymbol{G_{sim}},\hat{\beta}\right) p_N\left(\boldsymbol{A}\middle|\boldsymbol{P_{sim}},\boldsymbol{C_{sim}},\boldsymbol{G_{sim}},\hat{\alpha},\hat{\beta}\right) \end{aligned} \tag{3.11}$$

The posterior distribution of the parameters can continually be updated as incoming data is sequentially added by setting the prior as the previously inferred posterior distribution of model coefficients as shown in Eqn. (3.11). Updates to the posterior distribution of model coefficients are performed until sufficient model convergence and prediction performance is attained. Model convergence is determined through the change in values of the model coefficients and parameters as data is added. Model performance is evaluated through various error metrics such as the leave-one-out-cross-validation (LOOCV) error [30,31]. Building the reduced-order model and critically evaluating its reliability and robustness completes the first step of the two-step protocol. It should be noted that this is intended to be performed only once for a given class of materials.

3.3.2 Estimating Intrinsic Material Properties from Indentation Measurements

For the second step of the protocol, our goal is to employ the reduced-order model built in the first step together with indentation measurements obtained from a given sample to estimate its intrinsic material properties. Let $\{\boldsymbol{P}_{exp}, \boldsymbol{G}_{exp}\}$ denote such experimental measurements. The posterior distribution for the intrinsic material properties can be sampled from yet another application of the Bayes' rule as

$$p(\boldsymbol{c}|\boldsymbol{A}, \boldsymbol{P}_{exp}, \boldsymbol{G}_{exp}, \boldsymbol{\sigma}) \propto p\left(\boldsymbol{P}_{exp}\middle|\boldsymbol{A}, \boldsymbol{c}, \boldsymbol{G}_{exp}, \boldsymbol{\sigma}\right)p(\boldsymbol{c}) \tag{3.12}$$

where $\boldsymbol{A}$ denotes the parameters in the reduced-order model built in the first step. Although point estimates can be obtained by maximizing the likelihood in Eqn. (3.12), in the spirit of building a robust framework capable of accounting for various sources of uncertainty, we have decided to pursue the computation of the posterior distribution on the intrinsic material properties through sampling techniques. In order to sample from the posterior distribution defined in Eqn. (3.12), we need to establish the likelihood of the set of experimental observations. A likelihood can be constructed by assuming that the experimental observations (i.e., data points) are independent and normally distributed, i.e., the experimental data points are observations drawn from normal distributions with means estimated by the reduced order model and variances, $\boldsymbol{\sigma}$, estimated from the experimental data of the measured indentation property at M grain orientations [3,28,37,53]. This likelihood is expressed as

$$p(\boldsymbol{P}_{exp}|\boldsymbol{A},\boldsymbol{c},\boldsymbol{G}_{exp},\boldsymbol{\sigma}) = \prod_{i}^{M} \mathcal{N}(P_{i_{exp}}|\hat{P}(\boldsymbol{A},\boldsymbol{c},\boldsymbol{g}_{i_{exp}}),\sigma_i) \tag{3.13}$$

The evaluation of the likelihood described in Eqn. (3.13) is performed using the reduced-order model, $\hat{P}(\boldsymbol{A},\boldsymbol{c},\boldsymbol{g})$, built in the first step of the two-step protocol. In this work, the sampling from the posterior distribution of intrinsic material parameters (Eqn. (3.12)) is accomplished using Markov Chain Monte Carlo (MCMC). The goal of MCMC is to generate a Markov Chain which indirectly samples from the posterior distribution of interest as long as the number of samples drawn is very large. The Markov Chain is generated by the acceptance and rejection of a large number of transitions through the space of intrinsic material parameters based on an acceptance probability. In practice, a class of algorithms have been developed in order to define these transitions and are referred as Metropolis-Hastings algorithms [34]. In this work, Single Component Metropolis Hastings (SCMH) is applied, which considers component wise transitions [35]. In the algorithm below for a given step t, partial updates are performed for the sample $\boldsymbol{c}_t$ for each component j until all components are updated.

The basic steps for the implementation of the SCMH algorithm are as follows:

6. Initialize a starting point, $\boldsymbol{c}_0$, using the best available information
7. Sample transition, $\boldsymbol{c}^*$, from a proposal distribution $q_j(*)$ for an update of component j. If t is a new step, initialize $\boldsymbol{c}_t = \boldsymbol{c}_{t-1}$ where $\boldsymbol{c}_t$ will be subjected to partial updates (one component at a time). Mathematically, one can express this as

$$\boldsymbol{c}^* \sim q_j(\boldsymbol{c}|\boldsymbol{c}_t)$$

where $q_j(*)$ proposes $\boldsymbol{c}^*$ differing from $\boldsymbol{c}_t$ in component j, sampled from a normal distribution with mean c_t^j and variance v_j^2

$$c^{j^*} \sim \mathcal{N}\left(c^j | c_t^j, v_j^2\right)$$

8. Calculate the acceptance probability of transition, $\alpha(*)$

$$\alpha(\boldsymbol{c}^* | \boldsymbol{c}_t) = \min\left(1, \frac{p\left(\boldsymbol{c}^* \middle| \boldsymbol{A}, \boldsymbol{P}_{exp}, \boldsymbol{G}_{exp}, \boldsymbol{\sigma}\right) q_j(\boldsymbol{c}_t | \boldsymbol{c}^*)}{p\left(\boldsymbol{c}_t \middle| \boldsymbol{A}, \boldsymbol{P}_{exp}, \boldsymbol{G}_{exp}, \boldsymbol{\sigma}\right) q_j(\boldsymbol{c}^* | \boldsymbol{c}_t)}\right)$$

$$= \min\left(1, \frac{p\left(\boldsymbol{P}_{exp} \middle| \boldsymbol{A}, \boldsymbol{c}^*, \boldsymbol{G}_{exp}, \boldsymbol{\sigma}\right) p(\boldsymbol{c}^*)}{p\left(\boldsymbol{P}_{exp} \middle| \boldsymbol{A}, \boldsymbol{c}_t, \boldsymbol{G}_{exp}, \boldsymbol{\sigma}\right) p(\boldsymbol{c}_t)}\right)$$

9. Update Chain (accept/reject proposed transition)
    a. Draw a sample, r, from a standard uniform distribution
    b. If $\alpha > r$

$$\boldsymbol{c}_t = \boldsymbol{c}^*$$

10. Repeat steps (2-4) until all components of $\boldsymbol{c}_t$ are updated, then proceed to a new step.

While the probability of a proposed transition is described by the proposal distribution $q_j(*)$, the probability of accepting the transition is given by $\alpha(*)$. By assuming a flat prior for $p(\boldsymbol{c})$, the acceptance probability of a proposed transition is completely specified by the posterior probability of the states evaluated within a normalizing constant using Eqn. (3.13) [34,36]. The variances of the proposal distributions v_j^2 are tuned during the "burn-in" period in order to meet an acceptance rate around ~0.23. Ensuring the acceptance rate lies around 0.23 has been shown to provide efficient convergence of the Markov chain for

gaussian posteriors [37]. All of the computations described above were realized using functions readily available in MATLAB [54].

3.4 Case Study: Cubic Polycrystals

3.4.1 Problem Statement

For our first case study, we revisit the extraction of the single crystal elastic constants $\{C_{11}, C_{12}, C_{44}\}$ of the bcc metal Fe 3%-Si, which was previously attempted using standard regression techniques. In the previous study, a total of 2286 simulations were needed to establish a high-fidelity reduced-order model in the first step of the two-step protocol. The simulated database consisted of the indentation modulus corresponding to 300 distinct sets of cubic stiffness constants within the domain $50\ \text{GPa} \leq C_{11} \leq 250\ \text{GPa}$, $40\ \text{GPa} \leq C_{12} \leq 150\ \text{GPa}$ and $15\ \text{GPa} \leq C_{44} \leq 120\ \text{GPa}$ across 9 orientations selected within the fundamental zone of the relevant orientation space [7]. It is anticipated that the proposed Bayesian framework will need significantly less FE simulations to adequately capture the FE predicted indentation modulus within the same parameter space in a robust reduced-order model.

3.4.2 Model Building Process

The Bayesian model building process enables sequential design strategies through the identification of high value simulations which will best improve the predictive capability of the model. Since a database of simulations is already available, simulations are treated as "unseen" and are sampled based on the determined utility of performing the simulation.

Before beginning the sequential design process, an initial set of simulations must be performed to establish an initial model.

For the present study, a set of 123 FE simulations were selected from the previously performed 2286 simulations as this initial set. This initial set was selected to correspond to the boundaries of the intrinsic material parameter space. Following initialization, the reduced-order model in Eqn. 3.1 was considered with different truncation levels of L=8,10,12 for the symmetrized Surface spherical harmonics and Q=1,2,3 for the maximal degree of the respective Legendre Polynomials [22]. The truncation levels of the reduced-order model can be treated as hyperparameters, and must be selected so that we produce the most robust and accurate reduced-order models. Leave-one-out-cross-validation (LOOCV) was performed at various times during the update process and plotted in Figure 3.1 for the different truncation levels considered.

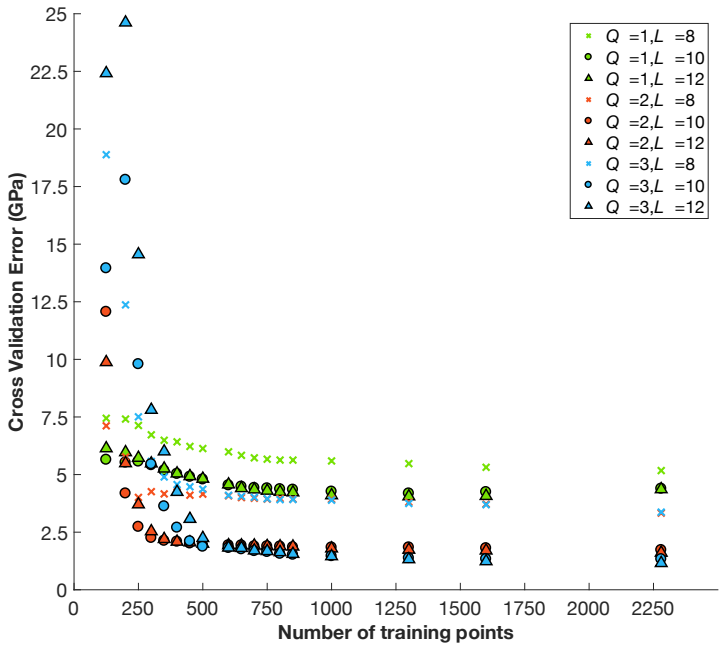

Figure 3.1. Cross validation error of the reduced-order model built in the first step of the two-step protocol for different truncation levels in Eqn3.1).

There is clear improvement in cross validation error up to truncations levels Q=2, L=10, with little improvement for higher truncation levels. The plots in this figure also provide guidance on where to stop the model building effort (i.e., when there is no appreciable improvement in the accuracy of the reduced-order model being built). In addition to the LOOCV, the norm of the vector of model coefficients at each update step (see Figure 3.2b) and the angular difference of the vector of model coefficients from the previous update step (see Figure 3.2a) were taken into consideration in determining when to stop the model building effort. Based on these considerations (see Figure 3.1, Figure 3.2a, and Figure 3.2b) it was decided to stop the model building effort after using 300 training points (this includes the set of 123 training point used for initialization). The predictive accuracy of the reduced-order model for the remaining FE simulations (i.e., 2286-300 = 1986) is presented in Figure 3.3 as a parity plot. The resulting mean absolute prediction error of the reduced-order model was found to be 2.16 GPa (see Figure 3.3) while the LOOCV error was found to be 2.22 GPa (see Figure 3.1). This is comparable to previous efforts based on standard regression techniques and utilizing the full database of 2286 FE simulations, where the LOOCV error was reported to be in the range of 2-2.5 GPa [7].

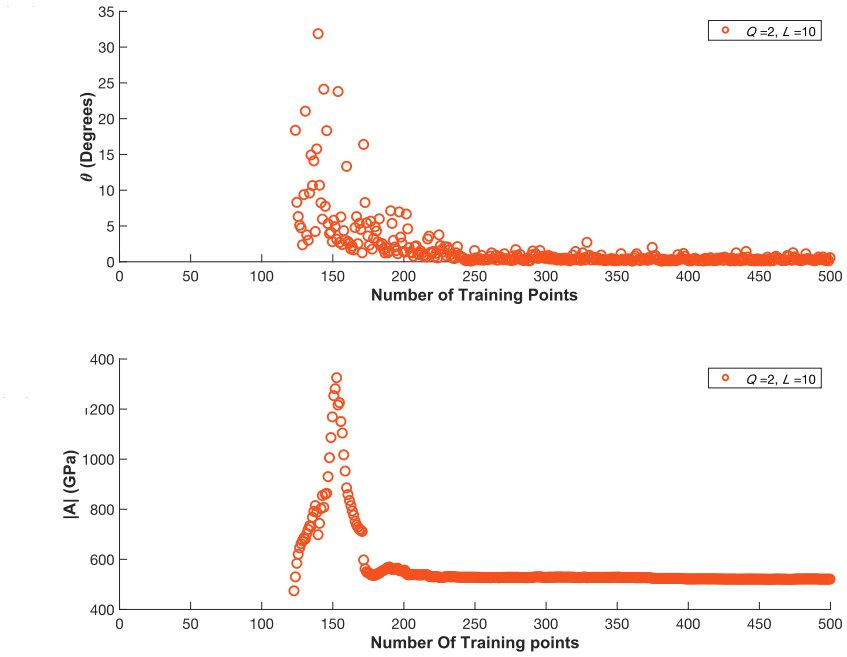

Figure 3.2. (A) Variation in the angular change in the vector of model coefficients between model update steps. (B) Variation in the magnitude of the vector of model coefficients during the model building process.

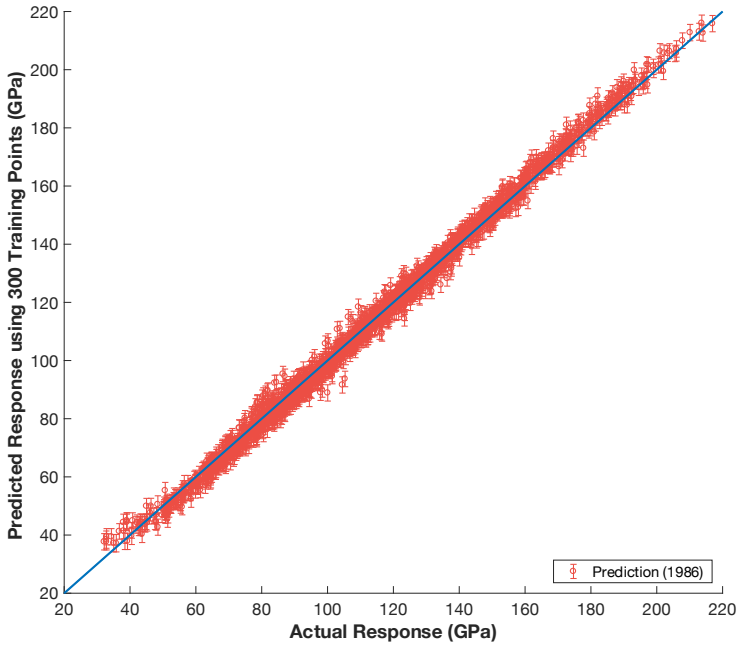

Figure 3.3. Predictions for the 1986 FE simulated indentation moduli not used in the training of the reduced-order model. A single standard deviation from the predicted mean is also shown in the plot for each prediction.

3.4.3 Extracting Intrinsic Material Parameters

At any point during the model building process, the Bayesian framework presented in Section 3.3.1 can be used to sample the posterior distribution on the material parameters via the MCMC approach. In order to accomplish this second step of the proposed framework, one needs to evaluate the likelihood function (see Eqn. (3.13)); this requires the use of the reduced-order model obtained in step (1) as well as the relevant experimental indentation data. The reduced-order model with truncations Q=2, L=10 obtained after using 300 training points (described in Section 3.4.2) was selected for this example case study. Experimental data, including the mean and associated variance of measured indentation moduli, were previously reported for 11 different grains in a polycrystalline sample of Fe 3%-Si [13]. Using the MCMC procedure described in Section 3.3.2, 50000 samples were drawn. The resulting multivariate distribution is shown in Figure 3.4 as three univariate distributions.

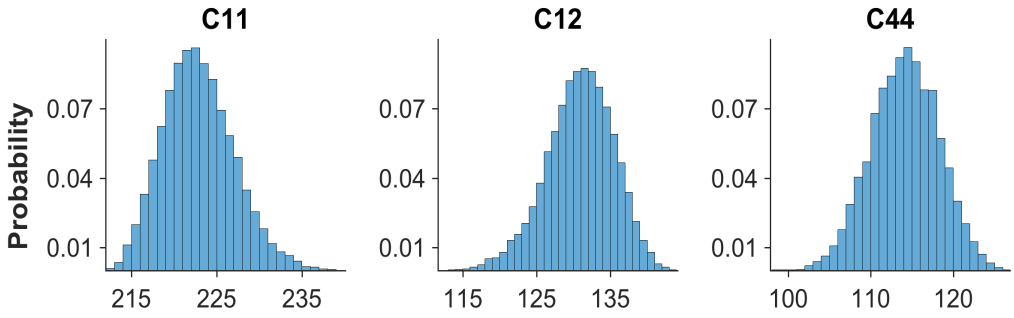

	C11	C12	C44
Mean (GPa)	222.88	130.88	114.13
STDEV	4.15	4.55	4.11

Figure 3.4. MCMC sampling of the multi-variate posterior distribution of the three intrinsic elastic constants for Fe 3% Si.

To recap, in Step (1) of the protocol used a minimal number of finite element simulations to establish a high fidelity reduced-order model. Using experimental data previously reported, [13] the established reduced-order model was used to sample the distribution of elastic constants in Step (2) of the protocol. The distributions for the parameters extracted here are in very good agreement with the literature values. Estimates of the elastic constants from the current study, typical values reported from literature [55], and estimates reported from the previous study based on ordinary regression (on the full set of 2286 FE simulations) [7] are shown in Table 3.1.

It is emphasized that the previous study did not attempt any form of uncertainty quantification with respect to these estimates. It is important to note that the highest relative uncertainty in the present study was associated with the estimation of C_{44}, which deviated the most from the reported literature values. Since the literature values seldom report the associated uncertainty, it is very difficult to identify the source of the small disagreement between the C_{44} values extracted here from the indentation measurements and the literature values obtained using completely different techniques. This small difference could be attributed to the experimental measurement errors (in both the indentation protocols employed here as well as the more conventional measurement protocols employed in literature). We further note that it should be possible to further refine the methodology presented here (i.e., Step (2) of the protocol) to identify specific additional grain orientations for indentation measurements that might improve specifically the estimates of C_{44} by reducing its variance. Such refinements will be pursued in future work.

Table 3.1. Comparison of reported estimates for single crystal elastic constants of the bcc-metal, Fe-3%-Si. All units are in GPa.

	C_{11}	C_{12}	C_{44}
Literature[a]	225	135	124
Previous Study[b]	216	132	122
Current Study	223	132	114

a. Simmons and Wang
b. Patel et al.

3.5 Case Study: Hexagonal Polycrystals

3.5.1 Problem Statement

In order to demonstrate the versatility of the proposed framework, attention is now turned to the extraction of the elastic constants, $\boldsymbol{c} = \{C_{11}, C_{12}, C_{44}, C_{33}, C_{13}\}$, for the hcp metal CP-Ti (commercially pure titanium) [55]. Unlike the previous case study, a database of previously performed FE simulations was not readily available for this case study. Therefore, FE simulations were designed and performed specifically for this study as demanded by the Bayesian inference framework in the Step (1) of the protocol.

The FE model used for this study is the previously validated Finite Element model [7] developed using the commercial software ABAQUS [56]. The sample mesh consisted of 12,610 C3D8 continuum 3-D elements and is shown in Figure 3.5. The simulated indents were performed using an analytically defined rigid indenter with a tip radius of 16 μm,

consistent with the size used in the experiments on single crystal CP alpha-Ti grains reported in literature [1]. The dimensions of the sample mesh were taken as 9.6 μm X 9.6 μm X 4.8 μm. The FE model was validated by comparing simulated indentation moduli to the theoretical values reported by Vlassak and Nix [5] for zinc single crystals $\boldsymbol{c} = \{161.1, 34.2, 38.3, 61.1, 50.3\}\ GPa$ as shown in Figure 3.5. The comparisons confirm the linear relationship between the indentation load (P) and the elastic indentation depth (h_e) raised to a power of 3/2 for hcp single crystals, as predicted by Vlassak and Nix [5] (note that the original Hertz theory [11] is restricted to isotropic materials).

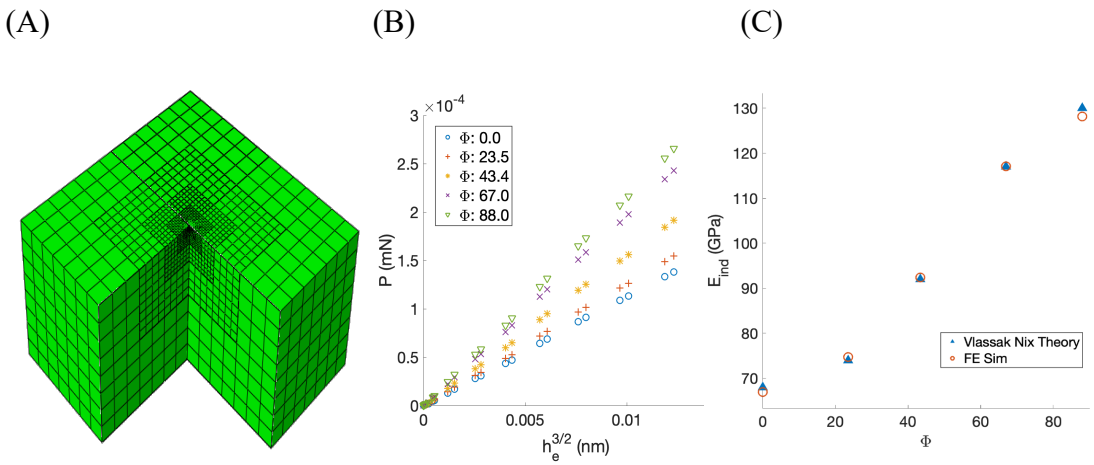

Figure 3.5. (A) Mesh used for Finite Element simulations. (B) Finite element simulated plots of P vs $h_e^{3/2}$ for zinc single crystals. (C) Comparison of Theoretical and FE simulated indentation moduli values reported for zinc single crystals.

For building the reduced-order model (Step 1 of the protocol), we need to identify the specific ranges of the intrinsic material properties of interest. For this study, the bounds of the ranges for the single crystal elastic constants were taken as 80 GPa $\leq C_{11} \leq$ 240 GPa, 40 GPa $\leq C_{12} \leq$ 120 GPa, 30 GPa $\leq C_{44} \leq$ 90 GPa, 70 GPa $\leq C_{33} \leq$ 210 GPa, and 40 GPa $\leq C_{13} \leq$ 90 GPa; these were chosen to encompass a large number of hcp metals of future interest to our research [6]. The transverse elastic isotropy of the hcp symmetry

implies that the elastic indentation response is dependent solely on the declination angle (Φ) between the indenter axis and c-axis of the hcp crystal. Therefore, one only needs to explore the orientation space defined by $0 \leq \Phi \leq \frac{\pi}{2}$ radians. Our goal will be to employ the sequential design strategy once again to efficiently explore the multi-dimensional parameter space identified above in establishing a reliable and robust reduced-order model for the FE indentation simulations over the entire parameter space of interest.

3.5.2 Model Building Process

As with the previous case study, the truncation parameters (Q, L) are important hyper-parameters in the model building process. Since, these are not known a priori, we need to build reduced-order models with different values of these hyper-parameters and make suitable selections. The basic strategy employed here as follows: (1) Reduced-order models with lower truncation levels are initially established, (2) the truncation level is increased systematically if the performance of the established reduced-order model is deemed inadequate, and (3) the model building process is stopped when either the accuracy of the reduced-order model is deemed adequate or when the improvements in the accuracy were deemed insignificant. The LOOCV errors obtained from this process for the different truncations levels are depicted in Figure 3.6. A set of 760 simulations were used as the initial set for all of these model-building exercises. This number was chosen to be slighter larger than the number of terms in the expansion of Eqn. 3.1) for the case (Q=2, L=4), which results in a total of 729 terms in the expansion. This initial set was identified using a Latin hypercube design (LHD) [57] across the 6 dimensional parameter space $\{C_{11}, C_{12}, C_{44}, C_{33}, C_{13}, \Phi\}$.

Following the initialization, additional simulations were chosen based on a screening of the highest uncertainty across a denser LHD of 2440 sets of inputs (total of 3200 design points including the initialization set). The LOOCV error for the various truncation levels appears to decrease for all cases as data is added with slight increase for the truncations (Q=3, L=4, 6) after 2200 data points, which given the small changes (less than 0.3 GPa) is attributed to noise. It is apparent from Figure 3.6 that the truncation level combination (Q=2, L=4) outperforms others throughout the model building process. The good accuracy of the reduced-order model built for this case study becomes apparent after about 2200 FE simulations, exhibiting a LOOCV error of 1.3 GPa as seen from Figure 3.6 and Figure 3.7.

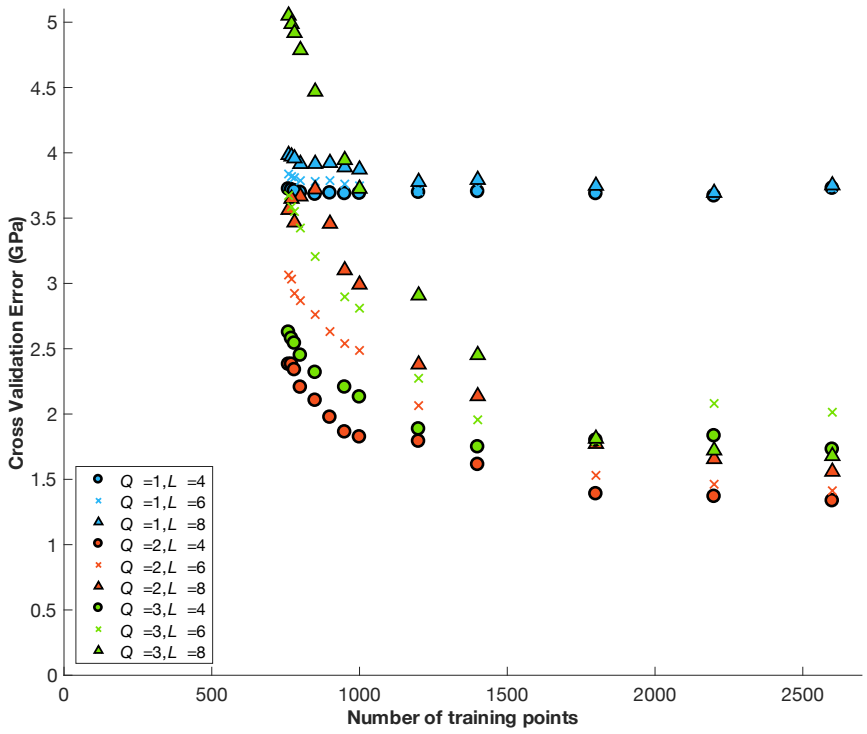

Figure 3.6. Cross validation error of the reduced-order models built in the first step of the two-step protocol for different truncation levels of Eqn. 3.1) for hcp crystals.

In order to generate a validation set, the selection process was continued to generate another set of 600 FE simulations. We argue that this approach is likely one of the best strategies

for building validation sets, as the elements of the validation set are selected based on the highest values of the prediction uncertainty. The prediction errors for the validation set of 600 FE simulations using the reduced-order model built with the training set of 2200 FE simulations are shown in Figure 3.8. This comparison yields a mean absolute error of 1.2 GPa.

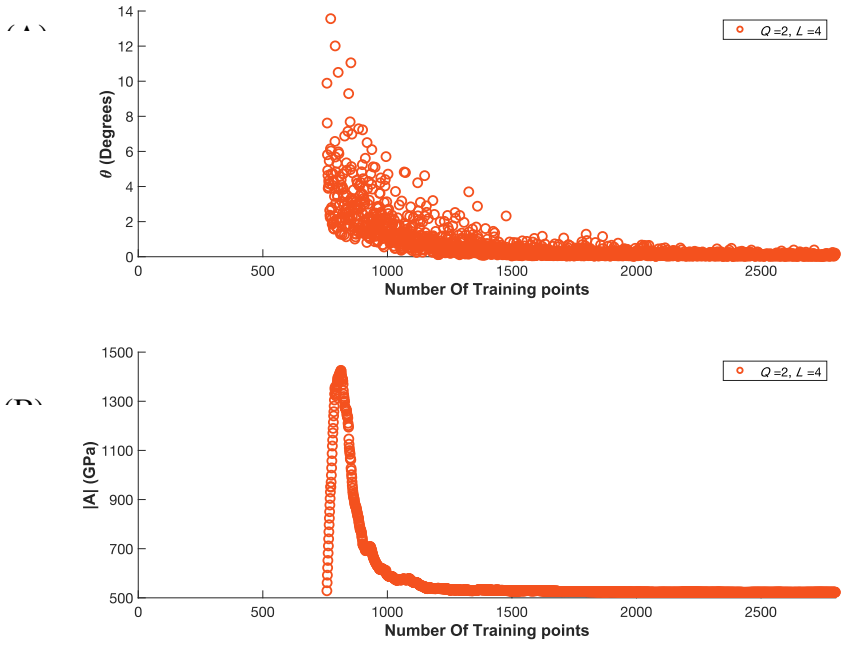

Figure 3.7. (A) Variation in the angular change in the vector of model coefficients between model update steps. (B) Variation in the magnitude of the vector of model coefficients during the model building process.

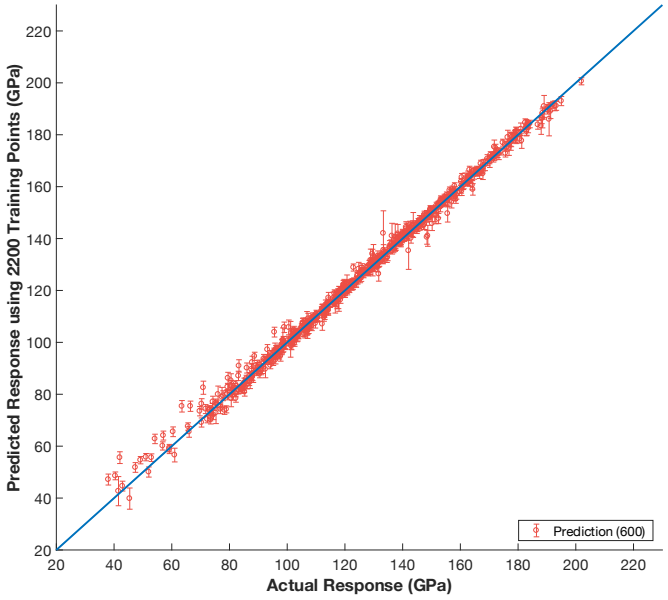

Figure 3.8. Predictions for the validation set of 600 FE simulations generated from sequential design process using reduced order model with truncations Q=2,L=4

It is important to recognize that the parameter space was purposefully chosen to be applicable to many hcp metals of future interest to our research [6]. Predictions are very good over the chosen parameter space as shown in Figure 3.8. Therefore, within the defined parameter space, future extraction efforts would no longer necessitate the generation of a new database. Furthermore, there is little value in performing additional simulations within the defined parameter space to attempt to significantly improve the reduced order model. The convergence of the associated model parameters in Figure 3.7 provides evidence that the reduced order model is unlikely change drastically with the introduction of new simulations.

It should be noted that the significantly larger training set needed for this case study compared to the previous case study can be attributed to the following reasons: (i) the present case study involved a six-dimensional input space whereas the previous one involved a five-dimensional input space, (ii) the range of values for each input in this case

study were selected to be significantly larger than the previous one, and (iii) the degree of elastic anisotropy and contrast captured in this case study is significantly larger compared to the previous case study. The degree of single crystal elastic anisotropy, can be quantified by the universal elastic anisotropic index, $\mathbb{A}$, [58,59] defined as

$$\mathbb{A} = 5\frac{G_v}{G_r} + \frac{K_v}{K_r} - 6 \tag{3.14}$$

where K and G are the bulk and shear moduli provided by Voigt and Reuss estimates (indicated by subscript v and r respectively) of a macroscopically homogenous polycrystalline material with uniform texture [60]. A maximum universal elastic anisotropic index of 7.2 was noted for the earlier cubic case study discussed in this paper, compared to 66.2 encountered in the current hcp case study. It is therefore quite reasonable that the number of training data points needed is significantly higher.

3.5.3 Extracting Intrinsic Material Parameters

The focus is now turned to the sampling of the posterior distribution of the elastic constants, $\boldsymbol{c} = \{C_{11}, C_{12}, C_{44}, C_{33}, C_{13}\}$, via MCMC. Similar to the previous case study, in order to sample from the posterior distribution of the intrinsic material parameters, the likelihood function in Eqn. (3.13) must be computed using the available experimental data and the reduced-order model established in Step (1) (corresponding to truncation levels Q=2, L=4 using a training set of 2200 FE simulation data points). The experimental data for this case study was obtained from a prior openly shared dataset [1]. This data set included indentation moduli for 50 different crystal orientations on a CP-Ti sample. Following the procedure described in Section 3.3.2, 50000 samples were drawn using the MCMC approach. The resulting posterior distributions are shown in Figure 3.9 for each of the five

intrinsic hcp elastic stiffness parameters. The maximum-a-posteriori (MAP) estimates, the mean values, and the standard deviations of the distribution are reported as a table in the same figure. The reported mean values for elastic constants were found to be $\{155, 89, 49, 174, 55\}$ GPa for $\{C_{11}, C_{12}, C_{44}, C_{33}, C_{13}\}$, respectively. Typical literature values reported are $\{162, 92, 47, 180, 69\}$ GPa [61]. With the exception of C_{13}, the extracted intrinsic stiffness parameters show good agreement with values reported in literature (mean values are within 5%). It is also interesting to note that the extracted distribution for C_{13} exhibits the highest relative uncertainty.

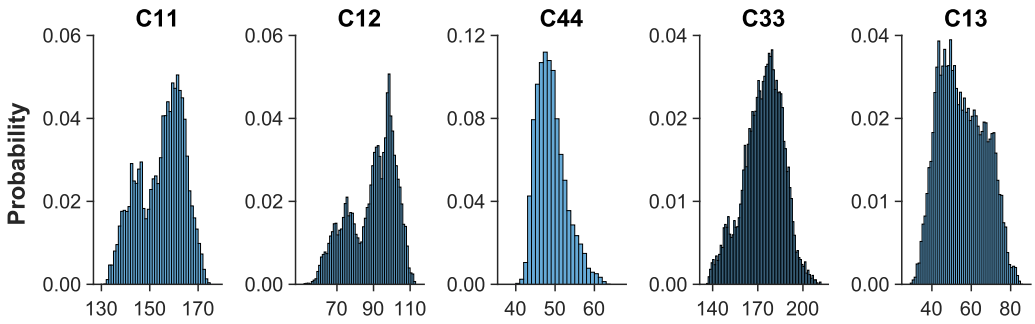

	C11	C12	C44	C33	C13
MAP (GPa)	161.5	98.5	47.5	179.5	49.5
Mean (GPa)	154.9	89.3	49.0	173.7	55.3
STDEV	9.3	12.6	3.8	13.2	11.5

Figure 3.9. MCMC sampling of the posterior distribution for the intrinsic single crystal elastic constants of CP-Ti.

This indicates the relative low sensitivity of the indentation modulus to changes in C_{13}, when compared to the other elastic stiffness constants. As noted in the previous case study, it should be possible to extend the framework presented here to focus exclusively on improving the estimation of C_{13} [42]. However, such an effort could only be justified after the uncertainty in the literature reported values is rigorously quantified. The variance in the

predictions of the surrogate model at selected orientations is compared with the experimental data in Figure 3.10.

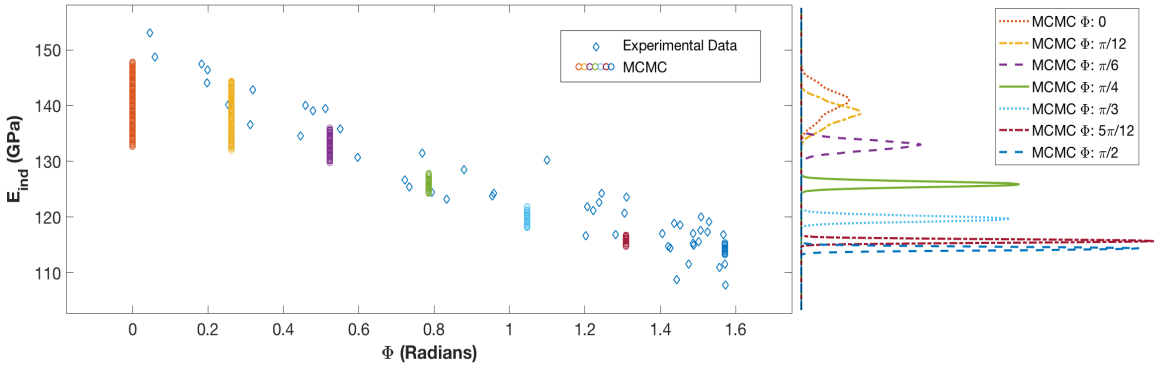

Figure 3.10. Left: Reduced-order model evaluations of the Markov Chain (MCMC) at selected points across the orientation space compared to available experimental data. Right: The resulting distributions of the evaluations using the reduced order model.

Evaluations of the reduced-order model at various orientations using samples from the posterior distributions of the elastic constants provides the possible mean indentation moduli for the observed experimental indentation moduli, as described in Section 3.3.2. Since the reduced-order model coupled with a sampled set of elastic moduli from the posterior distribution of elastic constants provides the respective mean indentation modulus as a function of orientation, the predictions should be more tightly packed in regions which there are more observations, reflecting a higher certainty of the mean. The prediction uncertainty from MCMC is in fact shown to be highest at low declination angles, while uncertainty is lowest at high declination angles where relatively much more data is available. Furthermore, this observation suggests that there is much more value in conducting additional tests at the lower declination angles, specifically in the range of 0-0.2 radians, compared to conducting them at the higher declination angles. This could be highly valuable input to the experimentalists for their future studies.

3.6 Conclusions

A statistical framework has been presented for the robust extraction of the intrinsic material parameters from available experimental observations from spherical indentation stress-strain protocols. The two-step Bayesian inference framework enables the specification of uncertainty in the measurement data, which is then transferred to the uncertainty in the values of the extracted intrinsic material properties. Most importantly, the new framework presented in this paper demonstrates potential for significantly speeding up the materials characterization effort by focusing on experiments that are likely to deliver the maximum value in establishing the desired properties. This is accomplished by employing a numerical model of the experiment itself (here accomplished using a finite element model). Although the numerical model can be very expensive, it is only needed for a one-time effort is establishing a reduced-order model (Step (1) of the proposed two-step protocol). Once the reduced-order model is established, the calibration of the available experimental data to the theory (Step (2) of the proposed two-step protocol) can be accomplished with minimal computational resources. The versatility and the robustness of the proposed new framework is demonstrated with two case studies: (i) extraction of three elastic constants for Fe-3%-Si, and (ii) extraction of the five elastic constants for CP-Ti. In both case studies, the ranges of intrinsic material parameters considered covers a significant number of polycrystalline hcp and cubic metals. This makes both models highly applicable to new case studies within the material classes. For material classes outside of the classes explored here, the main challenge is indeed Step (1) of the protocol, requiring the establishment of a high fidelity reduced-order model from suitable FE simulations, while Step (2) remains the same. In the event the extracted parameters in Step (2) fall outside of the extents of the

databases used to construct the reduced-order model, additional simulations considering the new bounds would become necessary. Finally, the use of a Bayesian framework opens new avenues for the development of autonomous (fully guided by the computer) scientific explorations. It is anticipated that the framework is extensible to a large number of other applications in multiscale materials modeling (e.g., extraction of the values of slip resistances from indentation measurements, extraction of the values of parameters in phase-field models based on available microstructure datasets).

Acknowledgements

The authors acknowledge funding from AFOSR award FA9550-18-1-0330 (Program Manager: J. Tiley). AC acknowledges funding from the National Science Foundation Grant 1258425.

CHAPTER 4. SEQUENTIAL DESIGN OF EXPERIMENTS FOR THE EXTRACTION OF INTRINSIC MATERIAL PROPERTIES VIA SPHERICAL INDENTATION MEASUREMENTS

The following work was accepted for publication in the Journal, JOM, in May 2019 under the title "Bayesian Sequential Design of Experiments for the Extraction of Single Crystal Material Properties from Spherical Indentation Measurements on Polycrystalline Samples" [47]. Order of authorship is Andrew R. Castillo, Roshan V. Joseph and Surya R. Kalidindi. AC was responsible for data analysis and simulations, RJ and SK provided guidance. All contributed to preparation of the manuscript

4.1 Abstract

This paper explores a formal strategy for the extraction of single crystal elastic constants of cubic polycrystalline metals based on the optimal design of spherical indentation experiments. Recent work has formulated the extraction of elastic constants using a two-step protocol. The first step established a surrogate model to capture the dependence of the indentation elastic modulus on the grain (i.e., crystal lattice) orientation and values of single crystal elastic constants. The second step involved the use of Markov Chain Monte Carlo (MCMC) to establish distributions on the elastic constants consistent with experimentally measured indentation moduli in grains of different orientations. The present study refines the second step in order to sequentially identify specific grains that should be indented to provide the most utility in improving the estimated distributions on

the elastic constants. The proposed workflow is demonstrated for the extraction of elastic constants for an as-cast cubic polycrystalline Fe-3%-Si sample.

4.2 Introduction

The lack of robust strategies for extracting reliable values of the intrinsic material parameters from related experimental measurements is currently one of the central bottlenecks in the advancement of multiscale materials modeling capabilities. As a specific example of interest to this paper, modern instrumented indentation systems have been remarkably successful in providing reliable measurements of the local load-displacement responses in a sample with a submicron-scale spatial resolution [62-64]. Recently developed spherical indentation protocols have demonstrated the consistent extraction of crystal-level indentation stress-strain responses from sub-granular load-displacement indentation measurements on polycrystalline samples [13-15,65,66]. More specifically, because of their high spatial resolution, these recent protocols are able to reliably extract grain-level indentation properties such as indentation modulus and indentation yield strength, which exhibit the expected dependence on the initial crystal lattice orientation in the indented material. With all these recent advances, the central challenge remains the reliable extraction of the values of the intrinsic materials properties (e.g., single crystal elastic stiffness parameters such as C_{11}, C_{12}, and C_{44} or the critical resolved shear strength that do not depend on the grain orientation) from the grain orientation-dependent properties measured in the indentation tests. This fundamentally requires an inverse solution that calibrates the values of the intrinsic material properties of interest by matching the forward theoretical solutions to the measurements obtained on an ensemble of grain orientations in a given polycrystalline sample [5,7,10,67].

One of the central bottlenecks in addressing the critical gap identified above comes from the fact that the forward model connecting the intrinsic material properties of the material to their corresponding indentation stress-strain responses requires the execution of a computationally expensive finite element (FE) model of the indentation test [8-11]. Since the solution of the inverse problem formulated above requires many forward solutions, there is a critical need for a clever strategy. In recent work [7,68], one such strategy involving a two-step protocol has been formalized: (1) Establish a surrogate model for the computationally intensive FE simulations; (2) Use inverse methodologies to calibrate intrinsic material parameters given available experimental data. It should be noted that the establishment of a reduced-order model (i.e., step (1)) requires a one-time high computational cost for a given material class (e.g., cubic crystals, hexagonal crystals). For example, it was shown that one can successfully build a high accuracy reduced-order model for capturing the relationship between the indentation elastic modulus and the grain orientation for a broad range of cubic materials [7]. Similarly, it was also shown that it is possible to build a reduced-order model to capture the dependence of indentation yield strength on the grain orientation for the entire class of single-phase bcc metals deformed by slip [10]. Once the reduced-order model is developed and validated, the main remaining challenge come from the efficient execution of the experiments (i.e., step (2)).

The experimental component of step (2) of the protocol involves conducting indentation measurements in grains of different orientations. A typical strategy for this task has been to perform as many indentation experiments in as many grains as possible [8,12]. The only guidance one typically gets is to select grains orientations that ensure a roughly uniform coverage of the fundamental zone of the relevant orientation space (defined based on the

crystal symmetry) [1,13]. Here is where an optimal design of experiments strategy might prove to be very beneficial. As a specific example, a properly designed strategy can inform the experimentalist on the following questions: (i) Amongst the available grain orientations on the sample, which orientation is likely to offer the most valuable information in improving the estimates of the intrinsic material properties of interest? (ii) When should one stop doing more tests? The answers to these questions have the potential to improve the reliability of the extracted values of the intrinsic material parameters of interest, while minimizing the number of experiments conducted.

A formal design of experiments strategy has not yet been explored in literature for the estimation of the grain-scale intrinsic material properties using the spherical indentation test protocols. Generally speaking, the strategies for the design of experiments can be broadly classified as static designs and sequential designs. Static designs focus upon finding a design prior to performing any experiments [69]. We note these approaches typically do not provide guidance for where additional experiments should be performed, or even if additional experiments should be performed. Sequential designs adjust depending on the values previously observed. Because of their high tailorability, sequential designs are well suited for studies of complex nonlinear problems using sophisticated and expensive tools such as the ones considered in this work [42,70].

The central challenge in sequential design arises from the fact that the value of an experiment is difficult to quantify prior to actually performing the experiment and attempting to extract the desired information (here these are the intrinsic material parameters). Therefore, the goal of this paper is to develop a dynamic workflow which provides guidance in the selection of the grain orientations for indentation measurements

by leveraging sequential design strategies. In this workflow, estimates of intrinsic material parameters are continually updated as new experimental data becomes available from grain orientations chosen by a utility function. The utility function is designed to effectively quantify the expected information of an experiment that is yet to be performed using Bayesian strategies. These strategies are reliant on the rigorous determination of the distributions associated with the variables of interest (i.e., intrinsic material parameters). In this work, the determination of the distribution of unknown model parameters has been accomplished using Markov Chain Monte Carlo (MCMC). The calibration of unknown model parameters using MCMC is already well established in many other applications [42,71,72].

The workflow explored in this study will first establish the distributions associated with the estimations of the intrinsic material parameters, then use the established distributions as an input to the evaluation of Bayesian-based information metrics. As a first application of this workflow, this study focuses on the extraction of the single elastic stiffness constants from a collection of experimental indents conducted on grains of different lattice orientations in a given polycrystalline sample.

4.3 Extraction of Intrinsic Material Parameters Via Spherical Indentation

4.3.1 Experimental Protocols

Modern instrumented indenter machines can measure the local mechanical response of the material volume underneath the indenter tip in the form of a load–displacement curve with high accuracy and resolution. The linear elastic response due to the contact of two quadratic surfaces is described by Hertz theory [17] as

$$P = \frac{4}{3} E_{eff} R_{eff}^{\frac{1}{2}} h_e^{\frac{3}{2}} \qquad (4.1)$$

$$\frac{1}{E_{eff}} = \frac{1 - v_s^2}{E_s} + \frac{1 - v_i^2}{E_i} \qquad (4.2)$$

$$R_{eff} = \frac{1}{R_s} + \frac{1}{R_i} \qquad (4.3)$$

where P is the indenter load, h_e is the elastic indentation displacement, and R, E, v, denote the radius, Young's modulus and Poisson's ratio of the indenter and sample denoted by subscripts i, s respectively. These equations are the basis for defining material properties measured in indentation tests, and their correlation to the intrinsic material parameters of interest to multiscale modeling efforts. For example, in the equations presented above, E_{eff} is a material property measured in indentation, while E_s is the intrinsic property of an isotropic material that is employed in modeling the response of the material to arbitrary loading conditions.

As noted earlier, a major advance in instrumented indentation has been their impressive resolutions in measuring very small loads and displacements, making it possible to measure local material responses from exceedingly small volumes of material. For example, one can conduct indentation measurements using spherical tips of radius ~1 μm, where the material volume exposed to the indentation plastic strains can be limited to a volume ~(100 nm)^3. These techniques offer unprecedented opportunities for studying the mechanical response in heterogeneous materials at multiple resolutions (i.e., length scales) ranging

from the nanoscale to the macroscale. As a specific example, we consider here the potential of spherical indentation for measuring the local elastic response of single crystals (i.e., grains) in a polycrystalline sample. In these experiments, the indenter tip size is chosen such that the effective indentation zone is significantly smaller than that of the grain being indented. Consequently, the E_{eff} computed using Hertz's theory (Eqs.) would depend only on the lattice orientation of the indented grain, $\boldsymbol{g} = \{\phi_1, \Phi, \phi_2\}$, and the intrinsic single crystal elastic stiffness parameters for the material; for cubic crystals, these are usually denoted as $\mathrm{C}_{11}, \mathrm{C}_{12}$, and C_{44}.

Estimation of Intrinsic Material Parameters using Markov Chain Monte Carlo

The indentation property E_{eff} (simply referred to as indentation modulus E henceforth) can be extracted from FE simulations for any specified lattice orientation, $\boldsymbol{g}$, and elastic stiffness constants, $\boldsymbol{c} = \{\mathrm{C}_{11}, \mathrm{C}_{12}, \mathrm{C}_{44}\}$. Therefore, the goal is to calibrate a set of elastic stiffness constants $\boldsymbol{c}$, by matching the simulated indentation modulus, E_{sim}, to the experimentally observed indentation modulus, E, for a collection of differently oriented grains. The experimental data is denoted by $\{\boldsymbol{E}_{exp}, \boldsymbol{G}_{exp}\}$, where $\boldsymbol{E}_{exp}$ are the set of experimentally measured indentation moduli corresponding to the set of lattice orientations $\boldsymbol{G}_{exp}$. The search across the intrinsic material parameter space using simulations is difficult due to the large product space of the possible values of the elastic constants and the range of grain orientations where the indentation moduli were measured. As already mentioned, an efficient strategy for addressing this inverse problem requires the establishment of a low-computational cost surrogate model for predicting the dependence of the indentation properties for prescribed values of the intrinsic material properties and grain orientations.

Since the only available approach to accomplishing this task reliably is to use the computationally expensive FE modeling toolsets [1,7,8,12], this means that one needs to train the surrogate model to the results of the FE simulations of the indentation tests. Furthermore, we wish to rigorously establish the associated uncertainty of the intrinsic material parameter estimates. Establishing the distributions on the intrinsic material parameters (i.e., uncertainty) typically requires computationally intensive sampling techniques, which are often only feasible through the use of a suitable reduced-order model.

Let $\hat{E}(\boldsymbol{c}, \boldsymbol{g})$ denote the reduced-order model relating the indentation modulus to a set of elastic constants and a lattice orientation, where the hat denotes that it is an approximation of the FE simulated $E(\boldsymbol{c}, \boldsymbol{g})$. In order to establish this function, a database of simulations covering the very large input parameter space is necessary. The database is described by $\{\boldsymbol{E}_{sim}, \boldsymbol{C}_{sim}, \boldsymbol{G}_{sim}\}$, where $\boldsymbol{E}_{sim}$ denote the set of FE simulated indentation moduli corresponding to grain (lattice) orientations $\boldsymbol{G}_{sim}$ and the single crystal elastic stiffness constants $\boldsymbol{C}_{sim}$. A reduced-order model with high accuracy has previously been established to predict the single crystal indentation modulus for cubic polycrystalline metals [7,73]. This function is expressed as

$$\hat{E}(\boldsymbol{c}, \boldsymbol{g}) \approx \sum_{l=0}^{L} \sum_{m=1}^{M(l)} \sum_{\boldsymbol{q}}^{\boldsymbol{Q}} A_l^{m\boldsymbol{q}} K_l^m(\boldsymbol{g}) \tilde{P}^{\boldsymbol{q}}(\bar{\boldsymbol{c}}) \tag{4.4}$$

$$\bar{c}_j = \frac{2c_j - c_j^{min} - c_j^{max}}{c_j^{max} - c_j^{min}} \tag{4.5}$$

where $\mathrm{K}_{\mathrm{l}}^{\mathrm{m}}(\boldsymbol{g})$ denote the symmetrized Surface Spherical Harmonics basis (enumerated by indices l and m) over the relevant orientation space of interest [73], and $\widetilde{\mathrm{P}}^{\mathbf{q}}(\bar{\mathbf{c}})$ denote a multivariate Legendre polynomial product basis. In other words, one can express $\widetilde{\mathrm{P}}^{\mathbf{q}}(\bar{\mathbf{c}}) = P^{q_1}(\bar{c}_{11})P^{q_2}(\bar{c}_{12})P^{q_3}(\bar{c}_{44})$, where $\boldsymbol{q} = (q_1, q_2, q_3)$ forms a multi-index array, each element of which is a nonnegative integer allowed to vary from 0 to the selected maximum degree, Q, i.e., $q_j \in [0, Q]$. For the proper application of the Legendre Polynomial basis, each of the elastic constants are rescaled over the range [74] as shown in Eqn. (4.5), where c_j^{max} and c_j^{min} are the maximum and minimum values of the j-th elastic constant. Integers Q and L denote the truncation levels adopted in the formulation of Eqn. (4.4). We note that the central challenge associated with the reduced-order model comes from establishing the model coefficients, A_l^{mq}, using the database of finite element simulations $\{\boldsymbol{E}_{sim}, \boldsymbol{C}_{sim}, \boldsymbol{G}_{sim}\}$, and determining appropriate truncation levels (Q, L). We note specifically that the model coefficients, A_l^{mq} have been determined in prior work using Bayesian Linear Regression [44]. Since the reduced-order model described by Eqn. (4.4) has already been built successfully in prior work (i.e., step (1) of the protocol described above) [44], attention in this work is drawn to step (2) of the protocol.

The extraction of intrinsic material parameters as described in step (2) will be approached in this work with an optimal Bayesian design of experiments strategy. As previously mentioned, this strategy requires a rigorous quantification of the distributions of the intrinsic material properties to be estimated. In other words, it is necessary to quantify the variations in the indentation measurements and effectively propagate them to the uncertainty in the estimates of the intrinsic material parameters through the inverse solution strategy (i.e., matching experiments to the FE simulations by varying the intrinsic material

parameters as the inputs). This is accomplished using a stochastic framework. Formally, the goal is to obtain the posterior distribution on the intrinsic material parameters, $p(\boldsymbol{c}|\boldsymbol{E}_{exp}, \boldsymbol{G}_{exp})$, which provides the probability density of the intrinsic material parameters, $\boldsymbol{c}$, given the experimental data, $\{\boldsymbol{E}_{exp}, \boldsymbol{G}_{exp}\}$. Using Bayes theorem, this is expressed as

$$p(\boldsymbol{c}|\boldsymbol{E}_{exp}, \boldsymbol{G}_{exp}) = \frac{p(\boldsymbol{E}_{exp}|\boldsymbol{c}, \boldsymbol{G}_{exp})p(\boldsymbol{c})}{\int_{\boldsymbol{c}} p(\boldsymbol{E}_{exp}|\boldsymbol{c}, \boldsymbol{G}_{exp})p(\boldsymbol{c})d\boldsymbol{c}} \qquad (4.6)$$

where $p(\boldsymbol{E}_{exp}|\boldsymbol{c}, \boldsymbol{G}_{exp})$ and $p(\boldsymbol{c})$ denote the likelihood function and the prior belief, respectively. The denominator on the right-hand side of Eqn. (4.6) reflects the evidence, whose computation is typically intractable. One way to address this challenge is to sample from the posterior using a Markov Chain Monte Carlo (MCMC) method. MCMC allows the sampling from the posterior distribution, $p(\boldsymbol{c}|\boldsymbol{E}_{exp}, \boldsymbol{G}_{exp})$, once the likelihood and prior are specified [34,36].

Let

$$E = E_{sim}(\boldsymbol{c}, \boldsymbol{g}) + \epsilon \qquad (4.7)$$

where $E_{sim}(\boldsymbol{c}, \boldsymbol{g})$ is a prediction of the indentation modulus from the FE simulation and ϵ is the measurement error in the real experiment. Assuming the measurement errors are independent and normally distributed with zero mean and constant variance σ^2 (i.e., $\epsilon \sim \mathcal{N}(0, \sigma^2)$), the likelihood can be expressed as

$$p\left(\boldsymbol{E}_{exp}\middle|\boldsymbol{c},\boldsymbol{G}_{exp}\right)=\prod_{i=1}^{n}\frac{1}{\sqrt{2\pi}\sigma}exp\left\{-\left(E_i-E_{sim}(\boldsymbol{c},\boldsymbol{g}_i)\right)^2/(2\sigma^2)\right\} \quad (4.8)$$

where n is the number of indentation experiments. MCMCs usually require as many as $N = 50{,}000$ samples to attain convergence. This means, the likelihood function needs to be evaluated N times, which is computationally infeasible because each evaluation of the likelihood requires n evaluations of the FE indentation models. This is where the reduced-order model obtained previously [44] (step (1) of the protocol) comes in handy. Using this high fidelity reduced-order model, $\hat{E}(\boldsymbol{c},\boldsymbol{g})$, the likelihood function is expressed as

$$p\left(\boldsymbol{E}_{exp}\middle|\boldsymbol{c},\boldsymbol{G}_{exp}\right)=\frac{1}{\left(\sqrt{2\pi}\sigma\right)^n}exp\left\{-\sum_{i=1}^{n}\left(E_i-\hat{E}(\boldsymbol{c},\boldsymbol{g}_i)\right)^2/(2\sigma^2)\right\} \quad (4.9)$$

Note that the uncertainty in the reduced-order model is neglected in writing Eqn. (4.9). Assuming a uniform prior for $p(\boldsymbol{c})$ along with the likelihood function in Eqn. (4.9) allows for the application of MCMC methods for sampling the posterior distribution on the intrinsic material parameters. In this work, this is performed using the Single Component Metropolis Hastings (SCMH) approach which considers component wise transitions [35].

4.4 Bayesian Sequential Design Of Experiments

The estimation of the single crystal elastic constants involves the matching of the simulated and the measured indentation moduli in grains of different orientations selected in a polycrystalline sample. The design of experiments task here solely considers what orientations ought to be picked for the indentation measurements. The available

orientations are provided by an orientation map obtained on the sample using electron back-scattered diffraction (EBSD) techniques [51]. In the following, we denote the set of grain orientations available for indentation measurements in the given sample (identified in the EBSD map) as $\boldsymbol{G}_{map}$. We note that the goal of design of the experiments is to identify the set of grain orientations $\boldsymbol{G}_{exp}$, $\boldsymbol{G}_{exp} \subseteq \boldsymbol{G}_{map}$, which are expected to provide the highest amount of information regarding the distributions on the intrinsic material properties of interest. Typically, $\boldsymbol{G}_{exp}$, is determined to obtain a uniform sampling of $\boldsymbol{G}_{map}$. As previously noted, this simple strategy is likely to be suboptimal, since the indentation measurements in the different grains are expected to exhibit different levels of sensitivity to the intrinsic properties of interest. Furthermore, there is little guidance to determine when one should stop making new measurements. This is because beyond a certain number of measurements (on grains of different orientations), new measurements are unlikely to add significant value to the stated goal of estimating the intrinsic materials properties of interest. Consequently, the simple strategies used currently often lead to oversampling. This work explores the benefits of approaching the problem through an optimal sequential design of experiments. This sequential workflow tracks rigorously the improvements made to the distributions on the intrinsic material parameters of interest, as new indentation measurements are added. In this strategy, one can objectively decide when to stop making further measurements because the protocols will naturally reveal when there are no further improvements to the distributions with the addition of new measurements. The details of the sequential design of experiments workflow implemented for the present study are summarized in Figure 4.1 The main task in this workflow is the optimal selection of the next orientation, $\boldsymbol{g} \in \boldsymbol{G}_{map}$, for the indentation measurement such that we can obtain the

largest reduction in the variance for the distributions on the intrinsic material properties of interest.

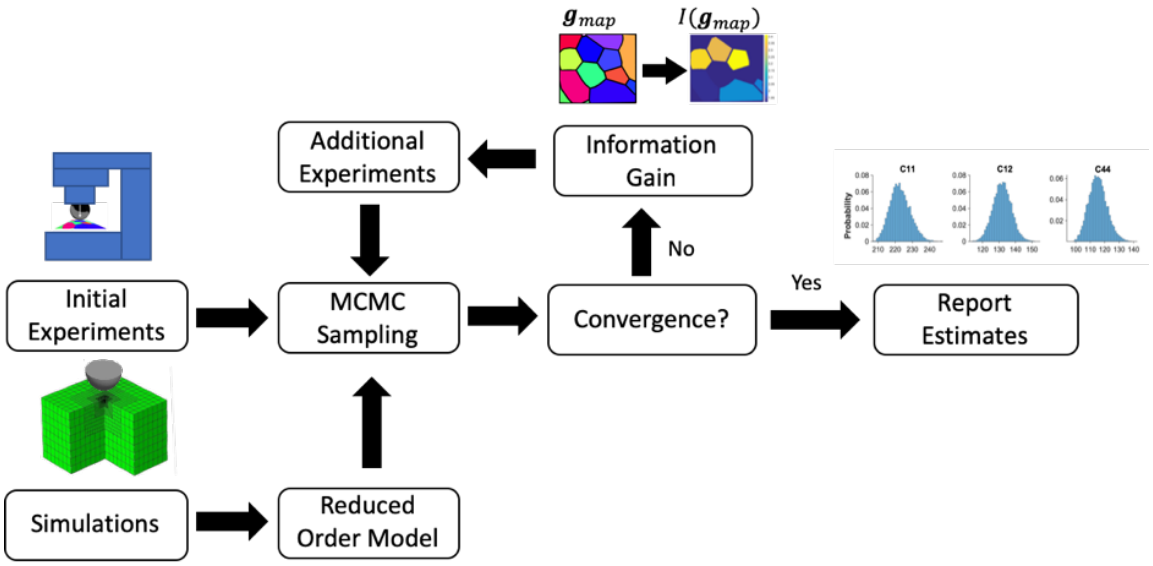

Figure 4.1. An overview of the proposed workflow for the estimation of the intrinsic single crystal elastic properties of the material. Utilizing a reduced-order model calibrated to a physics-based finite element model of the indentation experiment, the workflow evaluates the potential of each grain orientation in the sample for lowering the variances of the distributions on the intrinsic materials properties of interest. After performing the measurement and updating the distributions, the cycle is repeated. The experiments are stopped when the improvement in the distributions is deemed insignificant.

Before the start of the experiments, the pre-existing knowledge about the intrinsic material parameters $\boldsymbol{c}$ is encapsulated in the prior distribution, $p(\boldsymbol{c})$. Given any available experimental data $\{\boldsymbol{E}_{exp}, \boldsymbol{G}_{exp}\}$, the prior knowledge can be updated to obtain the posterior distribution $p(\boldsymbol{c}|\boldsymbol{E}_{exp}, \boldsymbol{G}_{exp})$ using Eqn. (4.5). Therefore, the value of the experimental data can be related to the difference between $p(\boldsymbol{c}|\boldsymbol{E}_{exp}, \boldsymbol{G}_{exp})$ and $p(\boldsymbol{c})$. One approach to measuring the difference between these two distributions is to use the Kullback-Liebler (KL) divergence expressed as [38]

$$KL(p(\boldsymbol{c}|\boldsymbol{E}_{exp},\boldsymbol{G}_{exp})||p(\boldsymbol{c})) = \int \log\frac{p(\boldsymbol{c}|\boldsymbol{E}_{exp},\boldsymbol{G}_{exp})}{p(\boldsymbol{c})} p(\boldsymbol{c}|\boldsymbol{E}_{exp},\boldsymbol{G}_{exp})d\boldsymbol{c} \tag{4.10}$$

However, since $\boldsymbol{E}_{exp}$ is unknown before the experiment, the KL distance needs to be averaged over the distribution of the possible values of $\boldsymbol{E}_{exp}$ in order to obtain a computable measure. Thus, the objective is to find $\boldsymbol{G}_{exp}$ to maximize the expected KL divergence expressed as

$$I(\boldsymbol{G}_{exp}) = \int KL(p(\boldsymbol{c}|\boldsymbol{E}_{exp},\boldsymbol{G}_{exp})||p(\boldsymbol{c}))p(\boldsymbol{E}_{exp}|\,\boldsymbol{G}_{exp})d\boldsymbol{E}_{exp}$$

$$= \iint \log\frac{p(\boldsymbol{c}|\boldsymbol{E}_{exp},\boldsymbol{G}_{exp})}{p(\boldsymbol{c})} p(\boldsymbol{c},\boldsymbol{E}_{exp}|\boldsymbol{G}_{exp})d\boldsymbol{c}d\boldsymbol{E}_{exp} \tag{4.11}$$

where $I(\boldsymbol{G}_{exp})$ can be viewed as the expected Shannon information gain [38,39] (or simply referred as information gain) due to the experiments. This criterion can be used for finding the Bayesian optimal design of experiment [40,41].

The approach described above tries to choose a set of n experiments simultaneously to maximize the information gain. An even better approach is to choose them sequentially by making use of the data obtained from the previous experiments in an adaptive manner. Such a sequential approach allows us to address the central questions raised as the main motivation for this work. That is, we can systematically select additional experiments with respect to the expected information gain considering our accumulated knowledge, and identify a stopping point for the experiments when the information gain is no longer significant.

Suppose k experiments are already done and the properties were measured. The aim is to choose the $(k+1)^{\text{th}}$ experiment, i.e., find the next grain orientation to perform the indentation measurement. As discussed in the previous section, we will use MCMC to obtain the posterior distribution of $\boldsymbol{c}$ given the data. Since the errors ϵ are independent, the posterior distribution of $\boldsymbol{c}$ obtained after k experiments can be viewed as the prior distribution of $\boldsymbol{c}$ for the $(k+1)^{\text{th}}$ experiment. For notational convenience, we will denote it by $p(\boldsymbol{c})$, that is, its dependence on the data from the k experiments is suppressed. Then, the objective is to find $\boldsymbol{g}$ to maximize the information gain for the $(k+1)^{\text{th}}$ experiment, expressed as

$$I(\boldsymbol{g}) = \iint \log \frac{p(\boldsymbol{c}|E,\boldsymbol{g})}{p(\boldsymbol{c})} p(\boldsymbol{c},E|\boldsymbol{g}) d\boldsymbol{c}dE$$

$$= \iint \log \frac{p(E|\boldsymbol{c},\boldsymbol{g})}{p(E|\boldsymbol{g})} p(E|\boldsymbol{c},\boldsymbol{g}) p(\boldsymbol{c}) d\boldsymbol{c}dE \qquad (4.12)$$

This can be approximated using the MCMC samples [75] by

$$\hat{I}(\boldsymbol{g}) \approx \int \frac{1}{N} \sum_{i=1}^{N} \log \frac{p(E|\boldsymbol{c}_i,\boldsymbol{g})}{p(E|\boldsymbol{g})} \, p(E|\boldsymbol{c}_i,\boldsymbol{g}) dE \qquad (4.13)$$

where the evidence term in the denominator can be further approximated by

$$p(E|\boldsymbol{g}) \approx \frac{1}{N}\sum_{j=1}^{N} p\left(E\middle|\boldsymbol{c}_j, \boldsymbol{g}\right) \tag{4.14}$$

The one-dimensional integral with respect to E in Eqn. (4.14) can be performed using numerical approaches such as Gaussian quadrature or Newton Cotes [76]. The search for the optimal grain is performed over a candidate set of grain orientations, $\boldsymbol{G}_{map}$. Thus, the Bayesian sequential design algorithm for the grain orientation $\boldsymbol{g}^*$ where the next indentation ought to be performed can be expressed as

$$\boldsymbol{g}^* = \underset{\boldsymbol{g}\in\boldsymbol{G}_{map}}{\operatorname{argmax}}\, \hat{I}(\boldsymbol{g}) \tag{4.15}$$

4.5 Case Study: Extraction of Elastic Constants from a Cubic Polycrystalline Sample

In order to demonstrate the validity of the overall strategy proposed in this work, the focus is now turned to a case study involving the guided extraction of the elastic constants $\{C_{11}, C_{12}, C_{44}\}$ from a polycrystalline sample of the bcc metal Fe-3%-Si. For this problem, a reduced-order model for the indentation modulus was already trained on FE simulations in prior work [7]. The model was expressed using generalized spherical harmonics as a Fourier basis, and the coefficients were calibrated using Bayesian linear regression [44]. The model showed high accuracy exhibiting a prediction average error of 2.1% over a validation set of 1986 simulations from a large product space of grain orientations and

cubic elastic stiffness parameters. The model coefficients were established using a training set of 300 simulations. Given the high predictive fidelity of the model, consideration of the uncertainty due to the reduced order model is omitted. The indentation mean and variance for the grains within the EBSD map depicted schematically in Figure 4.1 have been previously reported [28]. In the present case, due to the coarse-grained sample in question, $\boldsymbol{G}_{map}$ consisted of 11 orientations [28]. In order to explore the proposed workflow in Figure 4.1, the experiments are treated as unknown until identified by their determined utility. An initial likelihood function is necessary to begin the process. The initial likelihood function is built using the mean and variance of indentation modulus measured at a single orientation. The initial orientation is chosen such that the (001) crystallographic plane is as close to the sample normal axis as possible. This is due to the predictions from the reduced-order model being discernably sensitive to C_{11} (this is the dominant elastic stiffness parameter for cubic crystals) near this orientation [77]. Using this likelihood function, an initial posterior distribution is attained using MCMC.

Following the initialization, the initial posterior distribution of elastic constants is used to compute the information gain as described in Section (3), and the sequential design process begins. After each experiment is performed, the posterior distribution is sampled using MCMC. For each posterior distribution 50000 samples were drawn using MCMC. The initial 5000 were discarded in order to account for a "burn in" period. The selection of the next experiment is determined based on the maximum expected information gain across the grains in $\boldsymbol{G}_{map}$ using Eqn. (4.15). A problematic characteristic of the Shannon information metric is the potential computational cost. The computation cost associated with the information metric is O(N^2) where N is the length of the Markov chain. To

alleviate this computation only grains not yet selected in $\boldsymbol{G}_{map}$ were considered as selection candidates. Selection of additional experiments is continued until the posterior mean and standard deviation of the parameters exhibit convergence (i.e., only minimal changes with data added from new experiments). To serve as a comparison, random selection of experiments without replacement were also performed several times while utilizing the same initialization. The convergence rate using the information gain as a selection criteria was compared to cases using random selection in Figure 4.2. Using information gain as the design criteria, the mean of the sampled distribution of elastic constants was found to converge only after three experiments are performed. Additionally, using the information gain design criteria, the standard deviation also appears to converge after three experiments.

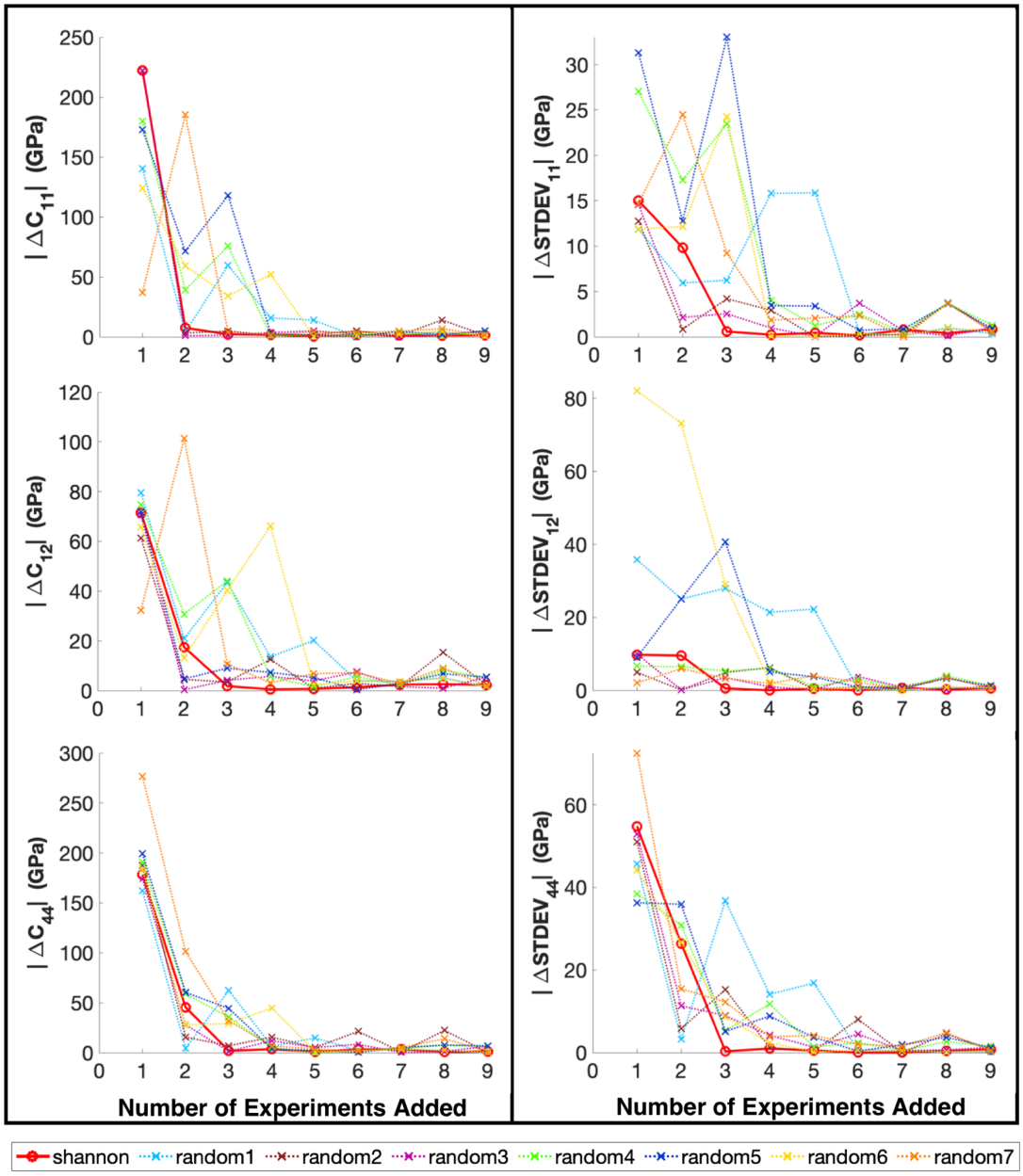

Figure 4.2. Comparison of parameter convergence rates for the sequential selection of experiments based on information gain criteria (shannon) and random selection. Left: Convergence rate for sampled mean {C11, C12, C44} of the MCMC chain. Right: Convergence rate for sampled standard deviation of {C11, C12, C44}. The initialization for all runs is a single orientation chosen such that the [100] crystal direction is close to the sample normal.

Likewise, all the distributions for each selection process appear to converge fairly quickly thereafter. It is not surprising that many of the poorly performing random runs initially selected orientations that were relatively close to each other. Furthermore runs in which distributions converged the fastest sampled close to the bounds of the orientation space first. This simply reflects the fact that the differing regions of the orientation space have discernably varying sensitivity to the individual intrinsic material parameters. Despite the adequate performance of a couple random runs, the results support the notion that the objective selection of experiments based on information gain indeed expedites the extraction of the intrinsic material parameters. Furthermore, the associated uncertainties of the extracted parameters (using information gain) after three experiments are hypothesized to be predominantly due to the uncertainty of the experimental measurements, rather than from under sampling the parameter space. This is evidenced by negligible changes in the standard deviation of the elastic constants after three experiments are performed while using the information gain criteria for selection. The distribution corresponding to the elastic constants using three experiments chosen via maximum information gain is shown in Figure 4.3.

The mean value of the posterior distribution in Figure 4.3 provides estimates of the elastic constants using the minimal amount of experimental data. These values are in very good agreement with values reported from literature [55]. Since uncertainty is rarely reported alongside parameter estimates, it is difficult to gauge the deviation from the estimated C_{44} value. A comparison of the values reported in literature, the previous study leveraging the same databases, and the current study are shown in Table 4.1.

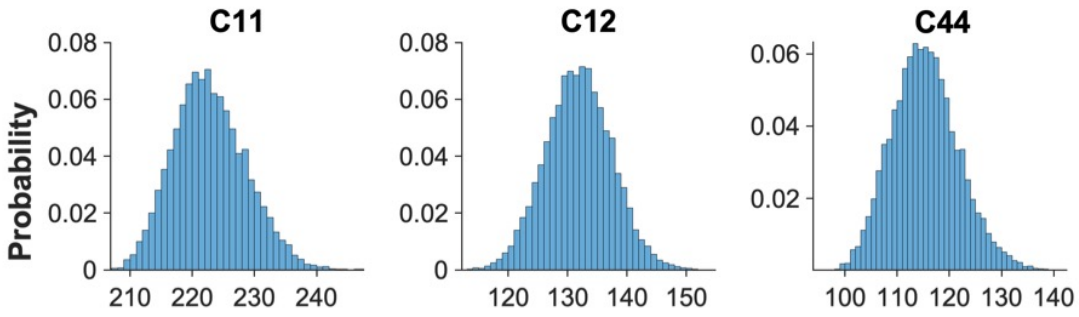

	C11	C12	C44
Mean (GPa)	222.81	131.87	115.39
STDEV	5.81	5.56	6.44

Figure 4.3. MCMC sampling of the posterior distribution of elastic constants, C11, C12, C44 for Fe-3%-Si using experiments chosen sequentially based on highest information gain.

Table 4.1. Comparison of the reported elastic constants, C11, C12, C44 for Fe-3%-Si.

	C_{11} (GPa)	C_{12} (GPa)	C_{44} (GPa)
Literature[a]	225	135	124
Previous Study[b]	216	132	122
Current Study	223	132	115

a. Simmons and Wang [55]

b.Patel et. al [7]

4.6 Discussion

Once a reduced-order model is established, the proposed workflow has the potential to be deployed for autonomous extraction of the intrinsic single crystal material properties from indentation experiments along with a rigorous quantification of their uncertainty. However, one should note that there are certain computationally intensive steps that could slow down the overall extraction effort. These steps include the distribution sampling via MCMC and the calculation of the information gain. Both computations take time due to the length of the Markov chain. Therefore, the following augmentations to the proposed workflow may be desirable in order to accelerate these computations. (1) Sampling of the intrinsic material parameter distributions can be performed through updating previous Markov chains via Sequential Monte Carlo [40,78], significantly reducing the time necessary to establish the parameter distributions at subsequent steps. (2) The computation of information gain metric can be expedited through the use of a reduced representation of sampled Markov Chains via importance sampling [40,42]. With such implementations, large grain maps can be scanned with real-time guidance as the measurements are being performed. Since both implementations essentially augment the Markov chain in order to hasten calculations, an evaluation of the resulting extracted parameters warrants careful attention and further investigation.

4.7 Conclusions

The workflow presented in this paper adopts a sequential strategy for the design of spherical indentation experiments to produce a highly informed pathway to the extraction of single crystal elastic constants. Within the workflow, distributions of the elastic

constants are systematically established by objectively identifying experiments which provide the most information gain. The prescribed workflow has identified that the maximal amount of information is gained within the first handful of experiments. Furthermore, estimates of the elastic constants using the first handful of experiments were in very good agreement with literature values. Therefore, careful attention should be taken in establishing the experimentally measured indentation properties for the handful of experiments identified early in the sequential design process. Such information itself provides very useful guidance to experimentalists. We further assert that the applicability of the suggested workflow extends past estimating single crystal elastic intrinsic properties. The current study implements the workflow to a relatively simple example. However, the workflow established is hypothesized to be highly robust to more complex applications in multiscale characterization of the material constitutive response. The main requirement of the workflow is the establishment of a likelihood function which links intrinsic properties of interest to an indentation property. Therefore, the workflow is potentially generalizable to other cases in the estimation of the intrinsic material properties as long as an appropriate reduced-order model can be established first. In this regard, it is pointed that the recently advanced framework of data-driven process-structure-property linkages [79-81] might prove very valuable in extending the application of the framework presented here to many other applications in multiscale materials modeling.

Acknowledgements

The authors acknowledge funding from AFOSR award FA9550-18-1-0330 (Program Manager: J. Tiley). AC acknowledges funding from the NSF Grant 1258425. RJ acknowledges funding from the NSF DMS Grant 1712642.

CHAPTER 5. ESTIMATION OF SINGLE PLY EFFECTIVE ANISOTROPIC ELASTIC CONSTANTS VIA SPHERICAL INDENTATION MEASUREMENTS

The following work was accepted for publication in the Journal, Meccanica in April 2020 under the title "Bayesian Estimation of single ply anisotropic elastic constants from spherical indentations on multi-laminate polymer matrix fiber-reinforced composite samples". Order of authorship is Andrew R. Castillo, and Surya R. Kalidindi. AC was responsible for data analysis and simulations, SK provided guidance. All contributed to preparation of the manuscript

5.1 Abstract

In this paper, the application of a recently formulated two-step Bayesian framework to the estimation of effective anisotropic elastic constants of single plies within a multi-laminate polymer matrix composite (PMC) is demonstrated, while using previously reported spherical indentation measurements within singular plies. Experimental spherical indentation measurements within the epoxy/fiber plies are inherently noisy due to local variation of the fiber volume fraction underneath the indenter. This paper demonstrates that the usage of a two-step Bayesian framework enables the extraction of reliable point estimates (and associated distributions) for the effective elastic constants from indentation modulus measurements conducted within single plies at different angles to the fiber orientations. The first step of the two-step Bayesian framework establishes the effective

elastic indentation modulus of a single ply as a function of its intrinsic elastic stiffness parameters and the angle between the indentation direction and the fiber orientation using a database of suitable finite element (FE) simulations. The second step involves the calibration of the indentation measurements from a given set of multi-laminate samples to the reduced-order model established in the first step. The second step is accomplished by sampling the posterior distribution of the single ply elastic parameters via Markov Chain Monte Carlo (MCMC) methods. This new framework is demonstrated in this study for an IM7/977-3 carbon fiber/epoxy multi-laminate sample.

5.2 Introduction

Laminated polymer matrix composites (PMC), comprised of stacked layers (referred as a laminate or multi-laminate) with each layer consisting of fibers orientated in a single direction (referred as a ply), have offered high tailorability and potential for the optimization of the mechanical properties to various applications across automotive, aerospace and civil infrastructure industries [82-85]. The modeling of the mechanical properties of the multi-laminate composite is generally pursued using homogenization schemes at two scales. At the first level, one takes the fiber and matrix properties and fiber volume fraction as inputs, and estimates the effective anisotropic properties of a singular ply [86,87]. At the second level, one takes the laminate properties and geometry (including stacking sequence and thicknesses of the individual plies) as inputs, and estimates the effective anisotropic properties of the PMC [88-93]. Consequently, the effective properties of a single ply play a critical role in the design of the laminated PMCs tailored for a selected

application. Direct experimental validation of the two-level composite models has been hampered by the lack of experimental protocols for the reliable estimation of the ply properties in a given multi-laminate sample [90,94-97]. The current practice relies on making single ply samples for experimental evaluation of their mechanical properties. However, one cannot be confident that the properties measured from these single ply samples would correspond well with the properties of the individual plies in a multi-laminate sample, because there are unavoidable differences in the processing conditions experienced in the production of these different samples.

Indentation techniques have been widely used in prior literature for establishing the local properties in heterogeneous samples, mostly aimed at evaluating the properties of microscale constituents or interfaces [5,98-100]. Recent advances in indentation instrumentation have tremendously improved the measurement resolution limits, and have now made it possible to measure local properties at submicron length scales. More specifically, recently developed spherical indentation protocols have demonstrated the consistent extraction of crystal-level indentation stress-strain responses from sub-granular load-displacement indentation measurements on polycrystalline metal samples [1,4,13,14,101]. These recent protocols are able to extract reliably the grain-level (i.e., grain lattice orientation dependent) indentation properties such as indentation modulus and indentation yield strength. Even more recently, novel protocols based on Bayesian statistics have been developed for estimating the intrinsic single crystal material properties (e.g., single crystal elastic stiffness parameters such as C_{11}, C_{12}, and C_{44} or the critical resolved shear strength) from the grain orientation-dependent indentation properties measured in different grains in a polycrystalline sample. These protocols fundamentally tackle an

inverse problem that calibrates the values of the intrinsic material properties of interest by matching the forward numerical (i.e., finite element method) solutions to the measurements obtained in the indentation experiments performed on a polycrystalline sample [7,10,44].

The spherical indentation stress-strain protocols have recently been extended to studies in carbon fiber/epoxy laminate composite. In a recent study, the spherical indentation stress-strain protocols were demonstrated for various orientations of single plies within a multi-laminate system [102]. Indentation moduli and indentation yield strengths at different declination angles (i.e., angle between the indentation direction and the fiber direction in a single ply) were reliably extracted from a multi-laminate PMC sample. The measured values of the indentation moduli were shown to decrease dramatically with an increase in declination, angle and were found to be reasonably consistent with forward predictions from finite element simulations. This recent study has demonstrated the potential of the spherical indentation stress-strain protocols for obtaining reliable and repeatable measurements of the local mechanical response of a single ply from a multi-laminate PMC sample. The next logical step in this research is to explore methods to extract the homogenized intrinsic properties of the individual plies from the indentation moduli measured at different declination angles (by indenting the differently oriented plies in a multi-laminate PMC sample). More specifically, the homogenized elastic response of a single ply (each ply is a composite comprising matrix and fibers) can be assumed to exhibit transverse isotropy and is represented by a set of five intrinsic stiffness parameters denoted as C_{11}, C_{12}, C_{13}, C_{33}, and C_{44}; these five parameters are adequate to fully define the ply's fourth-rank elastic stiffness tensor.

As already mentioned, the estimation of the intrinsic materials properties from the indentation properties demands a difficult inverse solution. This is because the most reliable forward models for this problem require the use of a computationally intensive finite element (FE) model of the indentation test. For the present case, the forward model would take the single ply properties as inputs, and predicts the indentation stress-strain responses at different declination angles. Given the high computational cost of the FE models of the indentation tests, inverse solutions need an efficient strategy. In recent work [44], a two-step Bayesian framework was proposed to address this class of problems, and its viability was demonstrated with the extraction of intrinsic crystal-level properties from indentation measurements in polycrystalline cubic and hcp metal samples. The first step in this protocol establishes a high fidelity, low computational cost, reduced-order model to take place of the computationally intensive FE model of the spherical indentation test. The second step calibrates the single ply properties of interest by using the experimentally measured indentation properties at different declination angles using the reduced-order model established in the first step together with a Markov Chain Monte Carlo (MCMC). One of the salient aspects of the proposed two-step Bayesian framework is that it also provides an estimate of the uncertainty (quantified as variance) in the estimated intrinsic properties. In this work, we will extend and demonstrate the viability of using the two-step Bayesian framework for the estimation of the single ply elastic stiffness parameters from the spherical indentation measurements on a multi-laminate PMC sample. It should be noted that the PMC samples studied here exhibit significantly higher levels of anisotropy and inherent variance in the indentation measurements, when compared to the polycrystalline cubic and hcp metal samples studied earlier.

5.3 Methods

5.3.1 Experimental Data

The elastic contact between two isotropic homogenous bodies with quadratic surfaces is described by Hertz theory as

$$P = \frac{4}{3} E^* R_{eff}^{\frac{1}{2}} h_e^{\frac{3}{2}} \tag{5.1}$$

where P is the indenter load, h_e is the elastic indentation displacement, R_{eff} is the effective radius of the indenter-sample system, and E^* is the effective indentation modulus. Although the measured E^* generally reflects the effective indentation modulus of the indenter-sample system, one can account for the elastic deformation in the indenter itself and recover the indentation modulus of the sample alone [17]. In the treatment presented here, it will be assumed that such corrections have been made, i.e., E^* denotes the indentation modulus of the sample. In recent work [102], spherical indentation protocols were used successfully to measure the effective indentation moduli at four different declination angles (denoted by ϕ) for single plies in an IM7/977-3 carbon fiber/epoxy multi-laminate sample. These measurements are summarized in Table 5.1, and are used in this study for the estimation of the single ply elastic constants. Note that the measurements show that the indentation moduli decrease significantly with an increase in the declination angle, and exhibit high levels of variance in the measurements. The high variance was attributed to the expected large variance in the local fiber volume fractions in the primary zones of the indentations performed [102].

Table 5.1. Previously reported measured indentation moduli for single plies in an IM7/977-3 carbon fiber/epoxy multi-laminate sample [102].

Ply Orientation (ϕ)	Number of Tests	Mean Indentation Modulus (GPa)	Standard Deviation (GPa)
0	29	43.2	8.7
30	14	29.9	4.0
60	18	16.6	1.7
90	28	12.4	3.0

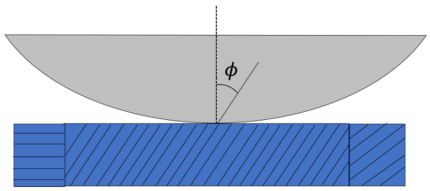

5.3.2 Finite Element Models for Effective Indentation Moduli of Plies

The simulated domain is treated as homogenous, transversely isotropic solid, whose elastic response in the sample reference frame is fully described by the set of five elastic constants, $\boldsymbol{c} = \{C_{11}, C_{12}, C_{44}, C_{33}, C_{13}\}$ and the specified declination angle, ϕ, between the fiber orientation in the single ply and the indentation direction. The sample size simulated was chosen to be 670 μm × 670 μm × 335 μm, while the indenter radius was chosen to be 500 μm, consistent with the experiments. The simulated sample size was chosen to be much larger than the indentation zone size (~50 μm reported in experiments) [102]. The mesh used is adopted from prior work, and consisted of 12,610 C3D8 continuum 3-D elements [7,102]. The FE model used in this work has been previously validated for the extraction of effective indentation moduli of various material systems, including cubic metal single crystals [7] and hexagonal metal single crystals [44]. The FE model has also been validated by direct comparisons with the analytical solutions reported by Vlassak and Nix [5]. Most recently, this FE model has been validated through the direct comparison of simulated and experimental values in single plies within PMC multi-laminate samples [102].

5.3.3 Bayesian Framework for the Extraction of Intrinsic Material Properties

The Bayesian framework employed here is adopted from prior work [44], and is briefly reviewed next. In this approach, the measured experimental indentation modulus for the i-th ply orientation (i.e., declination angle, ϕ) is modeled as

$$E_i^* = E_{sim}^*(\boldsymbol{c}, \phi_i) + \epsilon_i \tag{5.2}$$

where $E_{sim}^*(\boldsymbol{c}, \phi_i)$ denotes the FE-simulated indentation modulus corresponding to a set of effective elastic constants and a single ply orientation, and $\epsilon_i \sim \mathcal{N}(0, \sigma_i^2)$ denotes a stochastic noise term. It is implicitly assumed here that the FE simulated $E_{sim}^*(\boldsymbol{c}, \phi_i)$ exhibits negligible variance. Let $\{\boldsymbol{E}_{exp}^*, \boldsymbol{\Phi}_{exp}\}$ denote the set of experimental indentation moduli, $\boldsymbol{E}_{exp}^*$, measured at the corresponding ply orientations, $\boldsymbol{\Phi}_{exp}$. The likelihood for n experimental measurements across multiple plies (denoted $\{\boldsymbol{E}_{exp}^*, \boldsymbol{\Phi}_{exp}\}$) is expressed as

$$p\left(\boldsymbol{E}_{exp}^* \middle| \boldsymbol{c}, \boldsymbol{\Phi}_{exp}\right) = \prod_i^n \frac{1}{\sqrt{2\pi}\sigma_i} exp\left\{\frac{-(E_i^* - E_{sim}^*(\boldsymbol{c}, \phi_i))^2}{2\sigma_i^2}\right\} \tag{5.3}$$

where the variance, σ_i^2, is directly measured from experiments in the i-th ply (with a declination angle, ϕ_i). Inference of the effective elastic constants, $\boldsymbol{c}$, for the observed experimental data can be expressed by Bayes rule:

$$p\left(\boldsymbol{c} \middle| \boldsymbol{E}_{exp}^*, \boldsymbol{\Phi}_{exp}\right) \propto p\left(\boldsymbol{E}_{exp}^* \middle| \boldsymbol{c}, \boldsymbol{\Phi}_{exp}\right) p(\boldsymbol{c}) \tag{5.4}$$

Assuming a uniform prior for $p(\boldsymbol{c})$ along with the likelihood function shown in Eqn. (5.3), Eqn. (5.4) allows for the application of MCMC methods for sampling the posterior distribution on the effective intrinsic material properties [29,35]. MCMC algorithms seek

to generate a sequence, known as a Markov Chain, which converges to a target posterior distribution by accepting/rejecting a large number of proposed transitions across a finite parameter space based on an acceptance probability [44]. Specifically, the Single Component Metropolis Hastings (SCMH) algorithm is adopted in this work to generate transitions across the multivariate parameter space of effective elastic constants [35,44]. When implementing SCMH, the acceptance probability of a transition is solely determined by the ratio between candidate and current values evaluated by Eqn. (5.4). In practice, these methods often require tens of thousands of evaluations of the likelihood function to ensure convergence [37]. In this work, 50,000 samples are drawn via SCMH in order to generate a Markov Chain. Due to the probabilistic nature of MCMC, it is desirable to run the algorithm multiple times, randomly selecting initial starting points to ensure that independently sampled Markov Chains converge to similar distributions. The high computational costs associated with the execution of the FE models of indentation make it impractical to use the FE indentation models directly in the computations described above. The only practical approach for addressing this challenge is to first establish a reduced-order model.

Recent work [44] has demonstrated the successful development of a reduced-order model that captures the dependence of indentation modulus on the crystal orientation of the indented grain and an arbitrary set of single crystal elastic constants. The development of this reduced-order model involved the use of an expanded Fourier basis and the calibration of the Fourier coefficients via Bayesian Linear Regression (BLR). The usage of BLR provides a valuable quantification of uncertainty associated with the predictions from the reduced-order model [30]. These same strategies are adopted in this work to establish a

reduced-order model for $E^*_{sim}(\boldsymbol{c}, \phi)$. In order to establish the reduced-order model, a database of finite element simulations covering the relevant input parameter space is necessary. The quantification of uncertainty provided by BLR enables the deployment of sequential strategies to build a simulated database by focusing on areas of high predictive uncertainty. Simulations can be continually performed until sufficient performance of the reduced-order model is achieved, as determined by various error metrics. The implementation of this strategy in previous work has shown a significant reduction in the number of simulations necessary to establish a high fidelity reduced-order model in comparison with traditional regression approaches [7,44].

The Fourier basis used in the development of a reduced-order model in the previous work were obtained by compounding symmetrized surface spherical harmonics (to represent functions over the orientation space) with Legendre polynomials (to represent functions over the ranges of the values for the single crystal material constants) [7,44]. The advantage of this representation was the ability to capture the underlying crystal symmetries exhibited by the material system. We note that the local orientation of any material system with respect to a defined sample frame can be represented by a set of Bunge Euler angles $\{\varphi_1, \phi, \varphi_2\}$ [22]. Since any rotation about the sample normal does not affect the measured indentation properties, it can be seen that the indentation properties are independent of φ_1 [5,18,22]. Furthermore, the indentation modulus of the transversely isotropic material simulated in this work is also independent of φ_2 (i.e., a rotation of the ply about the fiber axis also does not influence the measured indentation response). As a result of these considerations, the desired reduced-order model [44] can be expressed as

$$E_{sim}^{*} \approx \hat{E}^{*}(\boldsymbol{c}, \phi) = \sum_{l=0}^{L} \sum_{\boldsymbol{q}}^{\boldsymbol{Q}} A^{l\boldsymbol{q}} P^{l}\ (cos\ (\phi)) \tilde{P}^{\boldsymbol{q}}(\bar{\boldsymbol{c}}) \tag{5.5}$$

$$\bar{c}_j = \frac{2c_j - c_j^{min} - c_j^{max}}{c_j^{max} - c_j^{min}} \tag{5.6}$$

where $P^{l}\ (\cos\phi)$ denote Legendre polynomials expanded over the ply orientation space [22], and $\tilde{P}^{\mathbf{q}}(\bar{\mathbf{c}})$ denote a multivariate Legendre polynomial product basis. In other words, one can express $\tilde{P}^{\mathbf{q}}(\bar{\mathbf{c}}) = P^{q_1}(\bar{c}_{11})P^{q_2}(\bar{c}_{12})P^{q_3}(\bar{c}_{44})P^{q_4}(\bar{c}_{33})P^{q_5}(\bar{c}_{13})$, where $\boldsymbol{q} = (q_1, q_2, q_3, q_4, q_5)$ forms a multi-index array, each element of which is a nonnegative integer allowed to vary from 0 to the selected maximum degree, Q, i.e., $q_j \in [0, Q]$. For the proper application of the Legendre Polynomial basis, each of the elastic constants are rescaled over their respective ranges [74] as shown in Eqn. (5.6), where c_j^{max} and c_j^{min} are the maximum and minimum values of the j-th elastic constant. Q and L denote the truncation levels adopted in the formulation of Eqn. (5.5). We note that the degree of the Legendre polynomials expanded about the orientation space are selected to be strictly even to fully reflect the symmetries present in the transversely isotropic material system [22]. The model coefficients, $\boldsymbol{A}$, are established using the aforementioned sequential model building process deployed successfully in previous work [44].

5.4 Results

5.4.1 Reduced-Order Model Building

In order to evaluate the likelihood function in Eqn. (5.3), a high fidelity reduced-order model must be established covering a suitable parameter space of the elastic intrinsic material parameters. The first step in this process is the identification of the extent of the input parameter space to be covered by the reduced-order model. To identify this space, simplified estimates of the effective elastic properties of a ply [87] can be computed using the constituent fiber/matrix properties in the following equations:

$$E_3 = E_{f3}V_f + E_m V_m \tag{5.7}$$

$$E_1 = E_2 = \frac{E_m}{1 - \sqrt{V_f}(1 - {E_m}/{E_{f2}})} \tag{5.8}$$

$$G_{23} = G_{13} = \frac{G_m}{1 - \sqrt{V_f}(1 - {G_m}/{G_{f23}})} \tag{5.9}$$

$$G_{12} = \frac{G_m}{1 - \sqrt{V_f}(1 - {G_m}/{G_{f12}})} \tag{5.10}$$

$$v_{23} = v_{f23}V_f + v_m V_m \tag{5.11}$$

where E,G, v denote the Young's moduli, shear moduli, and Poisson's ratios, respectively, the fiber direction corresponds to the 3-axis, and the subscripts *m* and *f* refer to the matrix and the fiber components, respectively [86]. A range of fiber volume fraction, V_f, between

20%-80% was used in Eqs. (5.7)-(5.11) in order to delineate the domain of the input parameter space for the desired reduced-order model. For these computations, the constituent fiber and matrix properties were taken from manufacturers' data (Hexcel HexTow IM7, CYCOM 977-3 Epoxy Resin) and reported values in literature [49,102,103]. The fiber properties were set as $E_{f3} = 276\ GPa, E_{f1} = 26\ GPa, G_{f12} = 7\ GPa, G_{f23} = 20\ GPa, v_{f23} = 0.3,$ while the matrix properties were set as $E_m = 3.3\ GPa, G_m = 1.2\ GPa, v_m = 0.35$. The ply stiffness values computed from Eqs. (5.7)-(5.11) were then converted to the corresponding values of $\boldsymbol{c}$ used in the development of the framework presented in this paper using relations already established in literature [86]. The extents (i.e., ranges) for the values of the components of $\boldsymbol{c}$ covered by the present work are summarized in Table 5.2. The full range of the ply orientation space, $0 \leq \phi \leq 90$ degrees, was included in this work.

Table 5.2. Bounds of each elastic stiffness constant considered in this study. Bounds were computed in accordance to Eqs. (5.7)-(5.11) considering a fiber volume fraction between 20%-80%.

	C_{11}(GPa)	C_{12}(GPa)	C_{44}(GPa)	C_{33}(GPa)	C_{13}(GPa)
Max	30.8	22.1	7.7	239	16.7
Min	5.6	1.3	2.2	65.9	2.2

As previously mentioned, a sequential model building process is adopted from prior work [44] in order to efficiently establish a reduced order model within the identified input parameter space. The implementation of this process includes the establishment of an initial reduced-order model using an initial data set, followed by the selection of additional

simulations based on predictive uncertainty. An initial data set of 740 simulations was generated from unique sets of inputs, $\{\boldsymbol{c}, \phi\}$, determined by a Max-Pro Latin Hypercube Design within the extents of the parameter space identified in Table 5.2, while ensuring material stability (i.e., positive eigen values for the stiffness tensor) [56,104]. The number of simulations for the initial data set was selected to be close to the number of coefficients associated with a reduced-order model established for the single crystal elastic constants in hcp crystals (i.e., truncation level Q=2, L=4 resulting in 729 model coefficients) [44]. Inputs to additional simulations were selected from another Max-Pro Latin Hypercube Design of 2200 simulations in accordance with the sequential model building strategy adopted from previous work [44].

Given the high levels of anisotropy in the composite plys studied here compared to the hcp crystals studied in previous work [44], it was anticipated that a higher level of truncation would be necessary for the present work. Using cross-validation error (CVE) approaches [31], the aforementioned model building process identified that a truncation level of Q=2, L=6 (CVE=0.93 GPa) provides significant improvement over the truncation level Q=2, L=4 (CVE=1.57 GPa) for the present work. The necessity of higher model complexity for the present case compared to the previous work [44] involving hexagonal single crystals is quite reasonable due to a notable increase in the anisotropy in the present work. The degree of elastic anisotropy can be quantified by the universal elastic anisotropic index, $\mathbb{A}$, defined as [58]

$$\mathbb{A} = 5\frac{G_v}{G_r} + \frac{K_v}{K_r} - 6 \tag{5.12}$$

where K and G are the bulk and shear moduli provided by Voigt and Reuss estimates (indicated by subscript v and r, respectively) of randomly oriented homogenized plies within a macroscopically homogenous multi-laminate system [58]. The arithmetic mean of $\mathbb{A}$ encountered in the training data used in this study is 17.4 while previous studies involving hcp single crystals encountered a mean anisotropic index of 2.2 [44].

A total of 860 simulations were sequentially added (1600 simulations total) to achieve convergence in the model building process. Convergence in the model building process is determined by changes in the model coefficients, $\boldsymbol{A}$, established at every step. Changes in the model coefficients as simulations are added is shown in Figure 5.1. It is seen that the model building process described in this paper produces a robust model.

An additional 600 simulations were added via the sequential design process for critical validation of the predictive performance of the reduced-order model. The accuracy of the predictions over the training and test sets is summarized in Figure 5.2. The reduced-order-model produced in this work shows very good predictive capability, exhibiting a mean absolute prediction error of 0.75 GPa over the test set. We note, predictions with a relatively high error (greater than 3.5 GPa) consistently corresponded to high values of $\mathbb{A}$ ranging from 75 to 215.

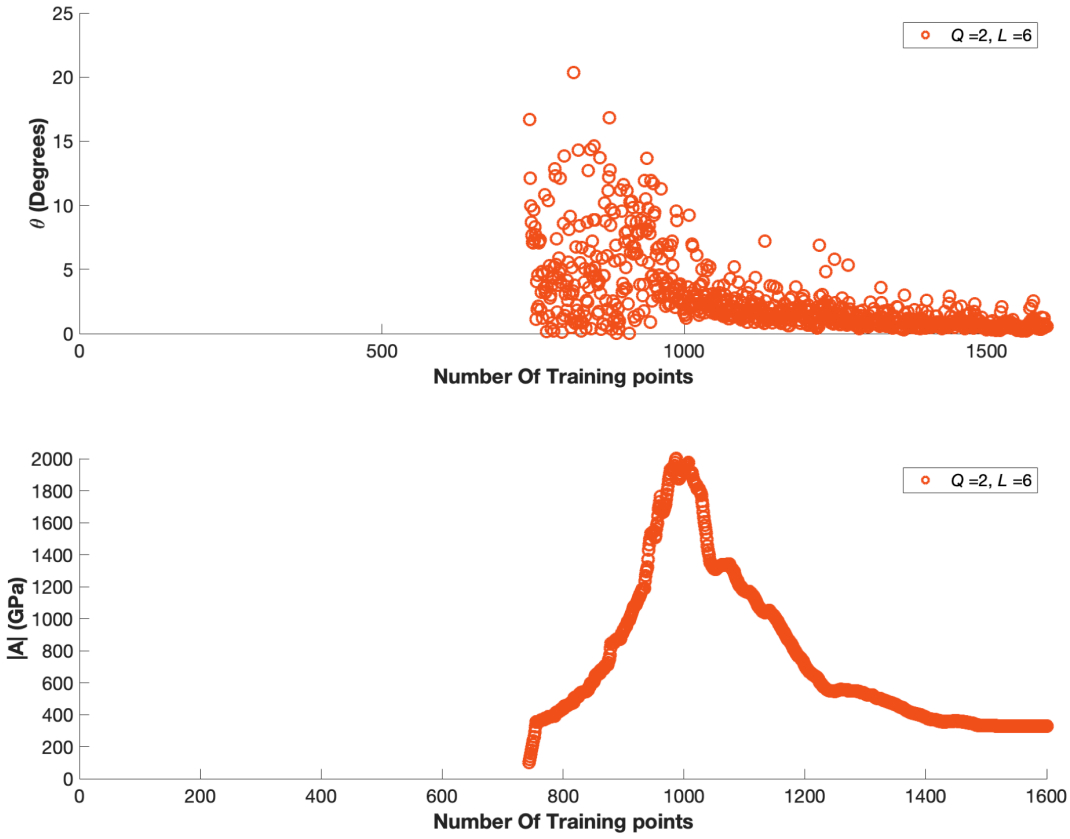

Figure 5.1. Convergence metrics during the building of the reduced-order developed in this work, corresponding to truncation levels Q=2, L=6. Top: The angular difference of the vector of model coefficients due to the addition of new simulations is shown to converge around 1600 simulations. Bottom: The magnitude of the vector of model coefficients shows a similar convergence.

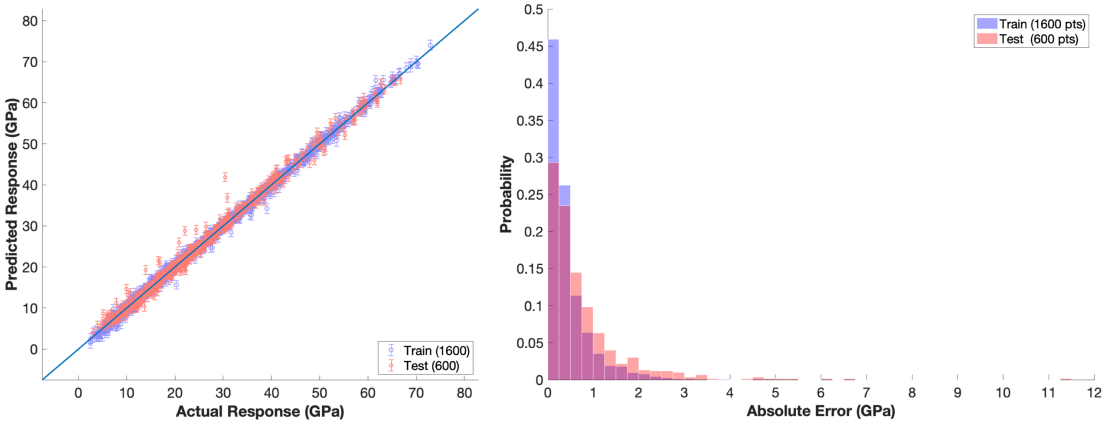

Figure 5.2. The accuracy of the reduced-order model built in this work for the prediction of the FE simulated effective indentation modulus for input values of the single ply stiffness distributed over the ranges specified in Table 5.2 and ply orientations ranging between 0 and 90 degrees. Left: Comparison of predicted and actual FE simulated effective indentation modulus for test and training data. Right: Corresponding histograms of the absolute error for test data and training data.

5.4.2 Estimation of Single Ply Stiffness from Indentation Measurements

We now shift focus to sampling the posterior distribution of ply elastic constants, $\boldsymbol{c} = \{C_{11}, C_{12}, C_{44}, C_{33}, C_{13}\}$, given a set of experimentally measured indentation moduli at different declination angles in individual plies of a multi-laminate sample. Following the establishment of the reduced-order model in the previous subsection, the likelihood function in Eqn. (5.3) can readily be evaluated for the available experimental data (presented in Table 5.1). In accordance with the methodology described earlier, 50000 samples are drawn from the posterior distribution shown in Eqn. (5.4) using a Single Component Metropolis Hastings algorithm [44]. The sampled posterior distributions of the effective elastic constants are shown in Figure 5.3. The mean values were found to be $\boldsymbol{c} = \{20.1, 11.7, 4.9, 155.4, 9.9\}$ GPa.

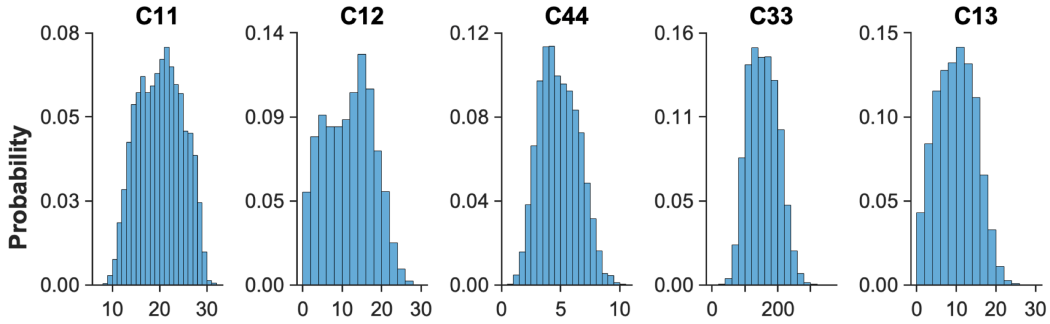

	C11	C12	C44	C33	C13
Mean (GPa)	20.1	11.7	4.9	155.4	9.9
STDEV	4.7	6.1	1.6	45.2	4.9

Figure 5.3. Extracted posterior distributions of the single ply elastic stiffness parameters from the available experimentally measured indentation moduli presented in Table 5.1.

Literature regarding the extraction of the (homogenized) single ply elastic properties from multi-laminate samples is sparse. To provide a basis for comparison, the effective properties of a corresponding ply with a fiber volume fraction of 63% (reported in the experiments) estimated using Eqns. (5.7)-(5.11) [102] is shown in Table 5.3.

Table 5.3. Comparison of effective elastic constants extracted using MCMC to estimates [102] obtained using Eqs. (5.7)-(5.11). We note the sampled distributions provide a measure of uncertainty with respect to the extracted ply elastic stiffness constants.

	C_{11}(GPa)	C_{12}(GPa)	C_{44}(GPa)	C_{33}(GPa)	C_{13}(GPa)
V_f: 63%	15.1	8.0	4.9	179.6	7.2
Sampled Mean	20.1 ± 4.7	11.7 ± 6.1	4.9 ± 1.6	155.4 ± 45.2	9.9 ± 4.9

Interestingly, all of the estimates obtained using the simplified equations presented in Eqs. (7-11) lie close to or within a single standard deviation of the respective sampled means. The noticeably higher discrepancy for the value of C_{11} is consistent with observations in prior experimental work when comparing the experimental data in Table 5.1 to FE simulations using initial effective property estimates [102]. We emphasize that one of the main advantages of the proposed framework is that we obtain useful measures of the uncertainty related to the estimated single ply elastic stiffness parameters from the spherical indentation measurements. Note that the uncertainty is relatively higher for the estimates of the "off diagonal" stiffness constants, C_{12} and C_{13}. This is because the indentation modulus exhibits a relatively low sensitivity to changes in these parameters across the ply-orientation space [77]. The relatively high uncertainty levels in Table 5.3 could be reduced if additional indentation measurements at additional ply orientations become available. Determination of where to perform additional experiments can be qualitatively determined by viewing the predictions of the reduced-order model over the

ply orientation space. The variation in the predictions of the reduced-order model due to the MCMC process is shown in Figure 5.4.

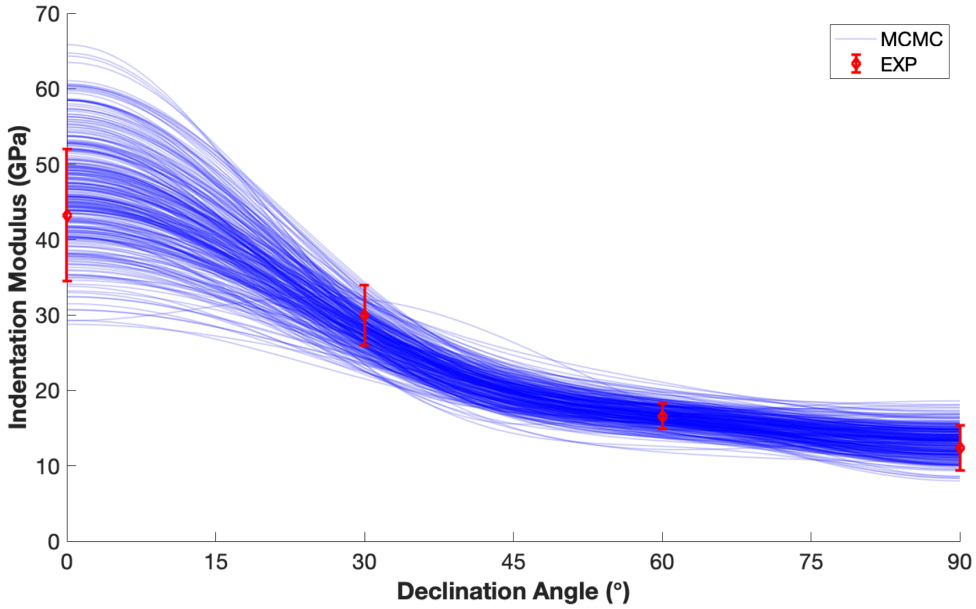

Figure 5.4. The sampled MCMC posterior distribution for the prediction of indentation moduli as a function of the indentation declination angle. Highest uncertainty is seen at low declination angles, suggesting more information gathered at these angles will provide the best improvement in the extracted effective intrinsic properties.

The predictions of the variation of the indentation moduli with the indentation declination angle, obtained from MCMC sampling, conform closely to the measured experimental indentation dataset verifying that the underlying variation in local indentation modulus observed within the single plies is effectively being communicated to the extracted distributions. However, significant variation in predictions occurs at lower declination angles, suggesting there would be value from additional experiments performed at lower declination angles. We note that the recently developed work in the sequential selection of indentation experiments based on highest information gain [47] may prove useful in leveraging the extracted distributions of effective elastic constants in order to quantitatively

determine the precise orientation of single plies to focus upon that may best sharpen the C_{12} and C_{13} distributions.

5.4.3 Bulk Multi-laminate Property Estimation

The effective elastic properties of a multi-laminate system can be tailored by manipulating the configuration of the constituent plies. Simple homogenization theories have often provided estimates for the effective properties of various configurations of a multi-laminate system. Therefore, it is desirable to incorporate the distributions of effective elastic constants sampled in Section 3.2 into such homogenization schemes in order to examine how the uncertainty in the single ply properties are propagated to the effective properties at the next higher length scale. Specifically, the overall elastic properties of a multi-laminate system with m oriented plies can be estimated using an iso-strain model [87,88] expressed as

$$\overline{C}_{ijkl} = f(\boldsymbol{c}) = \sum_{t=1}^{m} C_{pqrs} V^t Q^t_{ip} Q^t_{jq} Q^t_{kr} Q^t_{ls} \tag{5.13}$$

where $\boldsymbol{C}$ denotes the 4-th rank elastic stiffness tensor composed from $\boldsymbol{c}$, V^t is the volume fraction of the t-th ply and Q^t denotes the rotation matrix which transforms the material principle frame to the sample frame in accordance with the t-th ply orientation. We note, $\overline{\boldsymbol{C}}$ is the effective 4-th rank stiffness tensor of the multi-laminate system. In practice, symmetric ply configurations are often chosen such that a multi-laminate system likely exhibits an orthotropic, or quasi-isotropic elastic response [49,86,105,106]. Consequently, the effective Young's modulus in the longitudinal direction of such multi-laminate systems

is commonly reported in experiments [49,107]. Let $g(\overline{\boldsymbol{C}})$ be the function which computes the effective Young's modulus, denoted $\bar{E}$, in the longitudinal direction of an elastic orthotropic or quasi-isotropic multi-laminate system. We recall this relation is readily available in literature [86]. In order to take into account the distributions of effective elastic constants extracted in Section 3.2, the *expected* effective Young's modulus, can be computed as

$$\mathbb{E}\left(\bar{E}\middle|\boldsymbol{E}^{*}_{exp},\boldsymbol{\Phi}_{exp},\boldsymbol{c}\right)=\int g(f(\boldsymbol{c}))p(\boldsymbol{c}|\boldsymbol{E}^{*}_{exp},\boldsymbol{\Phi}_{exp})d\boldsymbol{c} \tag{5.14}$$

where the expectation function, $\mathbb{E}$, is readily approximated using the Monte-Carlo estimate [75] by

$$\mathbb{E}\left(\bar{E}\middle|\boldsymbol{E}^{*}_{exp},\boldsymbol{\Phi}_{exp},\boldsymbol{c}\right)\approx\frac{1}{N}\sum_{i=1}^{N}g(f(\boldsymbol{c}_i)) \tag{5.15}$$

where $\boldsymbol{c}_i$ enumerates the $N=50{,}000$ samples of the Markov Chain. The expected effective Young's Moduli in the longitudinal direction computed for various configurations of the IM7/977-3 epoxy-carbon fiber multi-laminate system are compared to previously reported experimentally measured values [49] in Table 5.4.

The computed expected longitudinal stiffness using the distributions extracted in Section 3.2 are in very good agreement with experimentally measured values. Furthermore, the reported standard deviations correspond to 10 separate MCMC chains. The small deviations between the predictions of these chains indicate robustness of the MCMC sampling methodology. The above exercise demonstrates how the distributions of in-situ

elastic ply properties may provide accurate predictions of the homogenized properties for arbitrary configurations of multi-laminate composite systems.

Table 5.4. Comparison of homogenized longitudinal Young's Modulus predicted using posterior distributions of single ply elastic stiffness constants to the longitudinal Young's Modulus measured experimentally for multiple multi-laminate configurations.

Multi-laminate Ply Configuration	**Experimental Longitudinal Young's Modulus**	**Expected Longitudinal Young's Modulus**	**STDEV of Expected Longitudinal Young's Modulus**
$[0/+45/90/-45]_{2S}$	58.9	57.6	0.6
$[+60/0/-60]_{3S}$	59.5	57.9	0.6
$[+30/+60/90/-60/-30]_{2S}$	38.1	39.5	0.4

5.5 Conclusions

A new framework has been presented and demonstrated for the extraction of homogenized single ply anisotropic elastic constants from available spherical indentation measurements on single plies within a multi-laminate PMC sample. The available experimental measurements exhibited varying levels of variance attributed to a large variance in the local fiber volume fractions in the primary zones of indentation. The Bayesian framework extended from prior work was successfully employed to sample distributions of the ply anisotropic elastic constants which reflect the uncertainty (expressed as variance) in the underlying experimental measurements. This is accomplished through the establishment of a likelihood function which requires a FE model of the spherical indentation experiment. In practice, a large number of evaluations of the likelihood function is necessary to discern the distributions of effective elastic constants. In order to expedite these computations, a high fidelity reduced-order model is established for the FE model of the indentation

measurement. Following the determination of the distribution of effective elastic constants pertaining to single plies, high fidelity estimates of bulk elastic properties of multi-laminate samples with various ply configurations were obtained. This was accomplished using the extracted distributions of effective elastic constants coupled with existing composite lamina theory.

Acknowledgements

The authors acknowledge support from ONR Grant N00014-18-1-2879.

CHAPTER 6. ESTIMATION OF CRYSTAL LEVEL ELASTIC-PLASTIC PROPERTIES FROM THE PRIMARY ALPHA PHASE OF TI ALLOYS VIA SPHERICAL INDENTATION MEASUREMENTS

The following manuscript is in preparation under the tentative title “Bayesian Estimation of crystal-level elastic-plastic properties of primary-alpha phase of different chemical compositions from spherical indentation measurements on polycrystalline Ti alloy samples”. Order of authorship is Andrew R. Castillo, Aditya Venkatraman and Surya R. Kalidindi. AC was responsible for data analysis, AV was responsible for simulations and SK provided guidance. All contributed to preparation of the manuscript.

6.1 Introduction

Alpha-beta titanium alloys exhibit high strength to weight ratio together with the excellent corrosion resistance and fatigue properties desired in various aerospace applications. The microstructures in these alloys exhibit rich features that typically include the single phase hexagonal close-packed primary-α grains and the secondary-α grains exhibiting varying morphologies comprised of alpha laths in a metastable bcc matrix. The microstructure features as well as the chemical compositions of the alloys are known to play important roles in the properties exhibited by these alloys. The large design space for these alloys has made it difficult to establish the precise connections between the microstructure features of Ti alloys and their mechanical properties [108-110] .

There has been significant effort in developing physics-based microstructure sensitive multiscale models which take into account the salient information of the material structure to predict the mechanical properties for Ti alloys at higher length scales [20,111-115]. These physics-based models leverage a variety of crystal plasticity theories in order to communicate the deformation at the crystal level to the macroscale. Commonly used examples of such frameworks include visco-plastic self-consistent crystal plasticity models as well as Taylor type crystal plasticity models [19,116]. In order to implement these models, knowledge of properties defined at the grain-scale (i.e., slip resistances of different slip families at the single crystal level) is essential. Such information is critically important for hexagonal metals such as Ti alloys, which are known to exhibit rich dual-phase microstructures with each constituent phase exhibiting high levels of plastic anisotropy at the grain-scale [112,117].

Mechanical characterization of crystal level properties have often been pursued using "miniaturized" versions of conventional methods of testing [117-120]. Examples of such tests includes microscopic compression tests on single crystal micro pillars produced using a focused ion beam [118] as well as cylindrical rods grown from single crystals [117]. Recent approaches have also attempted the calibration of crystal level parameters through the comparison of experimental and CPFE simulated load-deflection curves from bend tests on single crystal micro cantilever beams manufactured using a focused ion beam [121]. Other efforts in this vein include the calibration of grain scale properties through the comparison of experimental and CPFE simulated topographical surface patterns arising during conical nanoindentation experiments performed within singular grains at various orientations [8,12]. The lattice orientation of the individual test specimens are chosen

specifically to activate slip on selected slips systems of interest. These tests are often paired with slip trace analysis in order to verify that the targeted slip systems have been activated. Such approaches require highly specialized equipment and a sophisticated level of experimental skills and expertise. These approaches incur significant time and effort, and the results obtained are often highly sensitive to the intricate multi-step sample preparation processes required.

As an alternative to the direct experimental approaches described above, the determination of crystal level elastic-plastic properties has also been attempted through the calibration of physics-based model predictions with experimental measurements at the macroscale. As previously mentioned, the crystal level parameters serve as inputs to crystal plasticity-based simulation tools [19,20,116,122]. Consequently, one can calibrate the crystal level parameters in these models by matching the model predictions with the available experimental data (e.g., load-displacement curves, microstructure evolution documented by electron back-scattered diffraction (EBSD) maps) [19,20,112,116,122,123]. Since the experimental and simulation results are largely matched at the macroscale, these approaches do not often identify unique values for the crystal-level properties. In other words, one often identifies multiple sets of values for the crystal-level properties that provide similar levels of agreement between the predictions and measurements at the macroscale. A crucial shortcoming of many of these methods is, it is often exceedingly difficult to reliably quantify the uncertainty of estimates obtained due to the substantial amount of effort (experimental or simulated) needed. Therefore, a systematic strategy should be employed which can quantify and propagate the uncertainty due to the experimental measurements to the extracted crystal level properties.

Instrumented indentation techniques have demonstrated to be capable of providing high throughput reliable measurements at multiple length scales (down to submicron) in local volumes of material [4,8,15,62,101,124]. Currently employed strategies for extracting intrinsic material properties from indentation tests have generally involved the calibration of physics-based finite element (FE) models of these tests to the corresponding set of experimental indentation measurements [7,8,44,124]. It has been previously demonstrated that the estimation of intrinsic material parameters is much more robust when the calibration is attempted in the form of the normalized indentation stress-strain curves as opposed to directly matching the load-displacement curve. One such example demonstrated the capability of extracting the initial slip resistance of a polycrystalline sample of Fe-3%-Si sample using a collection of experimental indentation measurement performed in multiple grains [10]. The aforementioned work sought to provide robust estimates of slip resistances; however, did not attempt to propagate uncertainty from experimental estimates to the initial slip resistance extracted. In recent work, a two-step Bayesian framework was proposed to address this issue, and its viability was demonstrated with the extraction of intrinsic crystal-level elastic properties from indentation measurements in polycrystalline cubic and hcp metal samples [44]. The first step in this protocol establishes a high fidelity reduced-order model in place of the computationally intensive FE model of the spherical indentation test with respect to the crystal level parameters of interest (e.g. initial slip resistance values, single crystal elastic constants). We note the establishment of this reduced order model presents a singular computational cost, but afterwards is readily applicable across a multitude of alloys to be considered [6,44]. The second step calibrates the crystal level properties of interest by using a

collection of experimentally measured indentation properties within single crystals at various orientations using the reduced-order model established in the first step together with a Markov Chain Monte Carlo (MCMC). One of the salient aspects of the proposed two-step Bayesian framework is that it also provides an estimate of the uncertainty (quantified as variance) in the estimated crystal level properties.

In this work the two step Bayesian framework will be used to extract the values for the single crystal elastic constants, $\{C_{11}, C_{12}, C_{44}, C_{13}, C_{33}\}$, as well as the initial slip resistance values $\{s_{pr}, s_{ba}, s_{pyr-a}, s_{pyr-ca}\}$, and associated uncertainties quantified for the primary α phase of a collection of Ti alloys. Following the extraction step, a critical evaluation of the uncertainties of the extracted crystal level properties across the selected alloys will be performed. Previous studies involving the extraction of plastic crystal level properties for single phase cubic polycrystalline Fe-3%-Si samples only considered a single slip resistance value. The extraction effort here is complicated from the previous studies by the number of slip resistances necessary to consider. The difficult is further compounded by (i) the plastic anisotropy exhibited in HCP metals (ii) the exploration of the relatively high dimensional parameter space defined by slip resistances and crystallographic single orientations. We recall the final challenge of this study is the generation of a comprehensive dataset of single crystal elastic-plastic properties consistent across a collection of available Ti alloys using experimental spherical indentation measurements, which is the first of its kind to the authors knowledge.

6.2 Indentation Properties from Spherical Indentation Stress Strain Curves

These protocols are based on the relationships initially established by the elastic, frictionless, contact between two isotropic, homogenous bodies with quadratic surfaces by Hertz Theory [17].

$$\mathcal{P} = \frac{4}{3} E^* R_{eff}^{\frac{1}{2}} h_e^{\frac{3}{2}} \tag{6.1}$$

$$a = \sqrt{R_{eff} h_e} \tag{6.2}$$

where $\mathcal{P}$ is the indentation load due to the elastic indentation displacement, h_e. In Equation (6.1) R_{eff} denotes the effective radius of the indenter-sample system, and E^* is the effective indentation modulus. Although the measured E^* generally reflects the effective indentation modulus of the indenter-sample system, one can account for the elastic deformation in the indenter itself and recover the indentation modulus of the sample alone [17]. The corresponding distance to the edge of contact between the indenter and the sample surfaces is given by contact radius, a, shown in Equation (6.2). In order to transform indentation load-displacement data into meaningful indentation stress-strain curves, suitable measures of indentation stress, σ_{ind}, and indentation strain, ε_{ind}, have previously been developed [18].

$$\sigma_{ind} = \frac{\mathcal{P}}{\pi a^2} \tag{6.3}$$

$$\varepsilon_{ind} = \frac{4}{3\pi}\frac{h^*}{a} \tag{6.4}$$

These measures are meant to represent effective volume-averaged quantities in the primary deformation zones underneath the indenter. We note h^* generally reflects the total indentation depth of the entire indenter-sample system and, similar to E^*, one can account for the effect due to the indenter in order to recover the indentation depth due solely into the sample. In the treatment presented here, it will be assumed that such corrections have been made, i.e., E^* and h^* denotes the indentation modulus and depth of the sample respectively.

The main impediment in the determination of indentation stress and strain measures is that direct measurement of the contact radius, a, is often difficult. We note, when simulating the indentation experiment the computation of a is best accomplished via elastic unloading segments [16]. Each unloading segment corresponds to a single data point for indentation stress-strain measurements. Therefore, the establishment of an indentation stress-strain curve corresponds to the simulation of a loading segment followed by multiple unloading segments. This process leads to a significant computational expense when simulating a full indentation stress-strain curve.

6.2.1 Experimental Indentation Property Data

Although the above protocols were initially developed considering the contact between an indenter and isotropic material system, subsequent work has extended such protocols to the extraction of meaningful indentation stress strain curves for anisotropic material systems [1,4,13,15]. In polycrystalline materials, the indentation stress strain curves measured

within single grains of a particular thermodynamic phase have been found to be a function of the direction of indentation relative to the local crystallographic orientation. In recent work, spherical indentation protocols were used to successfully establish the indentation stress-strain response in α-grains at several crystallographic orientations for a wide array of Ti-alloys. We note, the crystallographic orientation of a grain with the sample frame can be represented by a set of Bunge Euler angles $\boldsymbol{g} = \{\varphi_1, \phi, \varphi_2\}$. For each experimental indent the indentation modulus, E^*, and indentation yield, Y^*, with their corresponding orientation, $\boldsymbol{g}$, was established in an unpublished study by Millan and Mohan et. al. We note these indentation properties are used in this study for the estimation of the intrinsic crystal level elastic-plastic properties. The alloys which are considered in this study and the corresponding measured indentation properties versus the angle between the crystal c-axis and the direction of indentation, ϕ (referred to as the declination angle), are summarized in Figure 6.1.

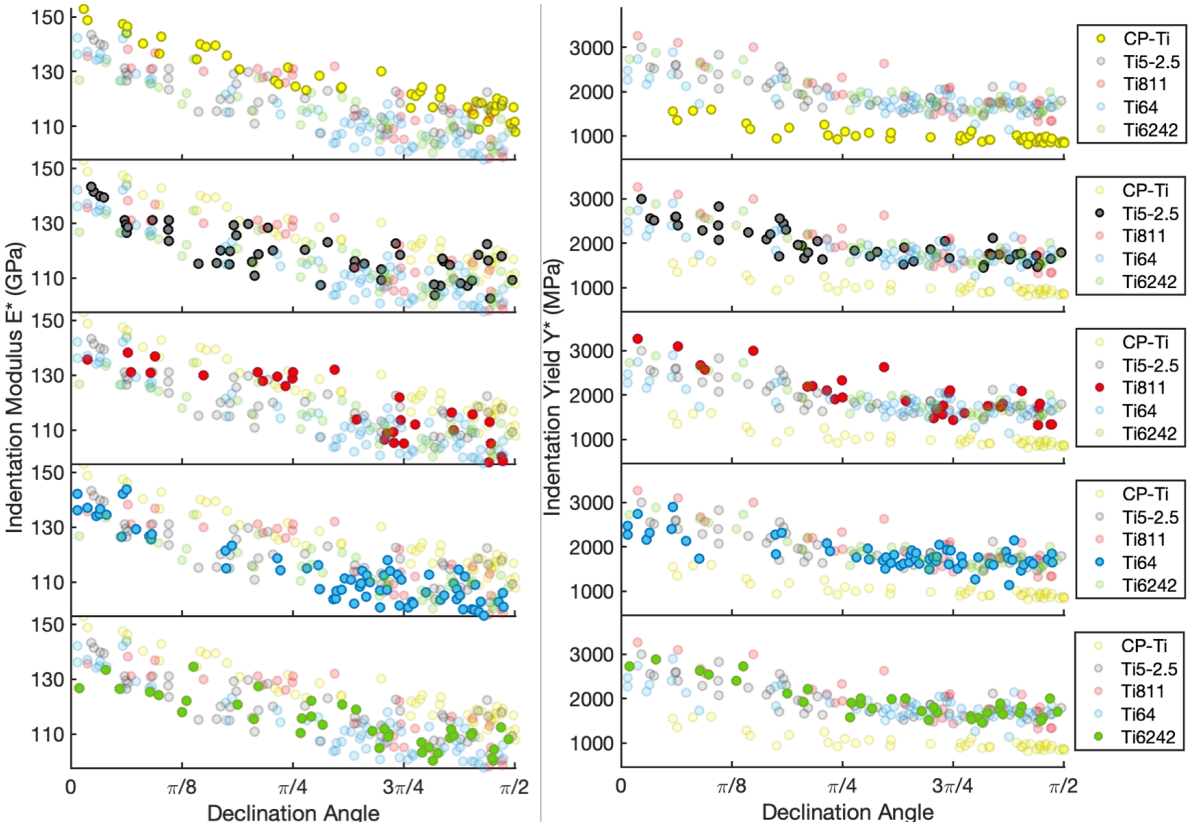

Figure 6.1. Summary of Ti-alloys which the indentation moduli, $\boldsymbol{E}^*$, and indentation yield values, $\boldsymbol{Y}^*$, versus the declination angle with respect to the direction of indentation and c-axis have been determined via indents within multiple $\boldsymbol{\alpha}$-grains of corresponding polycrystalline samples.

6.3 Crystal Plasticity Finite Element Simulation of the Spherical Indentation Experiment

6.3.1 Crystal Plasticity Material Model

In order to calibrate underlying single crystal material properties using experimental spherical indentation measurements, physics-based models of the indentation experiment which are sensitive to changes in the single crystal material parameters of interest (i.e. slip resistances) are needed. In order to implement such models, a suitable description of the local deformation at the crystal level is adopted from previous works [19,20]. The local

deformation at the crystal level is considered through the determination of the local plastic velocity gradient, $\boldsymbol{L}^P$, which is computed from the rates of shear deformation across multiple crystallographic slip systems [21]. $\boldsymbol{L}^P$ is related to the shearing rate across all α slip systems as

$$\boldsymbol{L}^P = \sum_\alpha \dot{\gamma}^\alpha \boldsymbol{S}_0^\alpha, \qquad \boldsymbol{S}_0^\alpha = \boldsymbol{m}^\alpha \otimes \boldsymbol{n}^\alpha \tag{6.5}$$

where $\boldsymbol{S}_0^\alpha$ is the Schmid tensor computed using the slip plane normal, $\boldsymbol{n}^\alpha$, and slip direction $\boldsymbol{m}^\alpha$.

The visco-plastic power law commonly used to model the slip activity on slip system α due to an imposed resolved shear stress τ^α is given by

$$\dot{\gamma}^\alpha = \dot{\gamma}_0 \left| \frac{\tau^\alpha}{s^\alpha} \right|^{\frac{1}{m}} sign(\tau^\alpha) \tag{6.6}$$

Where $\dot{\gamma}_0$ is a reference shear rate, m is the rate sensitivity parameter and s^α is the resistance to slip of the α system. We note the slip resistances, s^α, are usually taken to evolve through time in accordance with a hardening law which takes into account the shear rates across all slip systems. In this work, only initial values of slip resistance are of interest, and as such, values of s^α are treated as constant. The initial slip resistance parameters and corresponding slip systems considered in this work are shown in Table 6.1.

Table 6.1. Slip systems and corresponding initial slip resistance parameters considered in the crystal plasticity material model.

Slip System	Initial Slip Parameter	Slip Elements
$Prismatic$	s_{pr}	$\{1\ \bar{1}\ 0\ 1\}$ <1 1 $\bar{2}$ 0>
$Basal$	s_{ba}	$\{0\ 0\ 0\ 1\}$ <1 1 $\bar{2}$ 0>
$Pyrimidal < a >$	s_{pyr-a}	$\{1\ \bar{1}\ 0\ 1\}$ <1 1 $\bar{2}$ 0>
$Pyrimidal\ < c + a >$	s_{pyr-ca}	$\{1\ \bar{1}\ 0\ 1\}$ <1 1 $\bar{2}$ 3>

6.3.2 FE simulation of Spherical Indentation Experiment

The Crystal plasticity material model outlined above is incorporated into a user-material subroutine (UMAT) in the general purpose FE program ABAQUS in order to simulate the spherical nanoindentation test [19]. In prior work [10], an FE model was developed to estimate the nanoindentation yield strength. This FE model consisted of: (i) a deformable sample with the crystal plasticity material model attributed to it, and (ii) a rigid hemi-spherical indenter above the sample. Eight-noded, three-dimensional, continuum elements (C3D8 in ABAQUS) were used to mesh the deformable sample. The zone directly under the indenter (also called the primary indentation zone) should have a sufficient mesh density in order to capture the elastic-plastic transition accurately. In order to mitigate free surface effects, the FE discretization of the sample was designed such that the mesh density became progressively coarser toward the boundaries of the sample. We note, a large domain size was found to be necessary in order to accurately extract simulated spherical indentation stress-strain curves, and the resulting FE mesh consisted of 126560 elements.

While the aforementioned meshing scheme was effectively used to establish the slip resistances of BCC Fe-3%Si alloy, a significant computational challenge is presented in

this work due to: (i) the plastic anisotropy exhibited in HCP metals (for instance, between the Pyramidal-<c+a> slip system and the Prismatic slip system) and alloys is expected to further decrease the computational efficiency of the simulations and (ii) the exploration of fairly large parameter space (delineated by the bounds of the slip resistances chosen for the simulations) required to generate the dataset is expected to drastically increase the number of simulations that need to be performed. Therefore, there exists a need to build a more computationally efficient FE model. In contrast to coarsening the mesh of regions further from the primary zone of indentation in order to mitigate free surface effects, prior works [6,125,126] have instead meshed the region outside the primary indentation zone using infinite elements in order to simulate the effect of an infinite elastic domain in the region far from the indenter tip. Infinite elements rely on a specific decay function defined toward the direction of the free surface allowing the emulation of infinite domains [56]. Such treatment has the potential to allow for the drastic reduction of the number elements needed to mitigate free surface effects. For this study, the zone directly under the indenter which contains the primary zone of indentation is meshed using continuum finite element (C3D8 in this case), while the zones outside the primary indentation zone have been assigned eight-noded hexahedral infinite elements (type CIN3D8 in ABAQUS). The new FE model is shown Figure 6.2 (c). The aforementioned discretization procedure allows us to drastically reduce the number of elements in the deformable sample from 126560 elements to 13500. With this meshing scheme, the element size in the primary indentation zone is $0.05\mu m \times 0.05\mu m \times 0.075\mu m$, which represents an aspect ratio of 1.5.

In order to simulate the indentation stress-strain experiment, frictionless, surface-to surface contact between the deformable sample and rigid indenter with a radius of $10\mu m$ was used.

The displacement of the indenter is controlled in the z-direction. Multiple loading and elastic unloading segments were produced in order to compute the radius of contact shown in Eqn. (6.2) in accordance with the aforementioned indentation stress-strain protocols. Throughout the entire loading process, the slip activity is limited to the primary indentation zone in the FE simulation. We have validated the infinite elements incorporated FE model by comparing that the stress strain curves obtained from the FE simulation against the stress-strain curves reported in Patel et. al. [16] for an isotropic elastic-perfectly plastic sample (with the same material properties), as shown in Figure 6.2 (a). We note that the equivalent plastic strain contours (as indicated by "PEEQ") are restricted to the primary indentation zone.

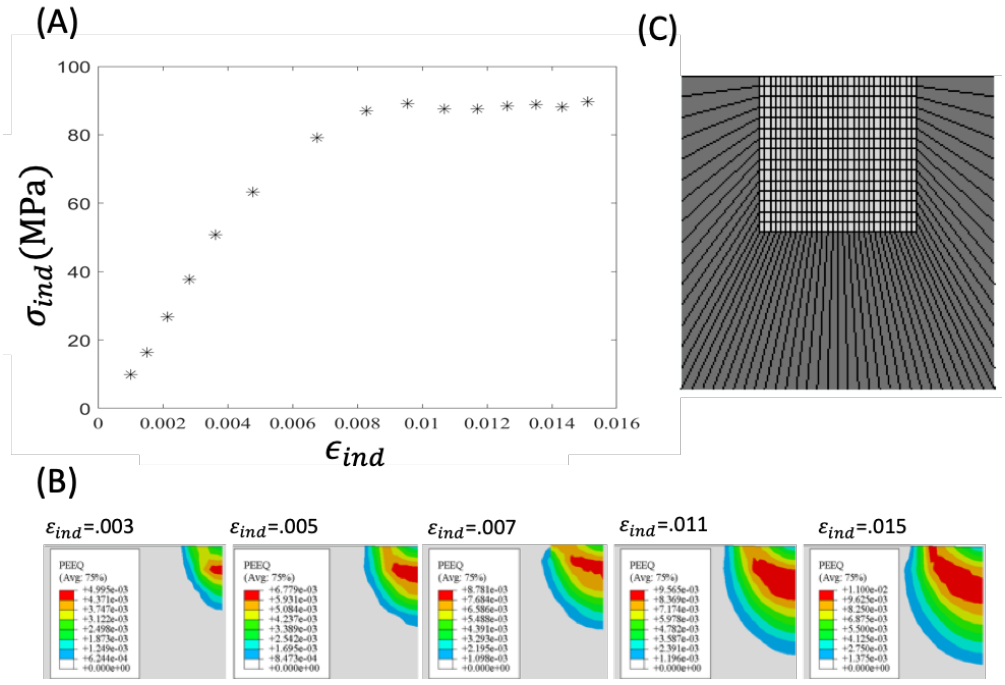

Figure 6.2. (a)Indentation stress-strain curve obtained for an elastic-perfectly plastic material from a FE simulation meshed with infinite elements in the primary indentation zone (b)illustration of the FE mesh used in this study with the light grey representing the continuum (C3D8) elements and the dark grey representing the infinite (CIN3D8) elements and (c)Evolution of Equivalent Plastic Strain contours (denoted as PEEQ) within the primary indentation zone for the isotropic elastic-perfectly plastic case, indicating the localized plastic deformation

6.4 Extraction of Single Crystal Level Properties via Spherical Indentations

6.4.1 Bayesian Framework for Extraction of Crystal Level Properties

The Bayesian framework employed here is adopted from prior work [44], and is briefly reviewed next. In the following let $\boldsymbol{\psi}$ be a set of crystal level intrinsic material properties, P^* be an experimentally measured indentation property (e.g. indentation modulus *or* indentation yield) which are highly correlated to the underlying intrinsic properties (e.g. single crystal elastic constants *or* initial slip resistances). In this approach, the measured indentation property is modeled as

$$P^* = P^*_{sim}(\boldsymbol{\psi}, \boldsymbol{g}) + \epsilon \tag{6.7}$$

where $P^*_{sim}(\boldsymbol{\psi}, \boldsymbol{g})$ denotes the FE-simulated indentation property at the crystallographic orientation $\boldsymbol{g}$, corresponding to a set of intrinsic material properties, $\boldsymbol{\psi}$, and $\epsilon \sim \mathcal{N}(0, \lambda)$ denotes a stochastic noise term. It is implicitly assumed here that the FE simulated $P^*_{sim}(\boldsymbol{\psi}, \boldsymbol{g})$ exhibits negligible variance. Let $\{\boldsymbol{P}^*_{exp}, \boldsymbol{G}_{exp}\}$ denote the set of experimental indentation properties, $\boldsymbol{P}^*_{exp}$, measured at the corresponding crystallographic orientations, $\boldsymbol{G}_{exp}$. The likelihood for n experimental measurements (denoted $\{\boldsymbol{P}^*_{exp}, \boldsymbol{G}_{exp}\}$) is expressed as

$$p\left(\boldsymbol{P}^*_{exp} \middle| \boldsymbol{\psi}, \boldsymbol{G}_{exp}, \lambda\right) = \prod_i^n \frac{1}{\sqrt{2\pi\lambda}} exp\left\{\frac{-(P^*_i - P^*_{sim}(\boldsymbol{\psi}, \boldsymbol{g}_i))^2}{2\lambda}\right\} \tag{6.8}$$

where P^*_i denotes the experimental indentation property measured at the i-th orientation and λ is the homoscedastic variance exhibited by the indentation modulus across the

orientation parameter space. Inference of the intrinsic material properties, $\boldsymbol{\psi}$, for the observed experimental data can be expressed by Bayes rule:

$$p\left(\boldsymbol{\psi}\middle|\boldsymbol{P}_{exp}^{*},\boldsymbol{G}_{exp},\lambda\right)\propto p\left(\boldsymbol{P}_{exp}^{*}\middle|\boldsymbol{\psi},\boldsymbol{G}_{exp},\lambda\right)p(\boldsymbol{\psi}) \tag{6.9}$$

Considering a uniform prior for $p(\boldsymbol{\psi})$ along with the likelihood function shown in Eqn. (6.8) allows for the application of MCMC methods for sampling the posterior distribution on single crystal properties [45]. MCMC algorithms seek to generate a sequence, known as a Markov Chain, which converges to a target posterior distribution by accepting/rejecting a large number of proposed transitions across a finite parameter space based on an acceptance probability. Specifically, the Single Component Metropolis Hastings (SCMH) algorithm is adopted in this work to generate transitions across the multivariate parameter space of intrinsic material parameters [35]. We note in previous studies multiple indents were available per grain orientation allowing a direct estimation of the variance. In this study, such a luxury is not available since only a single indent was available per grain orientation. This means for a given set of intrinsic material properties, $\boldsymbol{\psi}$, the variance λ associated with the likelihood in Eqn. (6.8) is unknown. One common way to approach this problem is to adjust the MCMC algorithm in order to generate samples of $\boldsymbol{\psi}$ and λ given the available data $\{\boldsymbol{P}_{exp}^{*},\boldsymbol{G}_{exp}\}$. Subsequently, Eqn. (6.9) is modified as

$$p\left(\boldsymbol{\psi},\lambda\middle|\boldsymbol{P}_{exp}^{*},\boldsymbol{G}_{exp}\right)\propto p\left(\boldsymbol{P}_{exp}^{*}\middle|\boldsymbol{\psi},\boldsymbol{G}_{exp},\lambda\right)p(\lambda|\boldsymbol{\psi},\boldsymbol{P}_{exp}^{*},\boldsymbol{G}_{exp})p(\boldsymbol{\psi}) \tag{6.10}$$

Where under the consideration of a normally distributed likelihood, the distribution of λ is commonly taken to be the inverse chi squared distribution [45,127,128].

$$p(\lambda|\boldsymbol{P}^*_{exp}, \boldsymbol{\psi}, \boldsymbol{G}_{exp}) \propto \ inv\text{-}\chi^2(\lambda|\hat{\lambda}\left(\boldsymbol{P}^*_{exp}, \boldsymbol{\psi}, \boldsymbol{G}_{exp}\right), n) \tag{6.11}$$

In Eqn. (6.11), $\hat{\lambda}\left(\boldsymbol{P}^*_{exp}, \boldsymbol{\psi}, \boldsymbol{G}_{exp}\right)$ denotes the best estimate of variance for the current parameters, $\boldsymbol{\psi}$, using the available data, i.e. $\hat{\lambda} = \frac{1}{n}\sum_i^n\left(P_i^* - P^*_{sim}(\boldsymbol{\psi}, \boldsymbol{g}_i)\right)^2$, and n denotes the number of available experiments. For a given transition across the parameter space the inverse chi squared distribution is fully determined and a candidate value for λ can be readily sampled. Generation of samples from the inverse chi-squared distribution can be accomplished using readily available software [54]. The acceptance probability of a proposed transition of $\boldsymbol{\psi}$ in the Monte Carlo algorithm is than solely determined by the ratio between candidate and current values evaluated by Eqn. (6.10). In practice, these methods often require tens of thousands of evaluations of the likelihood function to ensure convergence [37]. In this work, 50,000 samples are drawn via SCMH in order to generate a Markov Chain. Due to the probabilistic nature of MCMC, it is desirable to run the algorithm multiple times, randomly selecting initial starting points to ensure that independently sampled Markov Chains converge to similar distributions. The high computational costs associated with the execution of the FE models of indentation make it impractical to use the FE indentation models directly in the computations described above. The only practical approach for addressing this challenge is to establish a reduced-order model.

6.4.2 Reduced Order Models for prediction of Indentation Properties

In order to efficiently evaluate the likelihood function, suitable reduced order models which take into account single crystal material properties and intrinsic single crystal properties as

input and output indentation properties must be established. The indentation properties which reduced order models are established are dictated by the available experimental indentation properties measured across the orientation space. This corresponds to a reduced order model for the simulated indentation modulus, $E^*_{sim}(\boldsymbol{c}, \boldsymbol{g})$, where $\boldsymbol{c} = \{C_{11}, C_{12}, C_{44}, C_{33}, C_{13}\}$ denotes the single crystal elastic constants, as well as for the simulated indentation yield, $Y^*_{sim}(\boldsymbol{s}, \mathbf{g})$, where $\boldsymbol{s} = \{s_{pr}, s_{ba}, s_{pry-a}, s_{pyr-ca}\}$ denotes the initial slip resistances. We note, since any rotation about the sample normal does not affect the measured indentation properties, it can be seen that, in general, the indentation properties are independent of φ_1, i.e. $P^*_{sim}(\boldsymbol{\psi}, \mathbf{g}) = P^*_{sim}(\boldsymbol{\psi}, \phi, \varphi_2)$ [5,22].

Recent work has successfully established a reduced-order model that captures the dependence of indentation modulus on the crystal orientation of the indented grain and an arbitrary set of single crystal elastic constants applicable to a wide range of hcp metals [44,48]. Since hcp metals exhibit a transversely isotropic elastic response the measured indentation modulus is independent of φ_2 (i.e., a rotation about the c-axis also does not influence the measured elastic indentation response). Consequently, the aforementioned work established a model only considering the declination angle, $E^*_{sim}(\boldsymbol{c}, \phi)$, as shown below

$$E^*_{sim} \approx \hat{E}^*(\boldsymbol{c}, \phi) = \sum_{l=0}^{L} \sum_{\boldsymbol{q}}^{\boldsymbol{Q}} A^{\boldsymbol{lq}} P^l(cos\ (\phi)) \tilde{P}^{\boldsymbol{q}}(\bar{\boldsymbol{c}}) \tag{6.12}$$

$$\bar{c}_j = \frac{2c_j - c_j^{min} - c_j^{max}}{c_j^{max} - c_j^{min}}$$

where $\tilde{P}^{\mathbf{q}}(\bar{\mathbf{c}})$ denotes a multivariate Legendre polynomial product basis and $P^{l}(\cos\phi)$ denotes the Legendre polynomials expanded over the relevant orientation space. In other words, one can express $\tilde{P}^{\boldsymbol{q}}(\bar{\mathbf{c}}) = P^{q_1}(\bar{c}_{11})P^{q_2}(\bar{c}_{12})P^{q_3}(\bar{c}_{44})P^{q_4}(\bar{c}_{33})P^{q_5}(\bar{c}_{13})$, where $\boldsymbol{q} = (q_1, q_2, q_3, q_4, q_5)$ forms a multi-index array, each element of which is a nonnegative integer allowed to vary from 0 to the selected maximum degree, Q, i.e., $q_j \in [0, Q]$. We note, $\boldsymbol{Q}$ and L denotes the truncation levels for the for the formulation in Eqn. (6.12). For the proper application of the Legendre Polynomial basis, each of the elastic constants are rescaled over their respective ranges [74], where c_j^{max} and c_j^{min} are the maximum and minimum values of the j-th elastic constant. The degree of the Legendre polynomials expanded about the orientation space were selected to be strictly even to fully reflect the symmetries present in the transversely isotropic material system [22]. The above reduced order model established in previous works [44] is used here for the extraction of single crystal elastic constants for the collection of alloys in Figure 6.1.

A reduced order model has yet to be established for hcp metals which predicts the indentation yield for a given set of slip resistances, and corresponding orientation, $Y^*(\boldsymbol{s}, \phi, \varphi_2)$. Previous work involving the extraction of slip resistance values using indentation measurements into a collection of grains within a cubic Fe-3%Si polycrystalline sample found success in establishing a reduced order model by using Fourier basis obtained by compounding symmetrized surface spherical harmonics (to represent functions over the orientation space) with Legendre polynomials (to represent functions over the ranges of the values for the single crystal properties) [74]. The advantage of this representation was the ability to capture the underlying crystal symmetries exhibited by a given material system. The aforementioned work found extraction efforts were made

much more robust when formulated using normalized indentation yield values [10]. Extending these ideas, the reduced order model for the simulated indentation yield normalized by the prismatic slip, $\frac{Y^*_{sim}(\boldsymbol{r},\phi,\varphi_2)}{s_{pr}}$, takes the form

$$\frac{Y^*_{sim}}{s_{pr}} \approx \bar{Y}^*(\boldsymbol{r},\phi,\varphi_2) = \sum_{l=0}^{\tilde{L}} \sum_{m=1}^{\tilde{M}(l)} \sum_{\boldsymbol{\eta}}^{\tilde{\boldsymbol{Q}}} B_l^{m\boldsymbol{\eta}} K_l^m(\phi,\varphi_2) \tilde{P}^{\boldsymbol{\eta}}(\bar{\boldsymbol{r}}) \tag{6.13}$$

$$\bar{r}_j = \frac{2r_j - r_j^{min} - r_j^{max}}{r_j^{max} - r_j^{min}},\ \boldsymbol{r} = \left\{\frac{s_{ba}}{s_{pr}}, \frac{s_{pyr-a}}{s_{pr}}, \frac{s_{pyr-ca}}{s_{pr}}\right\}$$

where $K_l^m(\phi,\varphi_2)$ denote the symmetrized surface spherical harmonics expanded over the relevant orientation space [73], and $\tilde{P}^{\boldsymbol{\eta}}(\bar{\mathbf{r}})$ denotes a multivariate Legendre polynomial product basis. We note $\boldsymbol{\eta} = (\eta_1, \eta_2, \eta_3)$ forms a multi-index array, where each element of which is a nonnegative integer allowed to vary from 0 to a selected maximum degree, $\tilde{\boldsymbol{Q}}$, i.e., $\eta_j \in [0, \tilde{Q}]$. In Eqn. (6.13) m and l indexes the spherical harmonic basis where $\tilde{M}(l)$ enumerates the spherical harmonics that implicitly reflect the symmetries of the hcp system. With the model form in place, the remaining issue involves the establishment of the model coefficients, $\boldsymbol{B}$. In this work, the model coefficients, $\boldsymbol{B}$, are established using a sequential model building process deployed successfully in previous works [44]. In previous works, the calibration of Fourier coefficients to reduced order models for indentation properties was accomplished via Bayesian Linear Regression (BLR). The usage of BLR in this context provides a valuable quantification of uncertainty associated with the predictions from the reduced-order model [30]. In order to establish the reduced-order model, a database of finite element simulations covering the relevant input parameter

space is necessary. The quantification of uncertainty provided by BLR enables the deployment of sequential strategies to build a simulated database by focusing on areas of high predictive uncertainty. Simulations can be continually performed until sufficient performance of the reduced-order model is achieved, as determined by various error metrics. The implementation of this strategy in previous work has shown a significant reduction in the number of simulations necessary to establish a high fidelity reduced-order model in comparison with traditional regression approaches [44].

6.5 Results

6.5.1 Estimation of Single Crystal Elastic Constants

In the first application of the Bayesian framework outlined in Section 6.4, the initial focus is the extraction of single crystal elastic constants $\boldsymbol{c} = \{C_{11}, C_{12}, C_{44}, C_{33}, C_{13}\}$ from the collection of Ti samples. We recall, in order to sample from the distribution of single crystal elastic constants the main requirement is the establishment of the likelihood in Eqn. (6.10). To efficiently evaluate the likelihood function, a reduced order model can be built using a database of suitable finite element simulations of the spherical indentation experiment. The reduced order model, shown in Eqn. (6.12), which predicts the indentation modulus for an arbitrary orientation and given set of elastic constants has been built in previous works and is adopted here for extraction efforts [44]. The aforementioned model uses truncation levels Q=2, L=4 and was built using a database of 2200 finite element simulations within the bounds $80 \leq C_{11} \leq 240$ GPa, $40 \leq C_{12} \leq 120$ GPa, $30 \leq C_{44} \leq 90$ GPa, $70 \leq C_{33} \leq 210$ GPa, and $30 \leq C_{13} \leq 90$ GPa. Given the elastic transversely isotropic behavior of

hcp materials, only the orientation space defined by $0 \leq \phi \leq \frac{\pi}{2}$ was considered in the aforementioned model building process.

6.5.1.1 MCMC Sampling of Single Crystal Elastic Constants

Given the availability of a reduced order model, and the available experiments shown in Figure 6.1, the likelihood function can be established. The corresponding prior distribution of the elastic constants was taken to be a uniform distribution defined by the bounds of the FE simulated database. Multivariate MCMC chains of single crystal elastic constants were independently sampled for each alloy in Figure 6.1 and the resulting distributions are tabulated and summarized in Figure 6.3.

The resulting distributions are sharpest with respect to estimates for C_{44}, followed by C_{33} and C_{11}. Estimates for C_{12} and C_{13} show a significant amount of uncertainty relative to the other estimates. The relatively high uncertainty exhibited by C_{12} and C_{13} is indicative of a smaller influence of these elastic parameters on the indentation modulus (i.e. sensitivity) across the orientation space. We note, the mean estimates of single crystal elastic constants for CP-Ti are within one standard deviation of previous estimates which used the same reduced order model, but a separately collected experimental dataset for extraction efforts [1,44]. In order to better diagnose the uncertainties apparent in the extraction effort, the predictions of indentation modulus across the orientation space using the sampled MCMC chains are shown in Figure 6.4.

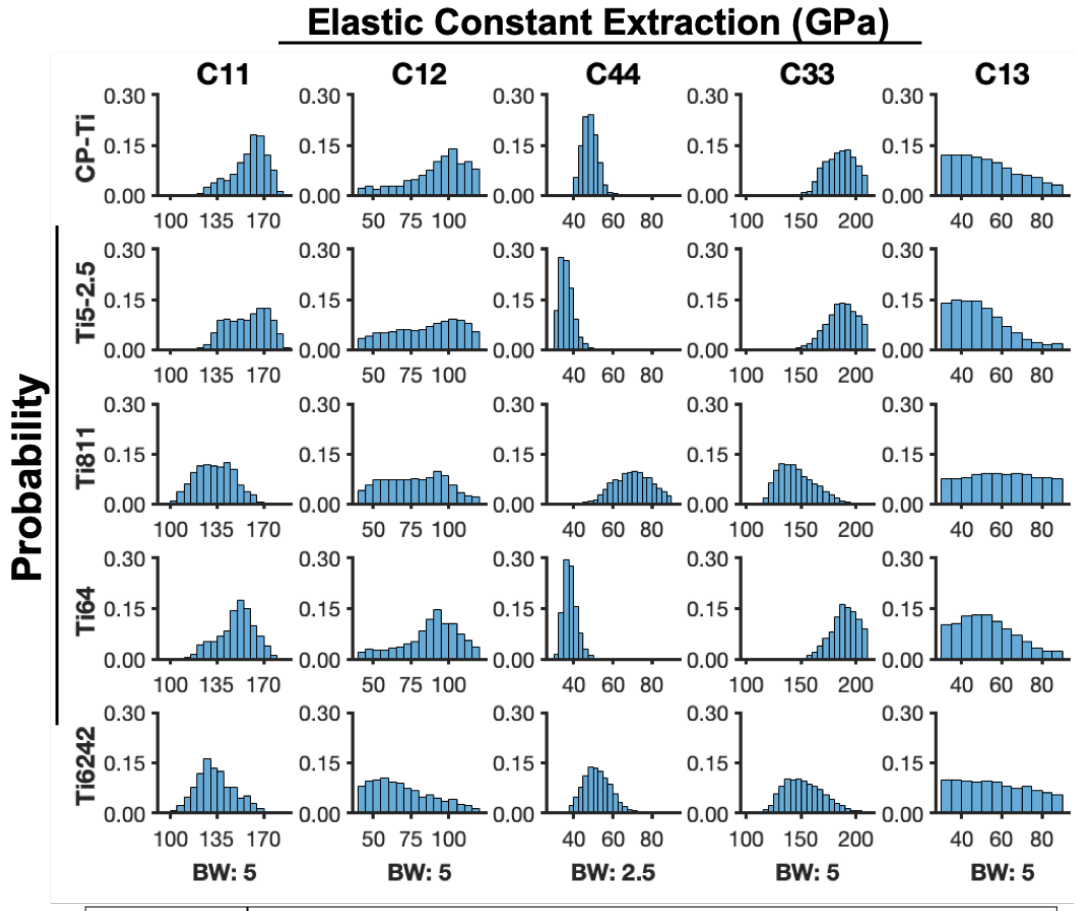

	C11 (GPa)	C12 (GPa)	C44 (GPa)	C33 (GPa)	C13 (GPa)
CP-Ti	159 ± 13	92 ± 19	48 ± 4	185 ± 13	53 ± 16
Ti5-2.5	158 ± 15	85 ± 22	37 ± 4	186 ± 13	49 ± 13
Ti811	133 ± 14	77 ± 20	70 ± 9	146 ± 17	60 ± 17
Ti64	150 ± 14	88 ± 18	38 ± 3	189 ± 12	53 ± 14
Ti6242	134 ± 14	70 ± 20	52 ± 7	153 ± 19	57 ± 17

Figure 6.3. Top: Distributions of single crystal elastic constants extracted for alloys considered in this work. BW denotes the fixed bin width for the distributions in a given column. Bottom: The mean and corresponding standard deviation of the extracted initial slip resistances are shown.

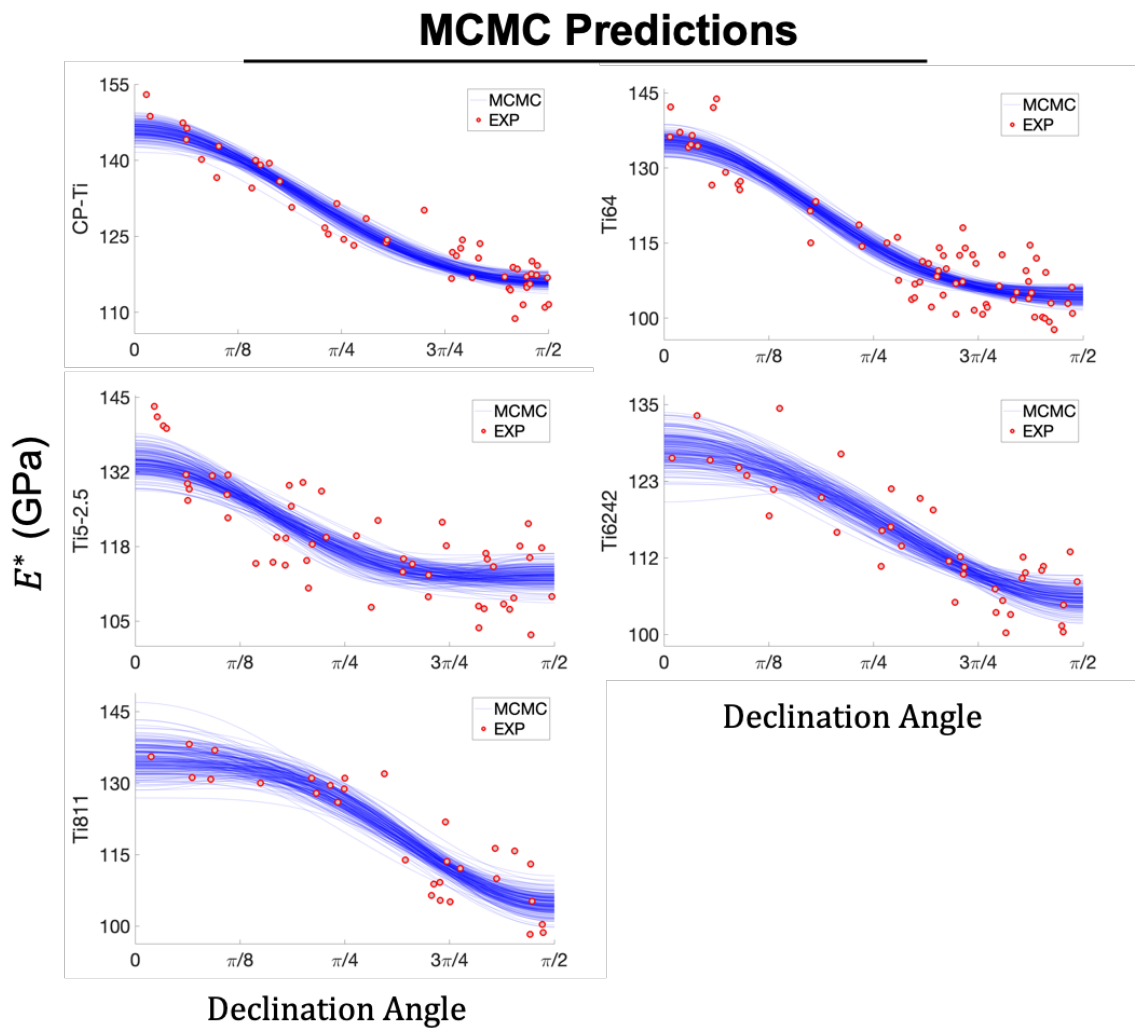

Figure 6.4. Predictions of Indentation Modulus versus declination angle using sampled MCMC chains and reduced order model established in previous works.

The tightest predictions across the orientation space correspond to the MCMC chains sampled from the CP-Ti and Ti64 samples. The distributions for C_{11}, C_{33}, and C_{12} of single crystal elastic constants extracted for CP-Ti and Ti-64 are in general slightly sharper compared to the respective distributions extracted for other alloys. We note, Ti64 had the most available experimental measurements (67), followed by Ti5-2.5 (52), CP-Ti (50), Ti6242 (38) and Ti811 (31). MCMC predictions and the underlying distributions of C_{11} and C_{12} for CP-Ti are noticeably sharper than those found from Ti5-2.5 even though

roughly the same number of experimental indents were available. These observations demonstrate that, intuitively, the more precision in the experimental measurements, the higher precision in the extracted distributions of single crystal elastic constants.

6.5.2 Estimation of Initial Slip Resistances

Attention is now turned to the extraction of initial slip resistance values from the alloys considered in Figure 6.1 for the associated families of slip systems in Table 6.1. In order to evaluate the likelihood function described in Eqn. (6.10), a high fidelity reduced order model covering a suitable parameter space must be established. The first step in this process is the determination of the bounds of the parameter space of crystal plasticity finite element simulations for the 3-dimensional space of slip ratios, $\boldsymbol{r}$, and 2-dimensional space of relevant Bunge Euler angles, $\{\phi, \varphi_2\}$. The bounds of the ratios were chosen to be $\{0.75 \leq \frac{s_{ba}}{s_{pr}} \leq 2.0\,, 2.0 \leq \frac{s_{pyr-a}}{s_{pr}} \leq 4.5\,, 2.5 \leq \frac{s_{pyr-ca}}{s_{pr}} \leq 6.5\}$, based on activity of slip resistances reported across literature for the alpha phase of Ti-alloys, while the bounds of the orientation parameters were chosen to be $\{0 < \phi < \frac{\pi}{2}, 0 \leq \varphi_2 \leq \frac{\pi}{3}\}$ which defines relevant the fundamental zone for HCP materials [129]. A database of indentation yield values with corresponding inputs $\{\boldsymbol{r}, \phi, \varphi_2\}$ and prismatic slip s_{pr} was generated via CPFEM indentation simulations outlined in Section (6.3.2). We note in the formulation shown by Eqn. (6.13), the prismatic slip, s_{pr} is essentially treated as a reference slip and is set to $s_{pr} = 5$ MPa. The remaining inputs considered for the database were determined in two steps, the first step is an initial database followed by a sequential design process adopted from previous works [44].

6.5.2.1 Reduced Order Model for Indentation Yield

Previous efforts in cubic metals found a large number of SSH basis functions were necessary in order to capture the dependence of normalized Indentation Yield on orientation [22]. We note the previous study involving cubic materials considered a single slip parameter, and effectively assumed a linear relationship was sufficient in capturing changes in indentation yield to changes in the slip resistance value for a given orientation. Extending these ideas only the linear terms about the associated slip ratios, i.e. $\tilde{Q}$=1, were initially considered and larger truncation levels for SSH coefficients were prioritized. Initially, 92 sets of inputs were screened from 5-dimensional Max Pro Latin Hypercube Design (LHD) of 1000 inputs based on space filling properites [104], where the number of simulations were chosen to be slightly larger than the number of Fourier coefficients (88) corresponding to truncation levels of $\tilde{Q} = 1, \tilde{L} = 10$. Following the determination of the initial database, a sequential design process adopted from previous works was used to select inputs to additional simulations from the remaining 902 inputs. Truncation levels, $\tilde{Q}$=1 and $\tilde{L}$=14 (corresponding to 160 Fourier coefficients) were found sufficient in establishing the reduced order model. The predictive performance of the reduced order model using a database of 312 CPFEM indentation simulations is demonstrated in Figure 6.5.

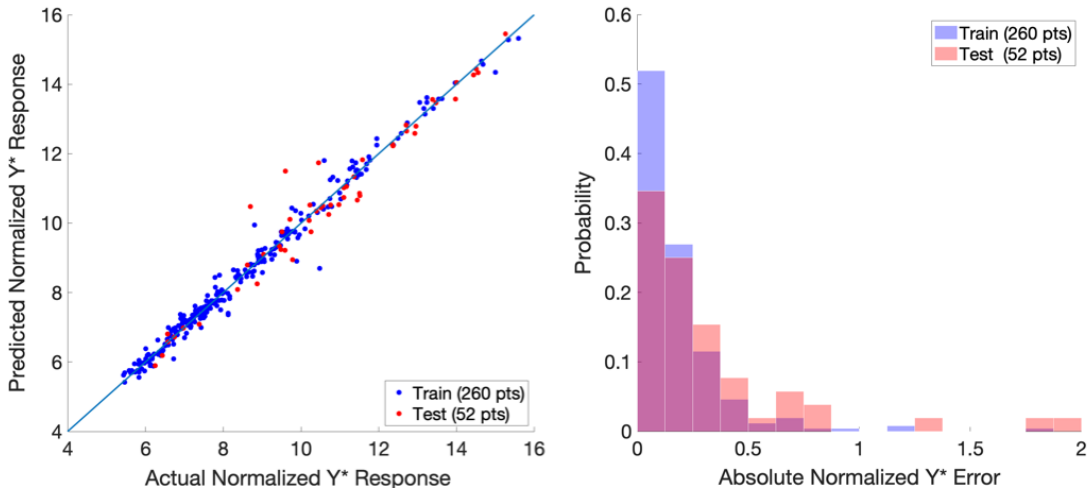

Figure 6.5. Left: Predictive performance of reduced order model for normalized indentation yield. Right: Corresponding Test and Train histograms of absolute error for predictions. We note the normalized values correspond to a unitless factor which scales according to the prismatic slip value.

The mean training error and corresponding standard deviation are 0.18 ± 0.20 while the mean test error and corresponding standard deviation are 0.32 ± 0.38. Errors which fall above 0.8 corresponded to points which were highly anisotropic and located toward the bounds of the considered parameter space of slip resistance ratios. Reduced order models with truncation levels below $\tilde{L}$=14 often exhibited comparable mean absolute testing and training errors, however the lower the truncation level the less anisotropy the model could accommodate, and predictions closer to the bounds of the parameter space worsened. For example, using the same testing and training dataset, a reduced order model with a truncation level, $\tilde{Q} = 1, \tilde{L}$=10, 5% of prediction errors fall between 0.8 and 2.0. We note with the chosen truncation level, 2.5% of total prediction errors fall between 0.8 and 2.0.

6.5.2.2 MCMC Sampling of Initial Slip Resistance Parameters

With a reduced order model in place attention is turned to the extraction of initial slip resistances, $\boldsymbol{s} = \{s_{pr}, s_{ba}, s_{pyr-a}, s_{pyr-ca}\}$. The likelihood shown in Eqn. (6.10) can be

evaluated for a given set of slip resistances using the experimental indentation yield values measured across the orientation space for a particular alloy shown in Figure 6.1. We note, a major advantage to the formulation of the reduced order model shown in Eqn. (6.13)(6.10) in accordance to normalized indentation yield and slip ratios is that it is unnecessary to directly bound the parameter space of slip resistances during the extraction process. Thus, a broad uniform distribution which only enforces the slip resistances to be strictly positive was used. With the likelihood(s) and prior(s) established, multivariate MCMC chains of slip resistances were independently sampled for each alloy and the resulting distributions are tabulated and summarized in Figure 6.6. The differences between the individual initial slip resistance parameters compared across the Ti-alloys is apparent in Figure 6.6. We note the relative uncertainty of the estimates can be ranked, from lowest to highest as prismatic with the lowest relative uncertainty, basal and pyramidal <c+a> exhibiting slightly more relative uncertainty and pyramidal <a> exhibiting the highest relative uncertainty. This ranking can be seen as reflective of the amount of slip activity for the slip systems across all the grain orientations experimentally indented. Similar to the extracted distribution of elastic constants, the MCMC predictions for indentation yield across the orientation space can assist in further analyzing the extracted distributions of initial slip resistances. The mean predictions of indentation yield from the MCMC chains across the orientation space for a given alloy as compared to the experimental data available are shown in inverse pole figure shown in Figure 6.7. The associated uncertainty of the mean predictions from the MCMC chains across the orientation space and the corresponding orientations probed experimentally are shown in the inverse pole figure in Figure 6.8. The mean predicted indentation yield contours are consistent with the

experimentally reported indentation yield values. The measure of uncertainty provided by the MCMC prediction can provide guidance to where addition experiments may be performed in order to sharpen the distributions of slip resistances. For instance, all IPF contours show increased uncertainty near [1,0,-1,0] crystal axis. Additional indents in this area may improve distributions across the board.

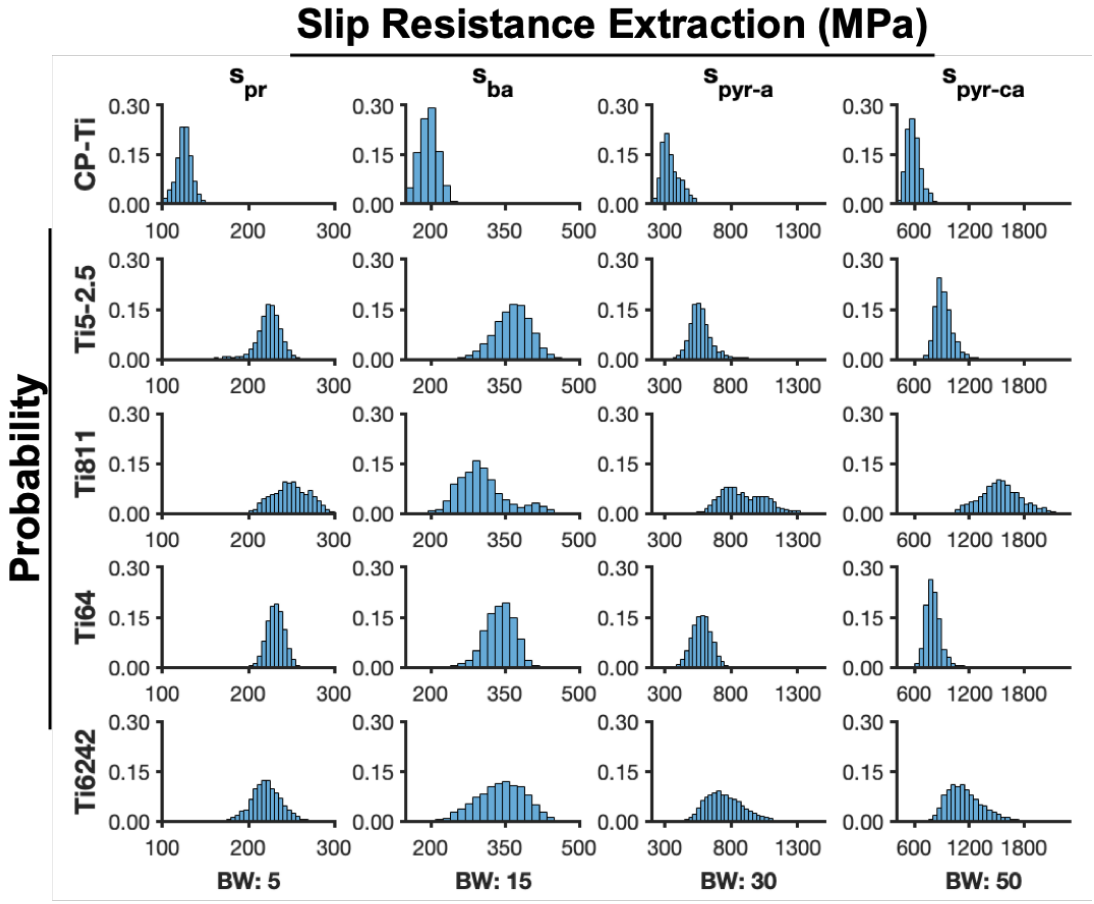

	s_{pr} (MPa)	s_{ba} (MPa)	s_{pyr-a} (MPa)	S_{pyr-ca} (MPa)
CP-Ti	125 ± 9	195 ± 20	346 ± 69	589 ± 77
Ti5-2.5	223 ± 15	366 ± 36	573 ± 96	921 ± 96
Ti811	249 ± 21	304 ± 49	894 ± 165	1546 ± 220
Ti64	231 ± 10	340 ± 30	579 ± 72	804 ± 82
Ti6242	221 ± 18	342 ± 49	748 ± 135	1150 ± 189

Figure 6.6. Top: Distributions of initial slip resistances for alloys considered in this work. BW denotes the fixed bin width for the distributions in a given column. Bottom: The mean and corresponding standard deviation of the extracted initial slip resistances are shown.

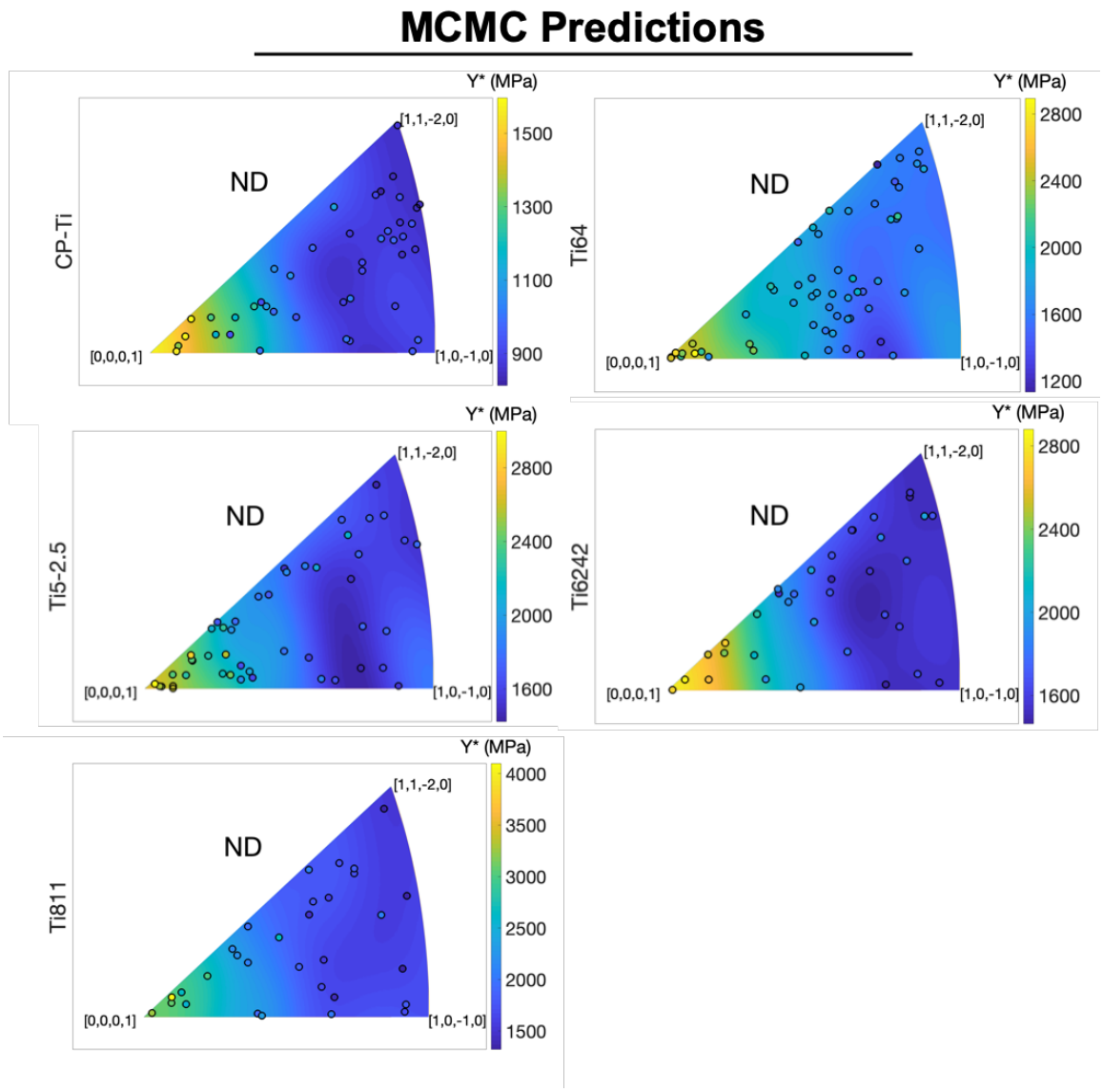

Figure 6.7. IPF Contours for Indentation Yield predictions using reduced order model and sample MCMC chains. The experimental measurements used in the extraction process are shown distinguished circles and are colored in accordance to their actual value.

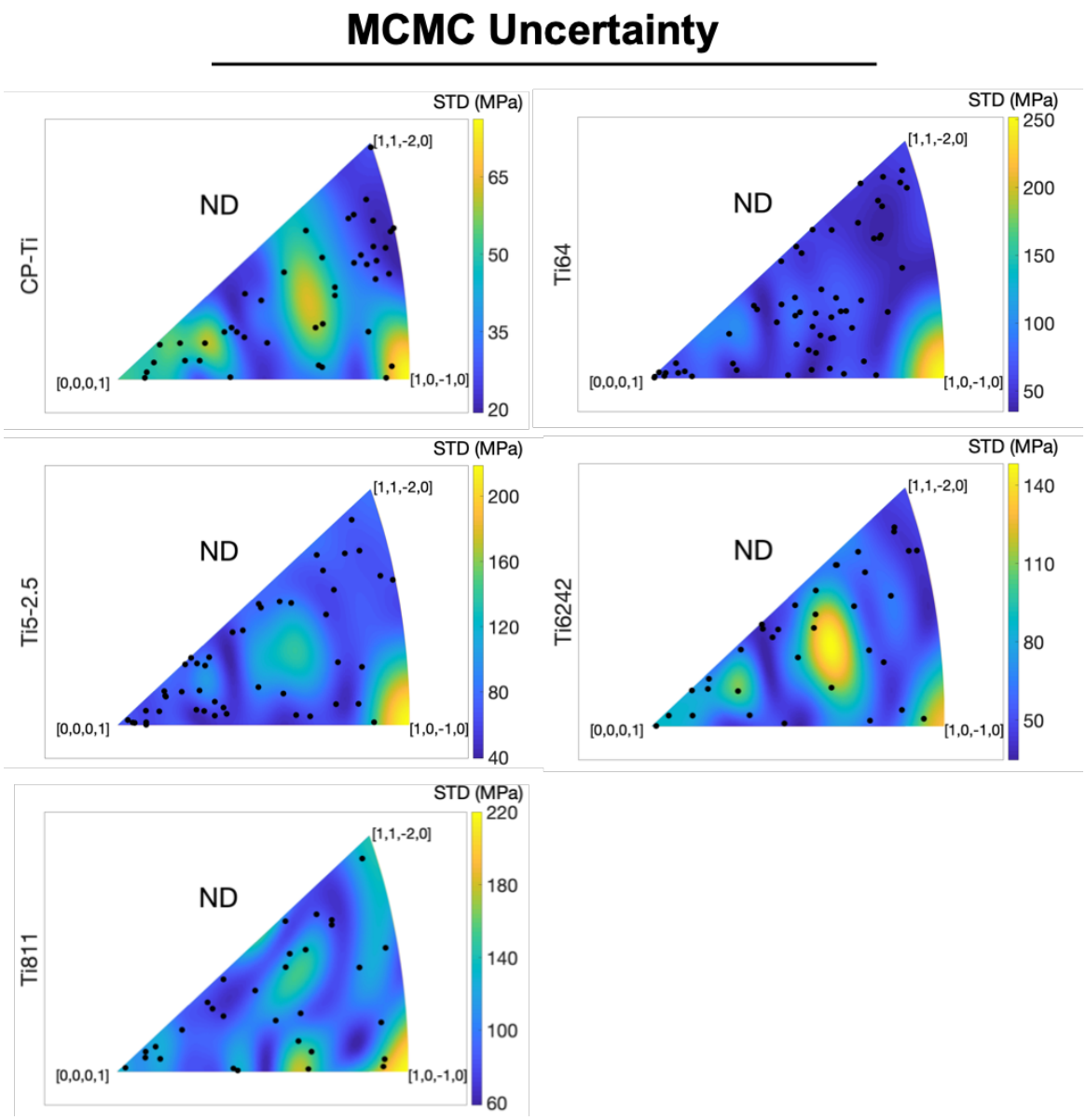

Figure 6.8. IPF contours of Standard deviation of predictions from reduced order model for Indentation Yield using sampled MCMC chains. Orientations of the available experimental measurements used in the sampling process are displayed by the black dots.

6.6 Conclusion

Protocols for the Bayesian estimation of single crystal level elastic-plastic properties from available experimental spherical indentation stress-strain measurements have been presented. The 2 Step Bayesian Framework presented here enables the quantification and

propagation of uncertainty in the observed experimental spherical indentation stress strain measurements to the extracted crystal level properties. Although the associated physics based finite element simulations are computationally expensive, the generation of a suitable database presents a one-time cost in establishing a reduced-order model (Step (1) of the proposed two-step protocol). Once the reduced-order model is established, the calibration of the underlying intrinsic properties to available experimental data (Step (2) of the proposed two-step protocol) can be accomplished with relatively minimal computational resources. The present work highlights the strengths in dividing up the tasks involved in crystal level properties estimation via spherical indentation into reduced order model building and calibration steps. This is evidenced by the adoption of a reduced order model built in a previous work and usage here to extract single crystal elastic constants. Furthermore, the protocols presented here successfully demonstrate the generation of a consistent dataset of initial slip resistances, with quantified uncertainty, corresponding to multiple titanium alloys with differing chemical compositions. Due to the formulation of normalized indentation yield, the extraction efforts are made much more robust, and additional alloys can be readily considered using the protocols established here. The generation of such a comprehensive dataset of single crystal properties at the crystal level using spherical indentation measurements is the first of its kind to the authors knowledge.

REFERENCES

1. Weaver JS, Priddy MW, McDowell DL, Kalidindi SR (2016) On capturing the grain-scale elastic and plastic anisotropy of alpha-Ti with spherical nanoindentation and electron back-scattered diffraction. Acta Materialia 117:23-34. doi:https://doi.org/10.1016/j.actamat.2016.06.053
2. Uchic MD, Dimiduk DM, Florando JN, Nix WD (2004) Sample Dimensions Influence Strength and Crystal Plasticity. Science 305 (5686):986-989. doi:10.1126/science.1098993
3. Bates BC, Campbell EP (2001) A Markov Chain Monte Carlo Scheme for parameter estimation and inference in conceptual rainfall-runoff modeling. Water Resources Research 37 (4):937-947. doi:10.1029/2000WR900363
4. Khosravani A, Morsdorf L, Tasan CC, Kalidindi SR (2018) Multiresolution mechanical characterization of hierarchical materials: Spherical nanoindentation on martensitic Fe-Ni-C steels. Acta Materialia 153:257-269. doi:https://doi.org/10.1016/j.actamat.2018.04.063
5. Vlassak JJ, Nix WD (1994) Measuring the elastic properties of anisotropic materials by means of indentation experiments. Journal of the Mechanics and Physics of Solids 42 (8):1223-1245. doi:https://doi.org/10.1016/0022-5096(94)90033-7
6. Priddy MW (2016) Exploration of forward and inverse protocols for property optimization of Ti-6Al-4V. Georgia Institute of Technology,
7. Patel DK, Al-Harbi HF, Kalidindi SR (2014) Extracting single-crystal elastic constants from polycrystalline samples using spherical nanoindentation and orientation measurements. Acta Materialia 79:108-116. doi:10.1016/j.actamat.2014.07.021
8. Zambaldi C, Yang Y, Bieler TR, Raabe D (2012) Orientation informed nanoindentation of α-titanium: Indentation pileup in hexagonal metals deforming by prismatic slip. Journal of Materials Research 27 (1):356-367. doi:10.1557/jmr.2011.334
9. Bhattacharya AK, Nix WD (1988) Finite element simulation of indentation experiments. International Journal of Solids and Structures 24 (9):881-891. doi:10.1016/0020-7683(88)90039-X
10. Patel D, Kalidindi S (2017) Estimating the slip resistance from spherical nanoindentation and orientation measurements in polycrystalline samples of cubic metals. International Journal of Plasticity 92:19
11. Donohue BR, Ambrus A, Kalidindi SR (2012) Critical evaluation of the indentation data analyses methods for the extraction of isotropic uniaxial mechanical properties using finite element models. Acta Materialia 60 (9):3943-3952. doi:10.1016/j.actamat.2012.03.034
12. Zambaldi C, Raabe D (2010) Plastic anisotropy of gamma-TiAl revealed by axisymmetric indentation. Acta Materialia 58 (9):3516-3530. doi:10.1016/j.actamat.2010.02.025
13. Pathak S, Stojakovic D, Kalidindi SR (2009) Measurement of the local mechanical properties in polycrystalline samples using spherical nanoindentation and orientation

imaging microscopy. Acta Materialia 57 (10):3020-3028. doi:https://doi.org/10.1016/j.actamat.2009.03.008
14. Pathak S, Kalidindi SR (2015) Spherical nanoindentation stress–strain curves. Materials Science and Engineering: R: Reports 91:1-36
15. Weaver JS, Kalidindi SR (2016) Mechanical characterization of Ti-6Al-4V titanium alloy at multiple length scales using spherical indentation stress-strain measurements. Materials & Design 111:463-472. doi:https://doi.org/10.1016/j.matdes.2016.09.016
16. Patel DK, Kalidindi SR (2016) Correlation of spherical nanoindentation stress-strain curves to simple compression stress-strain curves for elastic-plastic isotropic materials using finite element models. Acta Materialia 112:295-302. doi:https://doi.org/10.1016/j.actamat.2016.04.034
17. Hertz H (1896) Miscellaneous Papers (trans: Daniel Evan Jones GAS). MacMillan and Co., Ltd., New York
18. Kalidindi SR, Pathak S (2008) Determination of the effective zero-point and the extraction of spherical nanoindentation stress-strain curves. Acta Materialia 56 (14):3523-3532. doi:10.1016/j.actamat.2008.03.036
19. Kalidindi SR, Bronkhorst CA, Anand L (1992) Crystallographic texture evolution in bulk deformation processing of FCC metals. Journal of the Mechanics and Physics of Solids 40 (3):537-569
20. Kalidindi SR (1998) Incorporation of deformation twinning in crystal plasticity models. Journal of the Mechanics and Physics of Solids 46 (2):267-290
21. Needleman A, Asaro RJ, Lemonds J, Peirce D (1985) Finite element analysis of crystalline solids. Computer Methods in Applied Mechanics and Engineering 52 (1):689-708. doi:https://doi.org/10.1016/0045-7825(85)90014-3
22. Bunge H-J (1993) Texture analysis in materials science. Mathematical Methods (trans: Morris PR). Cuvillier Verlag, Göttingen
23. Adams BL, Kalidindi SR, Fullwood DT (2012) Microstructure sensitive design for performance optimization. Oxford, Elsevier Science
24. Proust G, Kalidindi SR (2006) Procedures for construction of anisotropic elastic-plastic property closures for face-centered cubic polycrystals using first-order bounding relations. Journal of the Mechanics and Physics of Solids 54 (8):1744-1762. doi:10.1016/j.jmps.2006.01.010
25. Knezevic M, Kalidindi SR, Mishra RK (2008) Delineation of first-order closures for plastic properties requiring explicit consideration of strain hardening and crystallographic texture evolution. International Journal of Plasticity 24 (2):327-342. doi:10.1016/j.ijplas.2007.05.002
26. Yabansu YC, Patel DK, Kalidindi SR (2014) Calibrated localization relationships for elastic response of polycrystalline aggregates. Acta Materialia 81:151-160
27. Yabansu YC, Kalidindi SR (2015) Representation and calibration of elastic localization kernels for a broad class of cubic polycrystals. Acta Materialia 94:26-35
28. Box GEP (1973) Bayesian inference in statistical analysis. Reading, Mass., Addison-Wesley Pub. Co., Reading, Mass.
29. Gelman A, Carlin J, Stern H, Dunson D, Vehtari A, Rubin D (2014) Bayesian Data Analysis, Third Edition (Chapman & {Hall/CRC} Texts in Statistical Science). Chapman and Hall/CRC. doi:citeulike-article-id:12855856

30. MacKay DJC (1992) Bayesian Interpolation. Neural Computation 4 (3):415-447. doi:10.1162/neco.1992.4.3.415
31. Christopher MB (2006) PATTERN RECOGNITION AND MACHINE LEARNING. Springer-Verlag New York,
32. J.C. MacKay D (1996) Hyperparameters: Optimize, or Integrate Out? doi:10.1007/978-94-015-8729-7_2
33. MacKay DJC (1998) Introduction to Gaussian process. Neural Networks and Machine Learning
34. Gelman A (2004) Bayesian data analysis. 2nd edition.. edn. Boca Raton, Fla. : Chapman & Hall/CRC, Boca Raton, Fla.
35. Haario H, Saksman E, Tamminen J (2005) Componentwise adaptation for high dimensional MCMC. Computational Statistics 20 (2):265-273. doi:10.1007/BF02789703
36. Chib S, Greenberg E (1995) Understanding the Metropolis-Hastings Algorithm. The American Statistician 49 (4):327-335. doi:10.1080/00031305.1995.10476177
37. Roberts GO, Gelman A, Gilks WR (1997) Weak Convergence and Optimal Scaling of Random Walk Metropolis Algorithms. The Annals of Applied Probability 7 (1):110-120. doi:10.1214/aoap/1034625254
38. Kullback S, Leibler RA (1951) On Information and Sufficiency. Ann Math Statist 22 (1):79-86. doi:10.1214/aoms/1177729694
39. Shannon CE, Weaver W, Wiener N (1950) The Mathematical Theory of Communication. Physics Today 3 (9):31-32. doi:10.1063/1.3067010
40. Ryan EG, Drovandi CC, McGree JM, Pettitt AN (2016) A Review of Modern Computational Algorithms for Bayesian Optimal Design. International Statistical Review 84 (1):128-154. doi:10.1111/insr.12107
41. Lindley DV (1956) On a Measure of the Information Provided by an Experiment. Ann Math Statist 27 (4):986-1005. doi:10.1214/aoms/1177728069
42. Huan X, Marzouk YM (2013) Simulation-based optimal Bayesian experimental design for nonlinear systems. Journal of Computational Physics 232 (1):288-317. doi:https://doi.org/10.1016/j.jcp.2012.08.013
43. Rasmussen CE Evaluation of Gaussian processes and other methods for non-linear regression. University of Toronto,
44. Castillo AR, Kalidindi SR (2019) A Bayesian Framework for the Estimation of the Single Crystal Elastic Parameters from Spherical Indentation Stress-Strain Measurements. Frontiers in Materials 6:136
45. Gelman A (2004) Bayesian data analysis. In., 2nd edition.. edn. Chapman & Hall/CRC, Boca Raton, Fla., p 276
46. MacKay DJC (1992) Information-Based Objective Functions for Active Data Selection. Neural Computation 4 (4):590-604. doi:10.1162/neco.1992.4.4.590
47. Castillo AR, Joseph VR, Kalidindi SR (2019) Bayesian Sequential Design of Experiments for Extraction of Single-Crystal Material Properties from Spherical Indentation Measurements on Polycrystalline Samples. JOM:1-9
48. Castillo AR, Kalidindi SR (2020) Bayesian estimation of single ply anisotropic elastic constants from spherical indentations on multi-laminate polymer-matrix fiber-reinforced composite samples. Meccanica. doi:10.1007/s11012-020-01154-w

49. Clay SB, Knoth PM (2016) Experimental results of quasi-static testing for calibration and validation of composite progressive damage analysis methods. Journal of Composite Materials 51 (10):1333-1353. doi:10.1177/0021998316658539
50. Sánchez-Martín R, Pérez-Prado MT, Segurado J, Bohlen J, Gutiérrez-Urrutia I, Llorca J, Molina-Aldareguia JM (2014) Measuring the critical resolved shear stresses in Mg alloys by instrumented nanoindentation. Acta Materialia 71:283-292. doi:https://doi.org/10.1016/j.actamat.2014.03.014
51. Adams B, Wright S, Kunze K (1993) Orientation Imaging: The Emergence of a New Microscopy. Metallurgical Transactions A 24:819-831. doi:10.1007/BF02656503
52. Atkinson AC (2007) Optimum experimental designs, with SAS. Oxford : Oxford University Press, Oxford
53. Ferraioli L, Porter E, Plagnol E (2012) Bayesian Inference for LISA Pathfinder using Markov Chain Monte Carlo Methods.
54. MATLAB (2016) version 9.1.0 (R2016b). The MathWorks Inc
55. Simmons G (1971) Single crystal elastic constants and calculated aggregate properties: a handbook. 2d ed.. edn. Cambridge, Mass., M.I.T. Press, Cambridge, Mass.
56. ABAQUS (2014) 6.14 Dassault Systémes Simulia Corp. Providence, RI
57. McKay MD, Beckman RJ, Conover WJ (2000) A Comparison of Three Methods for Selecting Values of Input Variables in the Analysis of Output From a Computer Code. Technometrics 42 (1):55-61. doi:10.1080/00401706.2000.10485979
58. Ranganathan SI, Ostoja-Starzewski M (2008) Universal elastic anisotropy index. Physical review letters 101 (5):055504. doi:10.1103/PhysRevLett.101.055504
59. Maarten De J, Wei C, Thomas A, Anubhav J, Randy N, Anthony G, Marcel S, Chaitanya Krishna A, Sybrand Van Der Z, Jose JP, Cormac T, Stefano C, Gerbrand C, Kristin AP, Mark A (2015) Charting the complete elastic properties of inorganic crystalline compounds. Scientific Data 2. doi:10.1038/sdata.2015.9
60. Hill R (1952) The elastic behaviour of a crystalline aggregate. Proceedings of the Physical Society Section A 65 (5):349-354. doi:10.1088/0370-1298/65/5/307
61. Fisher ES, Renken CJ (1964) Single-Crystal Elastic Moduli and the hcp → bcc Transformation in Ti, Zr, and Hf. Physical Review 135 (2A):A482-A494. doi:10.1103/PhysRev.135.A482
62. Oliver WC, Pharr GM (2004) Measurement of hardness and elastic modulus by instrumented indentation: Advances in understanding and refinements to methodology. Journal of Materials Research 19 (1):3-20. doi:10.1557/jmr.2004.19.1.3
63. Schuh CA (2006) Nanoindentation studies of materials. Materials Today 9 (5):32-40. doi:https://doi.org/10.1016/S1369-7021(06)71495-X
64. Minor AM, Syed Asif SA, Shan Z, Stach EA, Cyrankowski E, Wyrobek TJ, Warren OL (2006) A new view of the onset of plasticity during the nanoindentation of aluminium. Nature Materials 5:697. doi:10.1038/nmat1714 https://www.nature.com/articles/nmat1714#supplementary-information
65. Vachhani SJ, Doherty RD, Kalidindi SR (2016) Studies of grain boundary regions in deformed polycrystalline aluminum using spherical nanoindentation. International Journal of Plasticity 81:87-101. doi:https://doi.org/10.1016/j.ijplas.2016.01.001
66. Zhou AG, Barsoum MW, Basu S, Kalidindi SR, El-Raghy T (2006) Incipient and regular kink bands in fully dense and 10vol.% porous Ti2AlC. Acta Materialia 54 (6):1631-1639. doi:https://doi.org/10.1016/j.actamat.2005.11.035

67. Priddy MW, Paulson NH, Kalidindi SR, McDowell DL (2017) Strategies for rapid parametric assessment of microstructure-sensitive fatigue for HCP polycrystals. International Journal of Fatigue 104:231-242. doi:https://doi.org/10.1016/j.ijfatigue.2017.07.015
68. Fernandez-Zelaia P, Roshan Joseph V, Kalidindi SR, Melkote SN (2018) Estimating mechanical properties from spherical indentation using Bayesian approaches. Materials & Design 147:92-105. doi:https://doi.org/10.1016/j.matdes.2018.03.037
69. Ford I, Titterington DM, Kitsos CP (1989) Recent Advances in Nonlinear Experimental Design. Technometrics 31 (1):49-60. doi:10.2307/1270364
70. Lewis A, Smith R, Williams B, Figueroa V (2016) An information theoretic approach to use high-fidelity codes to calibrate low-fidelity codes. Journal of Computational Physics. doi:10.1016/J.JCP.2016.08.001
71. Aggarwal R, Demkowicz M, Marzouk Y (2014) Bayesian inference of substrate properties from film behavior. Modelling and Simulation in Materials Science and Engineering 23 (1):015009
72. Yoo YS, Jo CY, Jones CN (2002) Compositional prediction of creep rupture life of single crystal Ni base superalloy by Bayesian neural network. Journal of Materials Science and Engineering A 336 (1):22-29. doi:https://doi.org/10.1016/S0921-5093(01)01965-7
73. Bunge HJ (1979) Texture analysis in materials science : mathematical methods. In. Buttersworth & Co., p 376
74. Barlat F, Maeda Y, Chung K, Yanagawa M, Brem JC, Hayashida Y, Lege DJ, Matsui K, Murtha SJ, Hattori S, Becker RC, Makosey S (1997) Yield function development for aluminum alloy sheets. Journal of the Mechanics and Physics of Solids 45 (11):1727-1763. doi:https://doi.org/10.1016/S0022-5096(97)00034-3
75. Caflisch RE (1998) Monte Carlo and quasi-Monte Carlo methods. Acta Numerica 7:1-49. doi:10.1017/S0962492900002804
76. Chapra SC, Canale RP (2010) Numerical methods for engineers. In., 6 edn. Boston: McGraw-Hill Higher Education, p 583
77. Sobol′ IM (2001) Global sensitivity indices for nonlinear mathematical models and their Monte Carlo estimates. Mathematics and Computers in Simulation 55 (1):271-280. doi:https://doi.org/10.1016/S0378-4754(00)00270-6
78. Drovandi CC, McGree JM, Pettitt AN (2014) A Sequential Monte Carlo Algorithm to Incorporate Model Uncertainty in Bayesian Sequential Design. Journal of Computational and Graphical Statistics 23 (1):3-24. doi:10.1080/10618600.2012.730083
79. Yabansu YC, Steinmetz P, Hötzer J, Kalidindi SR, Nestler B (2017) Extraction of reduced-order process-structure linkages from phase-field simulations. Acta Materialia 124:182-194. doi:https://doi.org/10.1016/j.actamat.2016.10.071
80. Panchal JH, Kalidindi SR, McDowell DL (2013) Key computational modeling issues in Integrated Computational Materials Engineering. Computer-Aided Design 45 (1):4-25. doi:https://doi.org/10.1016/j.cad.2012.06.006
81. McDowell DL (2018) Microstructure-Sensitive Computational Structure-Property Relations in Materials Design. In: Shin D, Saal J (eds) Computational Materials System Design. Springer International Publishing, pp 1-25. doi:10.1007/978-3-319-68280-8_1

82. Koronis G, Silva A, Fontul M (2013) Green composites: A review of adequate materials for automotive applications. Composites Part B 44 (1):120-127. doi:10.1016/j.compositesb.2012.07.004
83. Soutis C (2005) Fibre reinforced composites in aircraft construction. Progress in Aerospace Sciences 41 (2):143-151. doi:10.1016/j.paerosci.2005.02.004
84. Hollaway LC (2010) A review of the present and future utilisation of FRP composites in the civil infrastructure with reference to their important in-service properties. Construction and Building Materials 24 (12):2419-2445. doi:10.1016/j.conbuildmat.2010.04.062
85. A.P. Mouritza MKB, P.J. Falzonb, K.H. Leongb (1999) Review of applications for advanced three-dimensional fibre textile composites. Composites Part A: Applied Science and Manufacturing (30):1445-1461
86. Reddy JN, Miravete A (2018) Practical analysis of composite laminates. CRC press,
87. Chamis CC (1989) Mechanics of Composite-Materials - Past, Present, and Future. J Compos Tech Res 11 (1):3-14
88. Kalidindi SR, Franco E (1997) Numerical evaluation of isostrain and weighted-average models for elastic moduli of three-dimensional composites. Composites Science and Technology 57 (3):293-305
89. Pastore C, Gowayed Y (2008) 6 - Structure and mechanics of 2D and 3D textile composites. In: Schwartz P (ed) Structure and Mechanics of Textile Fibre Assemblies. Woodhead Publishing, pp 141-189. doi:https://doi.org/10.1533/9781845695231.141
90. Kregers AF, Melbardis YG (1978) Determination of the deformability of three-dimensionally reinforced composites by the stiffness averaging method. Polymer Mechanics 14 (1):1-5. doi:10.1007/BF00859550
91. Ishikawa T, Chou TW (1982) Stiffness and strength behaviour of woven fabric composites. Journal of Materials Science 17 (11):3211-3220. doi:10.1007/BF01203485
92. Reddy JN (2003) Mechanics of laminated composite plates and shells: theory and analysis. CRC press,
93. Barbero E, Reddy J (1990) Nonlinear analysis of composite laminates using a generalized laminated plate theory. AIAA journal 28 (11):1987-1994
94. Flaggs DK, M (1982) Experimental Determination of the In Situ Transverse Lamina Strength in Graphite/Epoxy Laminates. Journal of Composite Materials 16:103-116
95. Huang ZM (2001) Simulation of the mechanical properties of fibrous composites by the bridging micromechanics model. Compos Part a-Appl S 32 (2):143-172. doi:Doi 10.1016/S1359-835x(00)00142-1
96. Kalidindi SR, Abusafieh A (1996) Longitudinal and transverse moduli and strengths of low angle 3-D braided composites. Journal of Composite Materials 30 (8):885-905
97. Engelstad S, Reddy J (1993) Probabilistic nonlinear finite element analysis of composite structures. AIAA journal 31 (2):362-369
98. Hardiman M, Vaughan TJ, McCarthy CT (2017) A review of key developments and pertinent issues in nanoindentation testing of fibre reinforced plastic microstructures. Composite Structures 180:782-798. doi:10.1016/j.compstruct.2017.08.004
99. Hodzic A, Kalyanasundaram S, Kim JK, Lowe AE, Stachurski ZH (2001) Application of nano-indentation, nano-scratch and single fibre tests in investigation of interphases in composite materials. Micron 32 (8):765-775. doi:Doi 10.1016/S0968-4328(00)00084-6

100. Unnikrishnan GU, Unnikrishnan VU, Reddy JN (2006) Constitutive Material Modeling of Cell: A Micromechanics Approach. Journal of Biomechanical Engineering 129 (3):315-323. doi:10.1115/1.2720908
101. Pathak S, Kalidindi SR, Mara NA (2016) Investigations of orientation and length scale effects on micromechanical responses in polycrystalline zirconium using spherical nanoindentation. Scripta Materialia 113:241-245. doi:http://dx.doi.org/10.1016/j.scriptamat.2015.10.035
102. Rossi A, Castillo A, Przybyla C, Kalidindi SR (2019 (accepted)) Study of Local Mechanical Responses in an Epoxy-Carbon Fiber Laminate Composite Using Spherical Indentation Stress-Strain. Integrating Materials and Manufacturing Innovation
103. Kaddour AS, Hinton MJ (2012) Input data for test cases used in benchmarking triaxial failure theories of composites. Journal of Composite Materials 46 (19-20):2295-2312. doi:10.1177/0021998312449886
104. Joseph VR, Gul E, Ba S (2015) Maximum projection designs for computer experiments. Biometrika 102 (2):371-380
105. Staab GH (1999) 6 - LAMINATE ANALYSIS. In: Staab GH (ed) Laminar Composites. Butterworth-Heinemann, Woburn, pp 191-282. doi:https://doi.org/10.1016/B978-075067124-8/50006-0
106. Khdeir AA, Reddy JN (1989) Exact solutions for the transient response of symmetric cross-ply laminates using a higher-order plate theory. Composites Science and Technology 34 (3):205-224. doi:https://doi.org/10.1016/0266-3538(89)90029-8
107. ASTM D (2008) Standard test method for tensile properties of polymer matrix composite materials.
108. Donachie MJ (2000) Titanium: a technical guide. ASM international,
109. Lütjering G, Williams JC (2007) Titanium. Springer Science & Business Media,
110. Sankaran KK, Mishra RS (2017) Metallurgy and design of alloys with hierarchical microstructures. Elsevier,
111. Zhang M, Zhang J, McDowell D (2007) Microstructure-based crystal plasticity modeling of cyclic deformation of Ti–6Al–4V. International Journal of Plasticity 23 (8):1328-1348
112. Fundenberger J, Philippe M, Wagner F, Esling C (1997) Modelling and prediction of mechanical properties for materials with hexagonal symmetry (zinc, titanium and zirconium alloys). Acta materialia 45 (10):4041-4055
113. Philippe M, Wagner F, Mellab F, Esling C, Wegria J (1994) Modelling of texture evolution for materials of hexagonal symmetry—I. Application to zinc alloys. Acta metallurgica et materialia 42 (1):239-250
114. Wu XP, Kalidindi SR, Necker C, Salem AA (2008) Modeling Anisotropic Stress-Strain Response and Crystallographic Texture Evolution in alpha-Titanium during Large Plastic Deformation using Taylor-Type Models: Influence of Initial Texture and Purity. Metallurgical and Materials Transactions a-Physical Metallurgy and Materials Science 39A (12):3046-3054. doi:10.1007/s11661-008-9651-x
115. Wu X, Kalidindi SR, Necker C, Salem AA (2007) Prediction of crystallographic texture evolution and anisotropic stress-strain curves during large plastic strains in high purity [alpha]-titanium using a Taylor-type crystal plasticity model. Acta Materialia 55 (2):423-432

116. Segurado J, Lebensohn RA, LLorca J, Tomé CN (2012) Multiscale modeling of plasticity based on embedding the viscoplastic self-consistent formulation in implicit finite elements. International Journal of Plasticity 28 (1):124-140
117. Williams J, Baggerly R, Paton N (2002) Deformation behavior of HCP Ti-Al alloy single crystals. Metallurgical and Materials Transactions A 33 (3):837-850
118. Jun T-S, Zhang Z, Sernicola G, Dunne FP, Britton TB (2016) Local strain rate sensitivity of single α phase within a dual-phase Ti alloy. Acta Materialia 107:298-309
119. Dimiduk D, Uchic M, Parthasarathy T (2005) Size-affected single-slip behavior of pure nickel microcrystals. Acta Materialia 53 (15):4065-4077
120. Kiener D, Grosinger W, Dehm G, Pippan R (2008) A further step towards an understanding of size-dependent crystal plasticity: In situ tension experiments of miniaturized single-crystal copper samples. Acta Materialia 56 (3):580-592
121. Gong J, Wilkinson AJ (2009) Anisotropy in the plastic flow properties of single-crystal α titanium determined from micro-cantilever beams. Acta Materialia 57 (19):5693-5705
122. Tomé C, Maudlin P, Lebensohn R, Kaschner G (2001) Mechanical response of zirconium—I. Derivation of a polycrystal constitutive law and finite element analysis. Acta Materialia 49 (15):3085-3096
123. Philippe M, Serghat M, Van Houtte P, Esling C (1995) Modelling of texture evolution for materials of hexagonal symmetry—II. application to zirconium and titanium α or near α alloys. Acta metallurgica et materialia 43 (4):1619-1630
124. Britton T, Liang H, Dunne F, Wilkinson A (2010) The effect of crystal orientation on the indentation response of commercially pure titanium: experiments and simulations. Proceedings of the Royal Society A: Mathematical, Physical and Engineering Sciences 466 (2115):695-719
125. Huang X, Pelegri AA (2005) Mechanical Characterization of Thin Film Materials with Nanoindentation Measurements and FE Analysis. Journal of Composite Materials 40 (15):1393-1407. doi:10.1177/0021998305059728
126. Lucchini R, Carnelli D, Ponzoni M, Bertarelli E, Gastaldi D, Vena P (2011) Role of damage mechanics in nanoindentation of lamellar bone at multiple sizes: Experiments and numerical modeling. Journal of the Mechanical Behavior of Biomedical Materials 4 (8):1852-1863. doi:https://doi.org/10.1016/j.jmbbm.2011.06.002
127. Higdon D, Kennedy M, Cavendish JC, Cafeo JA, Ryne RD (2004) Combining field data and computer simulations for calibration and prediction. SIAM Journal on Scientific Computing 26 (2):448-466
128. Santner TJ, Williams BJ, Notz W, Williams BJ (2003) The design and analysis of computer experiments, vol 1. Springer,
129. Kalidindi SR (2015) Hierarchical materials informatics: novel analytics for materials data. Elsevier,